ตัวเร่งปฏิกิริยาออกไซด์ผสมสตรอนเทียมและไทเทเนียมแบบโครงสร้างมีโซสำหรับการสังเคราะห์เมทิลเอสเทอร์ของกรดไขมัน

นายบุญทวี เลิศปัญญาพรชัย

วิทยานิพนธ์นี้เป็นส่วนหนึ่งของการศึกษาตามหลักสูตรปริญญาวิทยาศาสตรดุษฎีบัณฑิต
สาขาวิชาปิโตรเคมี
คณะวิทยาศาสตร์ จุฬาลงกรณ์มหาวิทยาลัย
ปีการศึกษา 2558

MESOSTRUCTURED Sr AND Ti MIXED OXIDE CATALYSTS FOR SYNTHESIS OF FATTY ACID METHYL ESTERS

Mr. Boontawee Lertpanyapornchai

A Dissertation Submitted in Partial Fulfillment of the Requirements
for the Degree of Doctor of Philosophy Program in Petrochemistry
Faculty of Science
Chulalongkorn University
Academic Year 2015

Thesis Title	MESOSTRUCTURED Sr AND Ti MIXED OXIDE CATALYSTS FOR SYNTHESIS OF FATTY ACID METHYL ESTERS
By	Mr. Boontawee Lertpanyapornchai
Field of Study	Petrochemistry
Thesis Advisor	Associate Professor Chawalit Ngamcharussrivichai, Ph.D.
Thesis Co-Advisor	Assistant Professor Toshiyuki Yokoi, Ph.D.

Accepted by the Faculty of Science, Chulalongkorn University in Partial Fulfillment of the Requirements for the Doctoral Degree

....Dean of the Faculty of Science

(Associate Professor Polkit Sangvanich, Ph.D.)

THESIS COMMITTEE

....Chairman

(Professor Pattarapan Prasassarakich, Ph.D.)

....Thesis Advisor

(Associate Professor Chawalit Ngamcharussrivichai, Ph.D.)

....Thesis Co-Advisor

(Assistant Professor Toshiyuki Yokoi, Ph.D.)

....Examiner

(Associate Professor Wimonrat Trakarnpruk, Ph.D.)

....Examiner

(Assistant Professor Warinthorn Chavasiri, Ph.D.)

....External Examiner

(Associate Professor Tawan Sooknoi, Ph.D.)

บุญทวี เลิศปัญญาพรชัย : ตัวเร่งปฏิกิริยาออกไซด์ผสมสตรอนเทียมและไทเทเนียมแบบโครงสร้างมีโซสำหรับการสังเคราะห์เมทิลเอสเทอร์ของกรดไขมัน (MESOSTRUCTURED Sr AND Ti MIXED OXIDE CATALYSTS FOR SYNTHESIS OF FATTY ACID METHYL ESTERS) อ.ที่ปรึกษาวิทยานิพนธ์หลัก: รศ. ดร. ชวลิต งามจรัสศรีวิชัย, อ.ที่ปรึกษาวิทยานิพนธ์ร่วม: ผศ. ดร. โทชิยูกิ โยโคอิ, 140 หน้า.

งานวิจัยนี้มีจุดประสงค์เพื่อสังเคราะห์ออกไซด์ผสมสตรอนเทียมและไทเทเนียมโครงสร้างแบบมีโซ (MSTs) ผ่านวิธีการจัดเรียงตนเองโซลเจลเผาไหม้ โดยใช้พลูโรนิก พี 123 เป็นสารกำหนดโครงสร้าง และประยุกต์เป็นตัวเร่งปฏิกิริยาในปฏิกิริยาทรานส์เอสเทอริฟิเคชันของน้ำมันเมล็ดในปาล์ม (PKO) และเมทานอล เริ่มต้นด้วยการศึกษาผลกระทบด้านพารามิเตอร์การสังเคราะห์ ต่อสมบัติทางเคมีกายภาพของ MSTs ผลการทดลองพบว่า MST ที่สังเคราะห์โดยใช้อัตราส่วนโดยโมลระหว่างกรดซิตริกต่อโลหะทั้งหมดที่ 1 ต่อ 1, ปริมาณพลูโรนิก พี 123 ที่ 0.17 มิลลิโมล และอุณหภูมิการเผา 600 องศาเซลเซียส แสดงสมบัติด้านโครงสร้างและพื้นผิวที่ดี ต่อจากนั้น MST ที่สังเคราะห์โดยปราศจากกรดซิตริก (MST-0C-0.17P(600)) และ MST ที่สังเคราะห์โดยเติมกรดซิตริกในอัตราส่วนโดยโมลระหว่างกรดซิตริกต่อโลหะทั้งหมดที่ 1 ต่อ 1 (MST-1C-0.17P(600)) ถูกเปรียบเทียบในแง่ความว่องไวในการเร่งปฏิกิริยาและความเสถียรภาพในปฏิกิริยาทรานส์เอสเทอริฟิเคชัน แม้ว่าปฏิกิริยาทรานส์เอสเทอริฟิเคชันที่ใช้ MST-1C-0.17P(600) เป็นตัวเร่งปฏิกิริยา ใช้อุณหภูมิสูงกว่าการใช้ MST-0C-0.17P(600) เป็นตัวเร่งปฏิกิริยา เพื่อดำเนินปฏิกิริยาให้ได้ผลผลิตของเมทิลเอสเทอร์ของกรดไขมัน ร้อยละ99.8 โดยน้ำหนัก แต่อย่างไรก็ตาม MST-1C-0.17P(600) แสดงเสถียรภาพเชิงเคมีในปฏิกิริยาทรานส์เอสเทอริฟิเคชันที่ดีกว่า MST-0C-0.17P(600) สุดท้าย ผลการทดลองจากอินซิทู ฟลูเรียร์ทรานส์ฟอร์ม อินฟราเรดสเปคโทรเมทรี (*in situ* FTIR) พบว่าลักษณะของตำแหน่งกัมมันต์บนผิวของ MST-C-0.17P(600) มีตำแหน่งกรดชนิดลิวอิส และตำแหน่งเบส 4 ชนิดที่มีความแรงแตกต่างกัน จากนั้นผลการทดลองจาก *in situ* FTIR ให้ข้อมูลเกี่ยวกับลักษณะของเมทานอลและเอทิลโพพิโอเนตซึ่งเป็นโมเดลของไตรกลีเซอไรด์ที่ถูกดูดซับบนตำแหน่งกัมมันต์ของ MST-C-0.17P(600) นอกจากนี้ผลการทดลองจาก *in situ* FTIR สามารถนำมาใช้เพื่อเสนอกลไกปฏิกิริยาสำหรับทรานส์เอสเทอริฟิเคชันโดยใช้ MST-C-0.17P(600) เป็นตัวเร่งปฏิกิริยา

สาขาวิชา ปิโตรเคมี	ลายมือชื่อนิสิต ....
ปีการศึกษา 2558	ลายมือชื่อ อ.ที่ปรึกษาหลัก ....
	ลายมือชื่อ อ.ที่ปรึกษาร่วม ....

5572822223 : MAJOR PETROCHEMISTRY

KEYWORDS: STRONTIUM TITANATE / MESOPOROUS MIXED OXIDES / TRANSESTERIFICATION / PALM KERNEL OIL / SOL-GEL COMBUSTION

BOONTAWEE LERTPANYAPORNCHAI: MESOSTRUCTURED Sr AND Ti MIXED OXIDE CATALYSTS FOR SYNTHESIS OF FATTY ACID METHYL ESTERS. ADVISOR: ASSOC. PROF. CHAWALIT NGAMCHARUSSRIVICHAI, Ph.D., CO-ADVISOR: ASST. PROF. TOSHIYUKI YOKOI, Ph.D., 140 pp.

The objectives of this research were synthesis of mesostructured Sr and Ti mixed oxides (MSTs) via a self-assembly sol-gel combustion method using Pluronic P123 as a structure-directing agent, in order to use them as heterogeneous catalyst in transesterification of palm kernel oil (PKO) and methanol. Firstly, the effects of synthesis parameters on physicochemical properties of MSTs were studied. The results showed that the MST synthesized with molar ratio of citric acid: total metals at 1: 1, amount of Pluronic P123 at 0.17 mmol and calcination temperature at 600 °C exhibited good structural and textural properties. After that, the catalytic activity and stability of MST synthesized without citric acid (MST-0C-0.17P(600)) and MST synthesized with adding citric acid at molar ratio of citric acid: total metals 1: 1 (MST-1C-0.17P(600)) were comparatively studied in transesterification. Although the reaction over MST-1C-0.17P(600)) required the temperature higher than that over MST-0C-0.17P(600)), to achieve the fatty acid methyl esters (FAME) yield of 99.8 wt%, the MST-1C-0.17P(600)) showed superior chemical stability compared to the MST-0C-0.17P(600)) in the transesterification. Finally, the results from *in situ* FTIR showed that MST-1C-0.17P(600)) had Lewis acid sites and 4 types with different strength of basic sites. Furthermore, *in situ* FTIR results provided the information about the nature of adsorbed methanol and ethyl propionate species on the active sites of MST-1C-0.17P(600). Moreover, the reaction mechanism for the transesterification using the MST-1C-0.17P(600) as catalyst was proposed.

Field of Study:	Petrochemistry	Student's Signature	....
Academic Year:	2015	Advisor's Signature	....
		Co-Advisor's Signature	....

ACKNOWLEDGEMENTS

I would like to take this opportunity to express my immense gratitude to all those persons who have given their invaluable support and assistance.

In particular, I am profoundly indebted to my supervisors, Assoc. Prof. Chawalit Ngamcharussrivichai. He was very generous with his time and knowledge and assisted me in each step to complete my research. I express my gratitude to my co-advisor, Asst. Prof. Toshiyuki Yokoi who offered many helpful suggestions and supported my study during 9 months at Chemical Resources Laboratory, Tokyo Institute of Technology, Japan. I also thank all Nomura laboratory's member (Kubota, Yunan and etc.) for their helpful advices, supports, encouragement and friendships during my period in Japan. Sincerest appreciation also extends to The Royal Golden Jubilee Scholarship (Thailand Research Fund) for financial support of this research.

I would like to acknowledge Prof. Pattarapan Prasassarakich, Assoc. Prof. Wimonrat Trakarnpruk, Asst. Prof. Warinthorn Chavasiri and Assoc. Prof. Tawan Sooknoi for their participation on the dissertation chairman and members of dissertation committee, respectively.

Lastly, I would like to thank my research group members (Niti, Wayu, Polthep, etc.) for suggestion, kindly support about my thesis and encouragement of my family who always beside me throughout Ph.D. period. This thesis is dedicated to them.

CONTENTS

Page

Page

Page

LIST OF TABLES

LIST OF FIGURES

CHAPTER I

Introduction

1.1 Motivation

Fatty acid methyl esters (FAMEs) are the important bio-based intermediates in various industries, such as biofuels, biolubricants, detergents, cosmetics and pharmaceuticals. FAME is conventionally obtained via transesterification of vegetable oils or animal fats with methanol. The transesterification to produce FAME can be catalyzed by either acidic or basic catalysts. Due to its high catalytic activity and less corrosiveness, homogeneous bases are more preferentially when compared to the acid counterparts [1]. However, the use of homogeneous catalysts results in undesirable effects when free fatty acids and/or water is present in feedstock, leading to formation of soap and lowering the FAME yield [2]. Moreover, the transesterification via homogeneous catalysis has several drawbacks, for example, difficulty of catalyst removal, a large amount of wastewater discharged, environmental pollution and contaminated glycerol. An alternative method for the production of FAME is to use heterogeneous base catalysts. The general advantages of using these catalysts are easy separation, less soap formation and reusability [1]. Various types of metal oxides have been investigated as solid base catalysts in the transesterification of triglycerides with methanol to produce FAME [3, 4].

Alkali earth metal oxides, including MgO, CaO, SrO and BaO were extensively applied as heterogeneous catalysts to the transesterification of triglycerides because they exhibited high basicity and gave high FAME yield under mild conditions [5-7]. Direct calcination of alkaline earth metal salt precursors at high temperatures is a common route to prepare the corresponding metal oxides of which the specific surface area is very low due to a sintering effect. To overcome this problem, metal oxides supported on high surface area materials were applied as the catalysts. The supported metal oxides used in the transesterification were commonly prepared by impregnation, followed by calcination at 500–600 °C [8-10]. Although the catalysts attained had better textural properties than the single metal oxides, they exhibited severe leaching effect [8]. To successfully commercialize the heterogeneously catalyzed transesterification process, the catalyst stability is the major issue that requires further research and development. Recently, mixed metal oxides have received much attention because their basicity and stability can be adjusted via modification of elemental composition and synthesis procedure. It was proposed that the catalytic activity of mixed oxides was improved by generation of newly strong basic sites or lattice defects [11], while a strong interaction between metal ions with different valence states in the oxide lattice enhanced the catalyst stability.

Strontium and titanium mixed oxides or strontium titanates ($SrTiO_3$) have been used in a broad field of heterogeneous catalysis because of its high activity [12], chemical stability, structural stability and thermal stability [13]. The conventional method for $SrTiO_3$ synthesis involves a solid-state reaction wherein $SrCO_3$ and TiO_2 powders are mixed and calcined at 1200 °C [14]. This method not only consumes a massive amount of energy but also results in particle-size non-uniformity and compositional inhomogeneity [14]. Several synthesis methods, such as hydrothermal technique [12], sol-gel method [15], combustion method [16], and sol-gel combustion method [17], have been studied in an attempt to improve the physicochemical properties of $SrTiO_3$. The sol-gel combustion method appears promising as a route to prepare a high-purity mixed oxide [17]. Citric acid as a reducing agent and fuel was added to a mixed-metal precursor solution to induce the redox reaction with nitrate anions. Then, the generated exothermic heat facilitated the formation of $SrTiO_3$ nanoparticles at relatively low calcination temperatures [17]. However, the $SrTiO_3$ attained by all of these methods exhibited low specific surface area (<5 m^2 g^{-1}) [12, 15] and porosity [15-17].

In the past few decades, mesoporous materials have attracted considerable attention because of their large surface area and high porosity, which are advantageous in various applications [18, 19]. The synthesis of $SrTiO_3$ with a mesostructure remarkably increases the textural properties. However, the synthesis of mesostructure $SrTiO_3$ via soft template route using commercial neutral-templating molecules is more difficult than that of silica-based mesoporous materials since the transformation of amorphous metal oxide nanoparticles to crystalline mixed oxides during thermal treatment disturbs the mesostructure arrangement [20] due to weak interactions between metal species and templating molecules.

In this dissertation the mesostructure Sr and Ti mixed oxides (MST) were synthesized via neutral-templated self-assembly sol-gel combustion method using Pluronic P123 (PEO_{20}-*b*-PPO_{70}-*b*-PEO_{20}; PEO = poly [ethylene oxide] and PPO = poly[propylene oxide]) as neutral-templating molecules. It is expected that the addition of citric acid as complexing agent and fuel in the combustion step not only enhances purity and crystallinity of $SrTiO_3$ phase but also promotes formation of mesoporosity in the MST obtained. The MST materials were characterized for their physicochemical properties using various techniques. Then, the obtained MSTs were applied as heterogeneous catalysts to the transesterification of vegetable oil with methanol to produce FAME. Moreover, the effects of free fatty acid and water containing in feedstock on the FAME yield and the structural properties of MST were investigated. Finally, the nature of active sites of MST catalysts was studied using *in situ* Fourier-transform infrared spectroscopy.

1.2 Objectives

1.2.1 To prepare mesostructured Sr and Ti mixed oxides (MST) via neutral-templated self-assembly sol-gel combustion method

1.2.2 To study the effects of synthesized parameters on physicochemical properties of MST

1.2.3 To study catalytic performance of MST in the transesterification of vegetable oil with methanol

1.2.4 To study nature of active sites on MST for the transesterification

1.3 Scope of this dissertation

This dissertation was separated into 3 parts. The scope of each part is schematically described in Figure 1.1.

1.3.1 Part A: Mesostructued Sr and Ti mixed oxides (MSTs) were synthesized via neutral-templated self-assembly sol-gel combustion method using triblock copolymer Pluronic P123 as neutral-templating agent. Effects of citric acid addition, molar ratio of citric acid: total metals, amount of structural-directing agent and calcination temperature on the physicochemical properties of the MST obtained were investigated. Characterization of MST materials was performed using thermal gravimetric/ differential thermal analysis (TG/DTA), powder X-ray diffraction (XRD), scanning transmission electron microscopy (STEM), transmission electron microscopy (TEM) and N_2 adsorption-desorption measurement.

1.3.2 Part B: Catalytic performance of MST was studied in transesterification of vegetable oil with methanol. The reaction was performed in an autoclave reactor. The acidic and basic properties of MST catalysts were determined by Hammett indicator and acid-base titration method. Effect of reaction parameters, including molar ratio of methanol: oil, catalyst loading, reaction temperature, and reaction time, on the FAME yield was studied. Then, effect of free fatty acid (FFA), as oleic acid, and water on the FAME yield was investigated. Finally, the kinetics and thermodynamics of transesterification over MST catalyst were also studied.

1.3.3 Part C: To obtain information about nature of active sites, the acidic and basic properties of MST were investigated by *in situ* Fourier-transform infrared spectroscopy (*in situ* FTIR) using pyridine and pyrrole as molecular probes, respectively. Nature of active site of methanol and ethyl propionate as model reactant molecules on the MST surface was also elucidated by *in situ* Fourier-transform infrared spectroscopy.

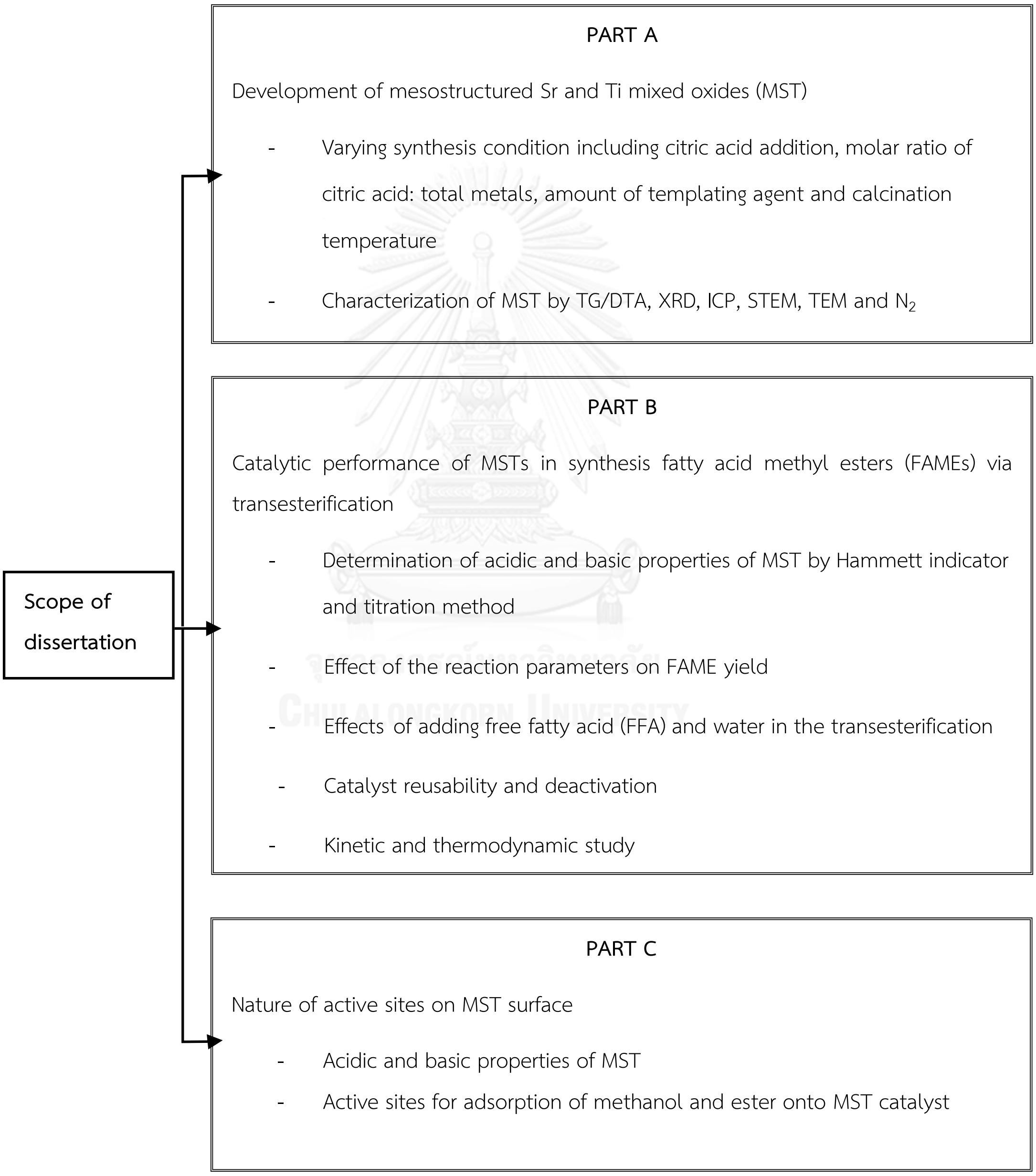

PART A

Development of mesostructured Sr and Ti mixed oxides (MST)

- Varying synthesis condition including citric acid addition, molar ratio of citric acid: total metals, amount of templating agent and calcination temperature
- Characterization of MST by TG/DTA, XRD, ICP, STEM, TEM and N_2

PART B

Catalytic performance of MSTs in synthesis fatty acid methyl esters (FAMEs) via transesterification

- Determination of acidic and basic properties of MST by Hammett indicator and titration method
- Effect of the reaction parameters on FAME yield
- Effects of adding free fatty acid (FFA) and water in the transesterification
- Catalyst reusability and deactivation
- Kinetic and thermodynamic study

PART C

Nature of active sites on MST surface

- Acidic and basic properties of MST
- Active sites for adsorption of methanol and ester onto MST catalyst

Figure 1.1 Experimental framework of this study.

CHAPTER II

Theory and literature reviews

2.1 Strontium titanate ($SrTiO_3$)

2.1.1 Properties of $SrTiO_3$

Strontium titanate ($SrTiO_3$) (IUPAC name: strontium (2+) oxotitanium bis(olate)) is an important member of perovskite-type multimetal oxides. $SrTiO_3$ crystallizes in the ABO_3 cubic perovskite structure (space group *Pm3m*) with a lattice parameter of 0.3905 nm and a density of 5.12 g cm^{-1} at room temperature [21]. The ideal crystal structure of cubic $SrTiO_3$ perovkite is shown in Figure 2.1. Metal cations in A (Sr^{2+}) and B (Ti^{4+}) sites are located in the 12- and 6-coordinated environments with O anions, respectively. Within the TiO_6 octahedra possessed hybridization of the O-2p states with the Ti-3d states leads to a pronounced covalent bonding [22]. On the other hand, Sr^{2+} and O^{2-} ions exhibit ionic bonding character. Hence, $SrTiO_3$ has mixed ionic-covalent bonding properties. This nature of chemical bonding leads to a unique structure, which make it a model electronic material. The physicochemical properties of $SrTiO_3$ are summarized in Table 2.1

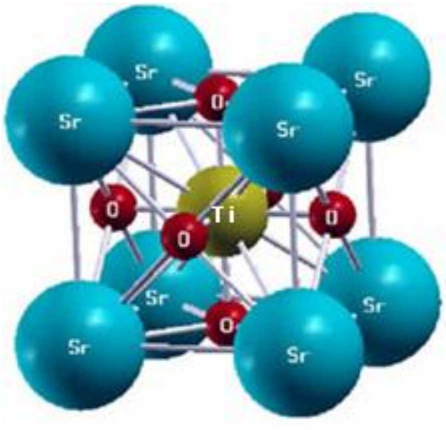

Figure 2.1 Crystal structure of perovskite $SrTiO_3$ [23].

Table 2.1 Physicochemical properties of cubic perovskite $SrTiO_3$ at room temperature [21]

Property	Value
Lattice parameter (nm)	0.3905
Atomic density (g cm^{-3})	5.12
Molar mass (g mol^{-1})	183.5
Melting point (°C)	2080
Mohs hardness	6
Dielectric constant (ε_0)	300
Thermal conductivity (W $(m.K)^{-1}$)	12
Coefficient of thermal expansion (Å $(°C)^{-1}$)	$9.4x10^{-6}$
Electronic band gap (eV)	3.2
Refractive index	2.31–2.38

The atomic arrangements for axial direction in $SrTiO_3$ are illustrated in Figure 2.2. For any given planar direction (h k l) of a perovskite structure, there are always two distinct types of alternating equally spaced atomic planes with different densities of Sr, Ti and O atoms. For instance, the (100) $SrTiO_3$ surface exhibits two different types of atomic alternating planes. One is terminated by a TiO_2 plane and another by a SrO plane [24]. Therefore, $SrTiO_3$ possesses both acid and basic surface characters on their surface due to acidity and basicity of TiO_2 and SrO, respectively.

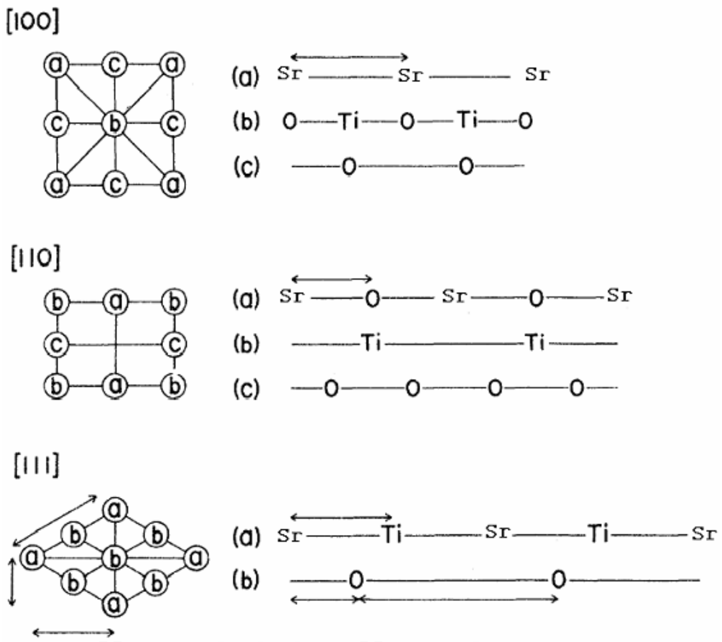

Figure 2.2 Atomic arrangements for [100], [110] and [111] axial directions in $SrTiO_3$ [22].

2.1.2 Synthesis of $SrTiO_3$

Conventionally, $SrTiO_3$ is synthesized via a solid-state reaction of $SrCO_3$ and TiO_2 at high temperature (>1000 °C), which not only consumes a lot of energy but also results in particle-size non-uniformity and compositional inhomogeneity [14]. The XRD patterns and SEM micrographs of $SrTiO_3$ synthesized by solid state reaction and molten salts method are presented in Figure 2.3.

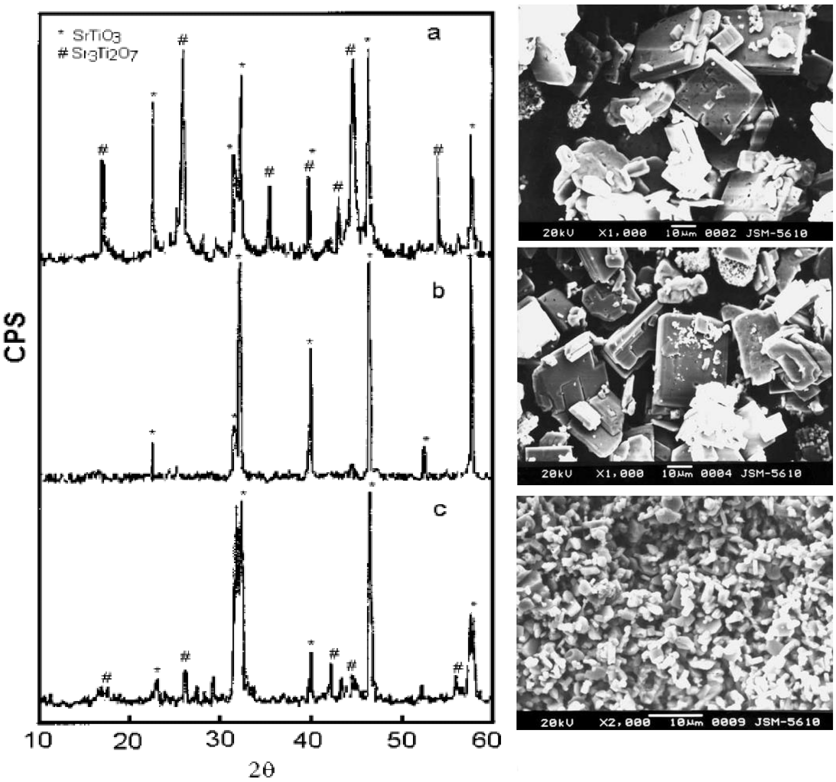

Figure 2.3 XRD patterns and SEM micrographs of $SrTiO_3$ synthesized using molten salts method various calcination conditions (a) 1300 °C for 4 h, (b) 1200 °C for 4 h and (c) conventional $SrTiO_3$ synthesized by solid state reaction [14].

In the past two decades, several synthesis techniques have been developed for preparation of $SrTiO_3$ nanoparticles with enhanced physicochemical properties, such as hydrothermal [14], ultrasonic spray pyrolysis [25], co-precipitation [26], polymeric precursor method [27], solvothermal method [28], combustion [16], sol-gel [15], and sol-gel combustion method [17, 29]. The sol-gel combustion method is widely used to prepare the nanomaterials with high purity and compositional homogeneity at relatively low crystallization temperatures when compared to conventional synthesis methods [29]. Liu et al. [17] synthesized the $SrTiO_3$ nanopowder via sol-gel combustion method using citric acid ($C_6H_8O_7$) as complexing agent and nitrate ions from metal precursors as oxidant. The process in which the $SrTiO_3$ phase generated can be described as follows.

$$C_6H_8O_7 + Sr^{2+} \longrightarrow C_6H_6O_7Sr + 2H^+ \quad (2.1)$$

$$2C_6H_8O_7 + Ti^{4+} \longrightarrow (C_6H_6O_7)_2Ti + 4H^+ \quad (2.2)$$

$$9Sr(NO_3)_2 + 5C_6H_8O_7 \longrightarrow 30CO_2 + 9N_2 + 20H_2O + 9SrO \quad (2.3)$$

$$9TiO(NO_3)_2 + 5C_6H_8O_7 \longrightarrow 30CO_2 + 9N_2 + 20H_2O + 9TiO_2 \quad (2.4)$$

$$SrO + TiO_2 \longrightarrow SrTiO_3 \quad (2.5)$$

Firstly, citric acid reacted with metal ions under acidic condition to achieve the stable complexes. Subsequently, amorphous metal oxide nanoparticles were formed via redox reactions of metal nitrates as oxidizing agent and citric acid as reducing agent. Due to exothermic nature of the reactions, heat released induced crystallization of amorphous SrO and TiO_2 via solid state reaction to obtain the crystalline $SrTiO_3$ phase. However, the synthesis of $SrTiO_3$ via the sol-gel combustion still has a major disadvantage, the presence of impurities phases because citric acid do not enough for interacting with metal ions in reaction mixture. Therefore, the obtained $SrTiO_3$ must be post-treated by washing with acid solution to remove the impurities [29]. The XRD patterns of $SrTiO_3$ synthesized via sol-gel combustion process before and after acid treatment are shown in Figure 2.4. Nevertheless, the $SrTiO_3$ materials attained by all of those methods exhibited low specific surface area ($<5\ m^2g^{-1}$) [12, 15] and porosity [15-17].

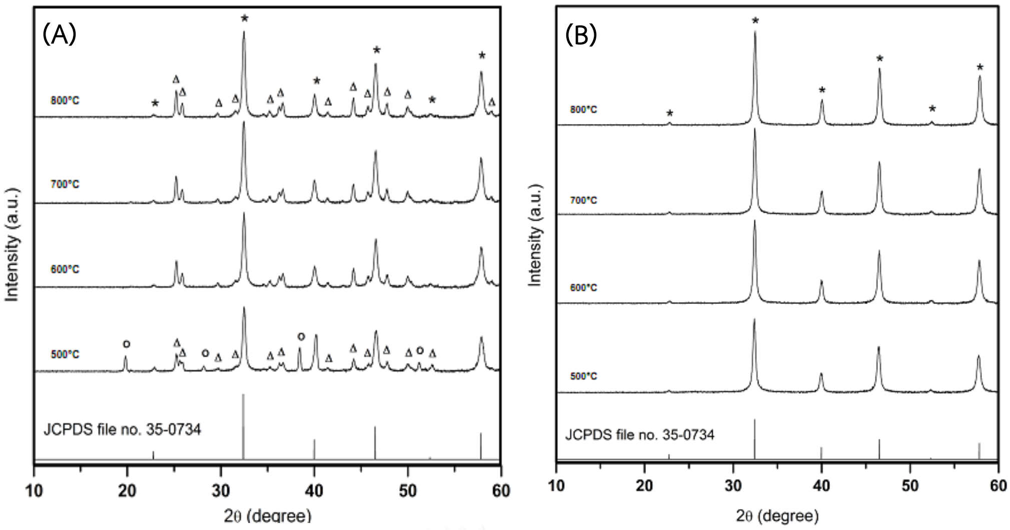

Figure 2.4 XRD patterns of $SrTiO_3$ synthesized via sol-gel combustion at various calcination temperatures (A) before acid treatment and (B) after acid treatment [29]. (★= $SrTiO_3$, ○ = $Sr(NO_3)_2$ and Δ= $SrCO_3$)

2.2 Mesoporous materials

Nanoporous materials have attracted a great deal of technological interests due to their desirable properties for wide range of applications, such as catalysts, molecular sieves, gas sensors, and energy conversion and storage [30-33]. According to the IUPAC definition, nanoporous materials can be divided into three categories based on pore sizes: pores with widths exceeding 50 nm are called macropores, pores with diameters in between 2 and 50 nm are called mesopores, and pores having widths of less than 2 nm are called micropores [34]. Examples of the materials categorized by these three different pore sizes are illustrated in Figure 2.5.

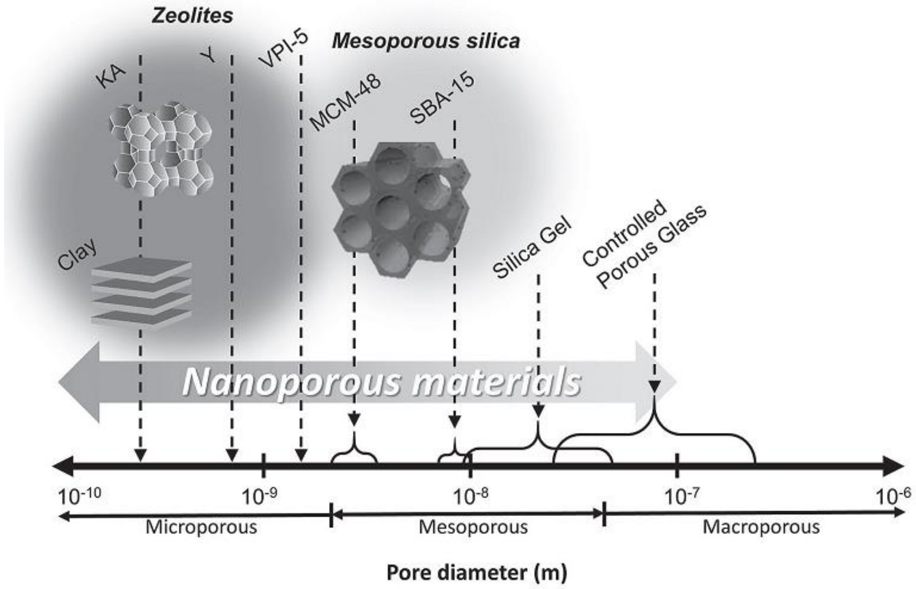

Figure 2.5 Classification of porous materials depending on their pore size [35].

After discovery of the first mesoporous material, MCM-41, synthesized by the Mobil researchers in 1992 [36, 37], much attention has focused on silica-based mesoporous materials because it possessed well 2D hexagonal pore structure ordering with a large surface area (600–1000 m^2 g^{-1}) and high pore volume (0.8–1.0 m^3 g^{-1}) [36, 37]. The TEM micrograph and low angle XRD pattern of MCM-41 are shown in Figure 2.6. However, MCM-41 is unstable due to its thin pore wall, compromising its potential application in catalysis, gas storage, and molecular filter [30, 33, 37]. Therefore, other mesoporous silica materials were synthesized to overcome these limitations.

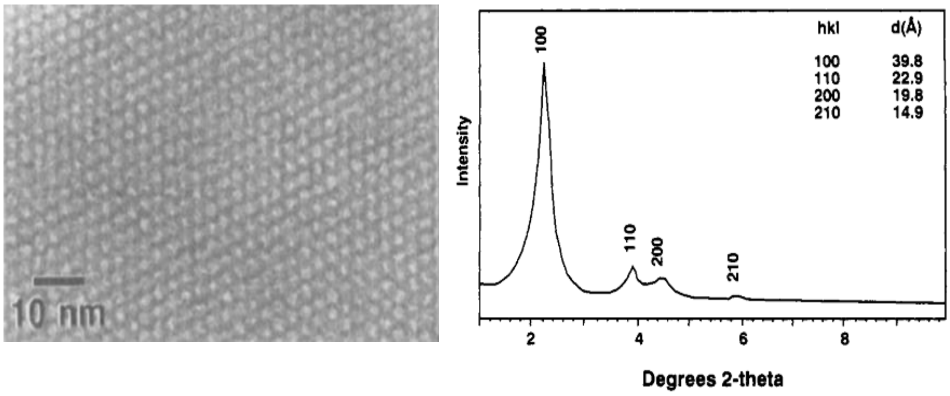

Figure 2.6 TEM image and low-angle XRD pattern of MCM-41 [37].

A new mesoporous silica, SBA-15, was firstly reported in 1998 [38]. It was synthesized using a tri-block copolymer of poly[ethylene oxide] and poly[propylene oxide] as a neutral templating agent. It possesses the same mesopore symmetry as MCM-41, but with larger pore diameter (~ 8 nm), thicker pore walls (~ 3 nm) and is higher hydrothermal stability [38]. Interestingly, SBA-15 exhibits disordered micropores in the walls, which is originated from the polymer template embedded in the silica walls during self-assembly process [39]. The TEM micrograph and low angle XRD pattern of SBA-15 are shown in Figure 2.7.

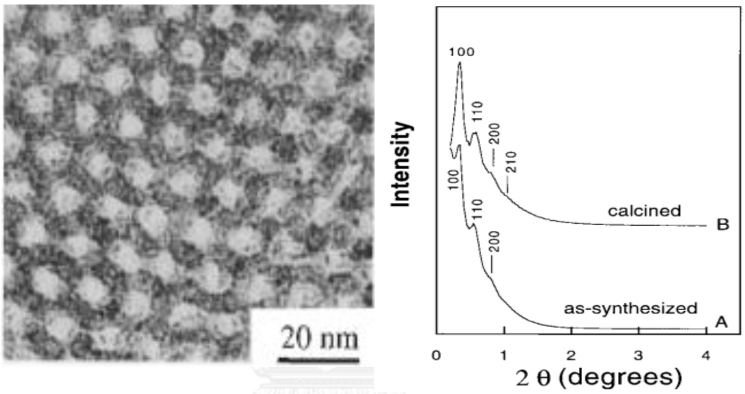

Figure 2.7 TEM image and low-angle XRD pattern of SBA-15 [38].

2.3 Mesoporous non-siliceous materials

As mesoporous silica materials exhibit neutral frameworks, they cannot provide catalytic activity for various chemical reactions. Moreover, most of silica-based mesoporous materials have amorphous walls, poor structural strength and stability, and limited applications. Currently, there is an obvious trend to synthesize mesoporous metal and transition metal oxides with crystalline or semicrystalline framework, which would bridge the gap between conventional high surface area mesoporous structure and active metal oxides. Owing to their fascinating physicochemical properties, including high electrical and thermal conductivity [40, 41], mesoporous non-siliceous materials offer a wide range of promising applications that cannot be achieved by siliceous mesoporous materials as summarized in Table 2.2.

Even though there have been many reports on successful preparation of mesoporous non-siliceous materials, keeping the integrity of mesostructure stability are still a challenging issue. Several main reasons for difficulty and complication in the synthesis of mesoporous non-siliceous materials can be explained as follows [42, 43]. Firstly, a high reactivity towards hydrolysis and condensation of non-siliceous metal precursors leads to undesirable phase separation between templating molecules and inorganic species, resulting in disordered porous gels. Next, the obtained structures are often unstable toward template removal and crystallization of metal species during thermal treatment as shown the simplified model in Figure 2.8. Finally, synthesis procedures are extremely sensitive to many external parameters, leading to irreproducible results.

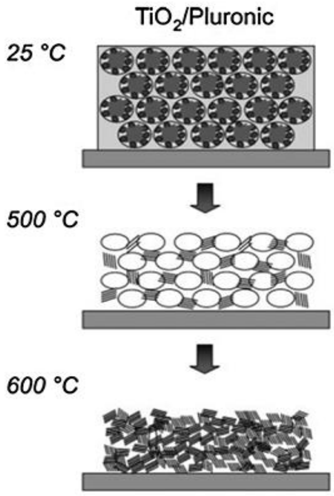

Figure 2.8 The simplified model for crystallization of mesoporous TiO_2 [43].

Table 2.2 Various applications of mesoporous non-siliceous materials [42]

Field	**Properties**	**Name of material**	**Application example**
Adsorption	Toxic ion adsorption	Mesoporous alumina	F, As(III), Cd(II), Cu(II), Zn(II) etc. adsorption to purify water
Catalysts	Redox	Mesoporous Ti-P mixed oxides	Partial oxidation of styrene, oxidation of cyclohexane to adipic acid
	Acid-base	Mesoporous Zn-Ti mixed oxides	Friedel-Crafts benzylation, esterification, tranesterification
	Photocatalysis	Mesoporous TiO_2	Photodegradation of dye, photosplitting of water
Optics, electricity, megnetism	Optical	Mesoporous WO_3	Chemosensing
	Optical Electronics	Mesoporous TiO_2 and ZnO	Photocurrent enhancement on dye doping
	Magnetism	Mesoporous Fe_3O_4	Ferromagnetism
Sensing	Gas sensing	Mesoporous SnO_2 and TiO_2	CO, NH_3, H_2, NO_2 etc. gas sensing

Mesoporous non-siliceous materials with semi-crystalline wall were firstly synthesized by Yang et al in 1998 [20]. Mesoporous metal oxides, including TiO_2, ZrO_2, Al_2O_3, Nb_2O_5, Ta_2O_5, WO_3, HfO_2, and SnO_2, and mesoporous mixed metal oxides, such as $SiAlO_{3.5}$, $SiTiO_4$, $ZrTiO_4$, Al_2TiO_5 and ZrW_2O_8, were prepared via sol-gel method using amphiphilic poly(alkylene oxide) block copolymers as structure-directing agents in non-aqueous solutions for organizing the network-forming metal-oxide species, for which inorganic salts serve as precursors. The TEM micrographs of mesoporous TiO_2 and ZrO_2 are shown in Figure 2.9. The partially hydrolyzed of metal chloride in ethanol generates $M(OEt)_nCl_m$ complexes with a low polymerization rate, which slowly react with water in air via hydrolysis. After hydrolysis, the resulting multivalent metal species can associate preferentially with hydrophilic poly[ethylene oxide] (PEO) moieties mediated by HCl to form mesostructure [44]. Hence, the materials attained are relatively thermally stable probably due to their thick inorganic walls. In addition, the most important feature is their semi-crystalline frameworks where nano-crystallites nucleate within the amorphous inorganic matrices.

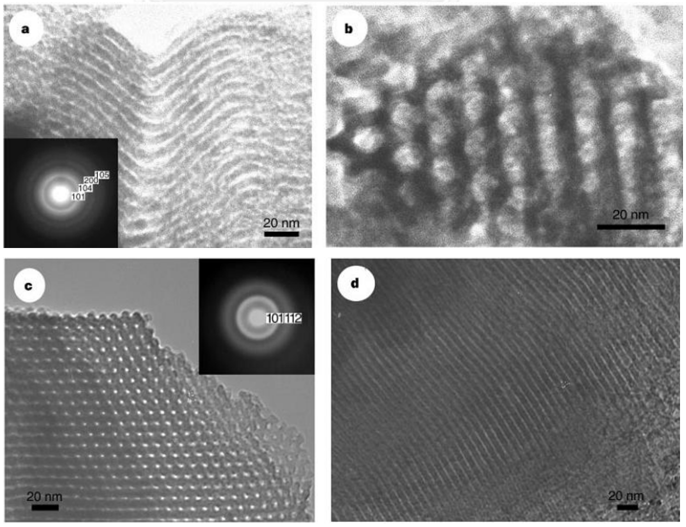

Figure 2.9 TEM micrographs of two-dimensional hexagonal mesoporous (a, b) TiO_2 and (c, d) ZrO_2 [44].

2.4 Formation of mesoporous materials: synthesis pathway and mechanism

The synthesis strategies for ordered mesoporous materials feature templating concepts which were proposed over twenty years ago [36-38]. Generally, the templates used for generation of mesopores can be simply classified into two classes. The first one is soft template, which is usually referred as structurally flexible surfactant molecules, for example cetyltrimethylammonium bromide (CTAB), sodium dodecyl sulphate (SDS), and block copolymers of poly[ethylene oxide] and poly[propylene oxide] The second is hard templates of which possesses well-ordered rigid frameworks, such as ordered mesoporous silica, carbon, and colloidal crystals. The roles of template in generating mesoporosity of materials via soft-template and hard-template pathways are explained in this section.

2.4.1 Soft-template method

The soft-templating method is the most successful pathway for the synthesis of mesoporous materials. In this method, organic surfactant molecules define a key role to template mesoporous structures via self-assembly route within inorganic matrices, and thus act as structure-directing agents (SDAs) [42]. The classification of SDAs as soft templates is illustrated in the Figure 2.10.

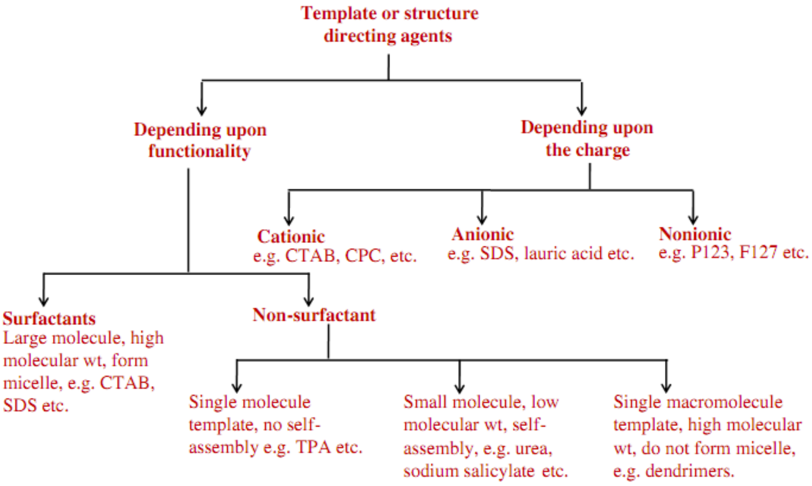

Figure 2.10 Schematic representation of various categories of soft-templates [42].

The SDAs can be grouped by the charge characteristic of their polar (hydrophilic) head groups as followed.

(1) Cationic surfactants possess a positive charge on their polar head group when dissociated in water. They include chemical classes such as amines, alkylimidazolines, alkoxylated amines, and quaternized ammonium compounds Examples of cationic surfactants are cetyltrimethylammoniumbromide or hexadecyltrimethylammonium bromide (CTAB), cetylpyridinium chloride (CPC), n-dodecyl pyridinium chloride. Molecular structure of respresentative cationic surfactants is shown in Figure 2.11.

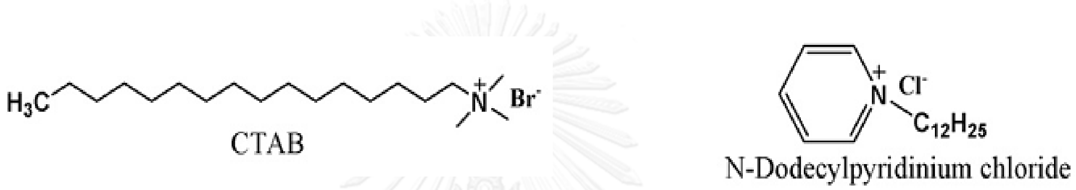

Figure 2.11 Molecular structure of cetyltrimethylammoniumbromide (CTAB) and n-dodecyl pyridinium chloride [42].

(2) Anionic surfactants dissociated in water into a negative charge on their polar head group. They include functional groups like carboxylic acids, sulfates, sulfonic acids, and phosphoric acid derivatives. Examples of anionic surfactant are sodiumdodecyl sulphate (SDS), sodiumdodecylbenzene sulphonate. Molecular structure of these anionic surfactants is presented in Figure 2.12.

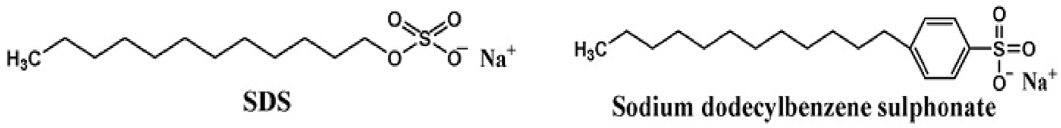

Figure 2.12 Molecular structure of sodiumdodecyl sulphate (SDS) and sodium dodecylbenzene sulphonate [42].

(3) Nonionic surfactants consist of hydrophilic and hydrophobic parts. The hydrophilic group is made up of water soluble moieties, rather than charged head group. Traditionally, hydrophilic part of nonionic surfactants consists of molecules with hydroxyl groups, for example poly[ethylene oxide](PEO). The hydrophobic part of surfactant consists of a long chain hydrocarbon that can be obtained from petrochemical source or naturally occurring fats and oils. [43] Commercial nonionic surfactants are listed in Figure 2.13.

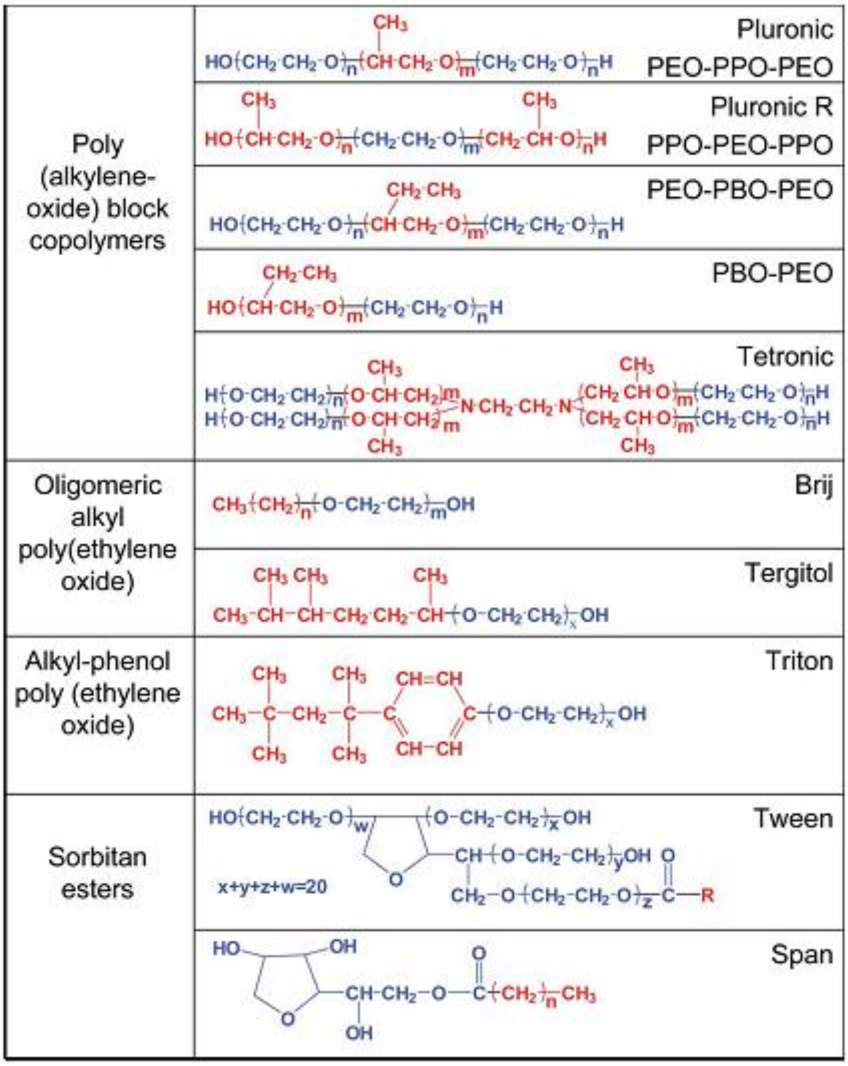

Figure 2.13 Classification commercial nonionic surfactants [44].

Six different synthesis pathways that reflect the metal-template molecular interaction have been readily employed to prepare ordered mesoporous materials under wide range of pH, temperatures and surfactant nature and their concentrations [42]. Table 2.3 summarizes types of interaction between template head group and inorganic precursor where S is the surfactant, I is the inorganic phase and X^- is the mediating anionic species, X^+ is intermediate cationic species, S^0 is neutral amine, I^0 is hydrated inorganic oligomer and N^0 is non-ionic template.

Table 2.3 Types of interaction between surfactant head group and inorganic precursor [42]

Surfactant type	Interaction pathway	Interaction type	Synthesis condition	Examples
Cationic (S^+)	Electrostatic interaction	S^+I^-	Basic	Tungsten oxide
		$S^+X^-I^+$	Acidic	Lamellar zinc phosphate
Anionic (S^-)	Electrostatic interaction	S^-I^+	Neutral or basic	Lamellar iron oxide
		$S^-X^+I^-$	Basic	Lamellar aluminum oxide and zinc oxide
Nonionic (S^0)	H-bonding interaction	S^0I^0	Neutral	Mesoporous zirconium oxide and tin oxide
Copolymer (N^0)	H-bonding interaction	N^0I^0	Acid	Mesoporous titanium oxide, and aluminum oxide

Figure 2.14 represents the soft-templating pathway leading to mesoporous non-siliceous materials. The synthesis of mesoporous non-siliceous materials via solf template pathway consists of four steps. Firstly, surfactant molecules are spontaneously formed to micelle when synthesis mixture possesses surfactant concetration higher than citrical micelle concentration (CMC). Secondly, the mesophases are formed by the interaction between hydrolized metal precusor and the head group of the organic micelle, that is driven by weak non-covalent bonds such as hydrogen bonds or Van der waal bond. With the evaporation of the solvent, the surfactant become high concentration and then generated a liquid-crystal phase in the presense of inorganic species, leading to mesostructure composites. Finally, the inorganic frameworks can be further phase transformed to metal oxides by post treatment and the surfactants as the soft-templating agent can be easiliy removed by calcination [45].

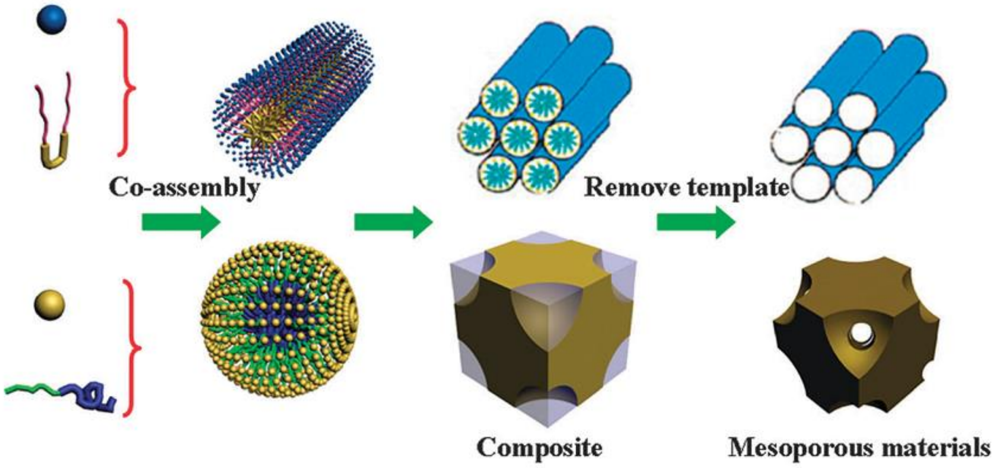

Figure 2. 14 Schematic representation of the soft-templating pathway leading to mesoporous non-siliceous materials. Different kinds of templates co-assembling with inorganic species can form different mesostructures [45].

Mesoporous non-siliceous materials prepared by soft-template have their advantages and disadvantages. The synthesis via soft-template route is easy compared to the hard template. Also low temperature is often employed. However, the products resulting from the soft template method, just like the silica materials prepared by similar approaches, usually have amorphous or semi-crystalline walls and poor thermal stability, which greatly limits their applications. [20, 46] Using specially designed polymer template such as KLE, crystalline metal oxides could be obtained, but all these syntheses are based on complicated sol-gel processes, the hydrolysis and polymerization of the transitional metal ions are difficult to control [47, 48].

2.4.2 Hard template method

Since mesoporous non-siliceous materials with highly crystalline framework cannot be prepared by the soft-templating route, researchers have developed various mesoscaled materials by the hard-templating route, also known as nanocasting technology. The principle of the hard-template pathway to synthesize mesoporous non-siliceous materials which involves four main steps is represented in Figure 2.15: (1) template preparation; (2) impregnating an inorganic precursor into the pore system of the template; (3) heating or other treatment to transform the precursor into the target product; and (4) template removal [45].

Generally, there are several advantages associated with mesoporous materials obtained by hard templating as follows [49]:

(1) The replica materials as hard template usually have three-dimensional (3-D) connected frameworks. Alternatively, nanowire arrays are connected by small pillars formed from the micro- or mesochannels inside the pore walls of the templates, leading to the high surface areas and uniform pore size distributions of these materials.

(2) After incipient wetness impregnation of the voids of the template with the precursors, the precursor should be easily converted to the desired composition with as little volume shrinkage as possible. The nanostructured materials with crystalline or even single crystal frameworks can be obtained by high temperature treatment while still be protected by the template.

(3) The synthesis strategy circumvents the necessity to control the hydrolysis–condensation process of the inorganic species and the cooperative assembly of surfactants and inorganic species, making it suitable for a wide variety of materials.

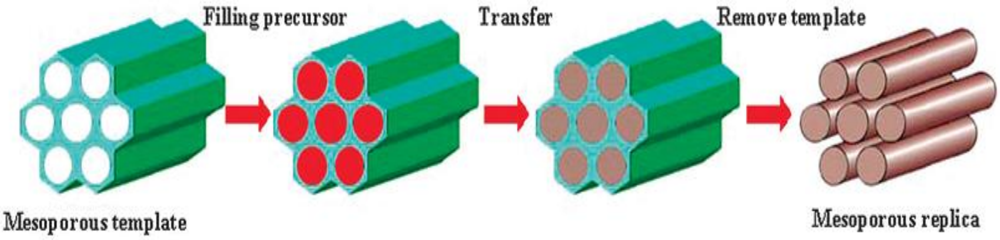

Figure 2.15 Schematic representation of the hard-templating (nanocasting) pathway leading to mesoporous non-siliceous materials [45].

Many mesoporous silicas or mesoporous carbons have been used as hard templates, such as MCM-48, SBA-15, KIT-6, and CMK-3, with or without surface modification. The first preparation of 3D highly crystalline porous transition metal oxides via hard-template method was reported by Zhu et al.[50], in which amine functionalized SBA-15 was used as the hard template. Mesoporous single crystalline Cr_2O_3 with highly ordered pores was obtained, consisting of nanowire arrays connected by short bridges as shown in Figure 2.16 Later, several other mesoporous metal oxides were prepared with a similar method, such as, WO_3 [51], and Fe_2O_3 [52].

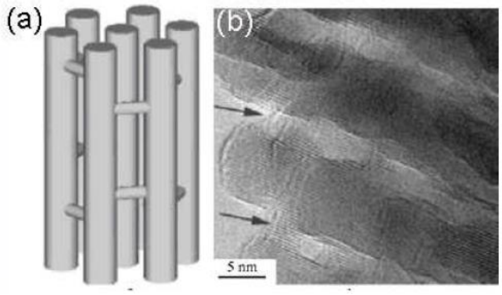

Figure 2.16 (a) Mesostructure model and (b) HRTEM image for mesoporous Cr_2O_3. The arrows indicate the small bridges between the wires [50].

Although the hard-template procedure offers a number of advantages, this method also has its disadvantages. Firstly, the mesoporous metal oxide materials must be stable to NaOH or HF solutions used to remove the silica template. For example, the synthesis of pure mesoporous MgO has not been possible using mesoporous silica [53]. Secondly, a solution step is still required as the means of introducing the transition metal precursor and this limits the range of materials to those stable in solution. Also, materials for which the precursors react with the mesoporous silica cannot be synthesized (e.g. lithium). While using mesoporous carbon as the hard template, one predominant disadvantage is the poor wetting of the pore walls by the aqueous precursor solution. To some extent, the post-synthesis reduction and post-synthesis solid-solid conversion enable preparation of low-valence metal oxides and lithium containing compound, greatly enriching the range of mesoporous materials and their applications [54, 55].

2.4.3 Combination of soft and hard template method

The main problem for ordered amorphous mesoporous metal oxide is the stability of the mesostructure during crystallization, thus a silica/carbon enforcement method was developed, which combines the advantages of the hard and soft template method. In this way highly crystalline ordered mesoporous Nb_2O_5, Ta_2O_5, $(Ta, Nb)_2O_5$ and $TiNb_2O_6$ have been obtained [56]. Figure 2.16 presents the general concept for reinforcement of the pore walls in order to retain the amorphous to crystalline transition during thermal treatment at high temperature. In procedure (a), the carbon source was filled and carbonized under nitrogen condition together with crystallized mesoporous metal oxide. Then, carbon as reinforcement was removed by calcination in air. The procedure (b) is to strengthen the mesostructure by coating. The internal and external surfaces of amorphous mesoporous materials are covered by silica layers and then crystallization by calcination in air. Finally, the silica layers are digested by treatment with hydrofluoric acid or alkaline solution.

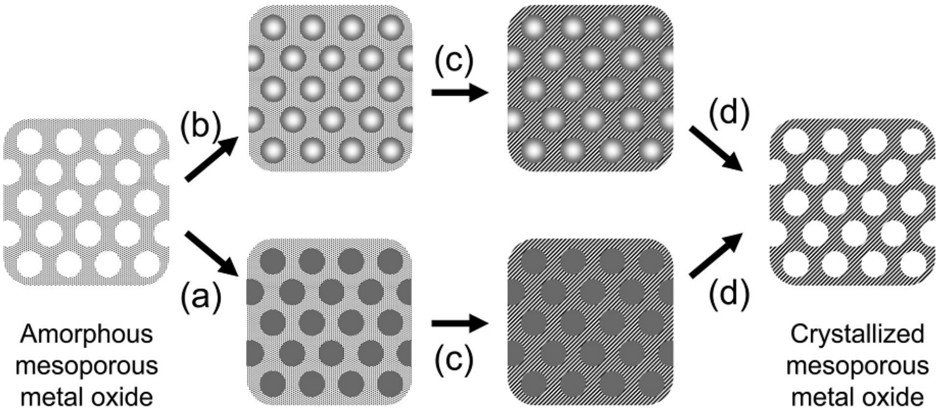

Figure 2.17 Schematic illustration of the strategy for reinforced crystallization of mesoporous metal oxides: (a) back filling, (b) coating, (c) crystallization, and (d) removal of the reinforcement. [56].

Moreover, Lee et al. [57] reported the preparation of ordered crystalline TiO_2 and Nb_2O_5 in a one-pot synthesis using block copolymers with an sp^2 hybridized carbon-containing hydrophobic block as the structure-directing agents, which converted to amorphous carbon material under appropriate heating conditions. The obtained *in-situ* carbon is sufficient to act as a rigid hard template keeping the pores of the oxides intact while crystallizing at high temperatures. Therefore, it exhibited combined assembly by soft and hard (CASH) chemistries. The schematic representation of CASH method is illustrated in Figure 2.18. This method can be used to obtain highly crystalline, mesoporous transition-metal oxides through high-temperature heat treatments that were otherwise not possible without collapse of the mesostructure.

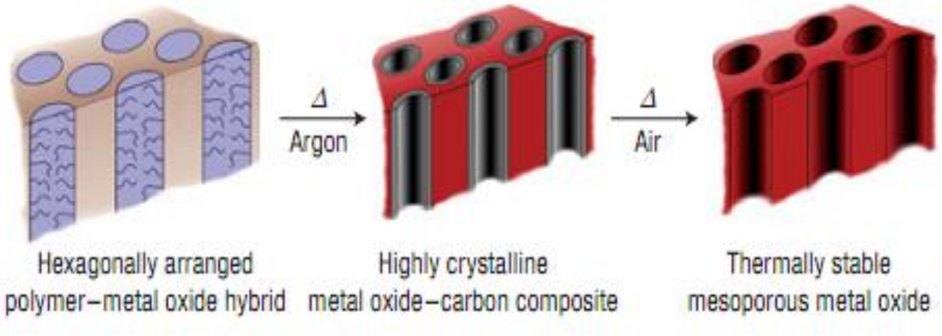

Figure 2.18 Schematic representation of CASH method [57].

2.5 Fatty acid methyl esters (FAMEs)

Fatty acid methyl esters (FAMEs) are the important bio-based intermediates in various industries, such as biofuels, biolubricants, detergents, cosmetics and pharmaceuticals [58-60]. Biodiesel, as main application of FAME, is a clean-burning fuel derived from vegetable oils or animal fats ,and is an advantageous alternative to fossil diesel fuel because of its biodegradability, bio-renewable nature, very low sulfur content and toxicity, low volatility or flammability, good transport and storage properties, higher cetane number, and its salutary atmospheric CO_2 balance for production [61]. The comparative standard in fuel properties of biodiesel and diesel from fossil source are compared in Table 2.4.

Table 2.4 The standard in fuel properties of biodiesel and fossil-diesel [62]

Property	Diesel	Bioiesel
Fuel standard	ASTM D975	ASTM PS 121
Fuel composition	C10–C21	C12–C22
Lower heating value (MJ/m^3)	36.6 x 10^3	32.6 x 10^3
Specific gravity, at 15°C	0.85	0.88
Kinematic viscosity (mm^2/s), at 40°C	1.3–4.1	1.9–6.0
Moisture content (wt.%)	0.161	<0.05
Iodine value	-	<120
Flash point (°C)	60–80	100–170
Cloud point (°C)	(-15)–5	(-3)–12
Pour point (°C)	(-35) –(-15)	(-15)–10
Cetane number	40–55	>51
Carbon (wt%)	87	77
Hydrogen (wt%)	13	12
Oxygen (wt%)	0	11
Sulfur (wt%)	<0.05	0–0.0024
FAMEs content (%)	-	96.5

2.5.1 Synthesis of FAME

Transesterification process has been widely used to produce FAME from triglycerides (fat or oil) with methanol [61]. Transesterification is the general term used to describe the important class of organic reactions, where an ester is transformed into another through interchange of the alkoxy moiety. When the original ester is reacted with an alcohol the transesterification process is called alcoholysis. The general equation for transesterification is shown in Eq. (2.6) [63].

$$\mathrm{RCOOR'} + \mathrm{R''OH} \xrightleftharpoons{\textit{catalyst}} \mathrm{RCOOR''} + \mathrm{R'OH} \tag{2.6}$$

Since transesterification reaction is reversible, the molar ratio of alcohol: ester is one of the main factors that influence the yield of product. Therefore, an excess of alcohol is used to drive the reaction forward. However, an excessive amount of alcohol makes glycerol recovery difficult, much energy used for alcohol recovery. Ideal alcohol/ester ratio has to be established empirically, considering each individual process [2, 61, 63].

The reaction temperature clearly influences the yield of FAME product. A higher reaction temperature can reduce the viscosities of precursors, and results in an increased reaction rate. However, some research groups found that when the reaction increases beyond the optimal level, the yield of the FAME product decreases because a higher reaction temperature accelerates the saponification reaction in case of alkali catalyzed tranesterification [58].

In case of reaction time, FAME yield increases with reaction time. At the beginning, the reaction rate is slow because of the mixing dispersion of methanol into oil. Then, the reaction proceeds faster. However, excess reaction time will lead to a reduction in the FAME yield due to backward reaction of transesterification, which tends to produce more fatty acids to form soaps [58].

The amounts of catalyst used in the transesterification reaction have the optimum amount so that its low amount in the reaction causes it to remain incomplete and its extra amount leads to induce the soap formation. Moreover, in case of heterogeneous catalysis, the large amount of catalyst reduced the mass transfer in reaction system due to viscosity in synthesis mixture increased [58]. Thus, the suitable amount of catalyst depends on the operational conditions and the type of catalyst.

2.5.1.1 Homogeneous catalysis of transesterification

Transesterification reaction can be catalyzed by both acid and basic catalysis However, tranesterification reaction conventionally used alkali catalysts such as alkaline metal alkoxides and hydroxides [2, 61, 64] because of its higher activity and less corrosive than acidic catalysis [64]. The reaction mechanism for alkali-catalyzed transesterification was formulated as four steps as present in equations 2.7–2.10 [63]. The first step (Eq. (2.7)) is the reaction of the base with the alcohol, producing an alkoxide and the protonated catalyst. The nucleophilic attack of the alkoxide at the carbonyl group of the triglyceride generates a tetrahedral intermediate (Eq. (2.8)), from which the alkyl ester and the corresponding anion of the diglyceride are formed (Eq. (2.9)). The latter deprotonates the catalyst, thus regenerating the active species (Eq. (2.10)), which is now able to react with a second molecule of the alcohol, starting another catalytic cycle. Diglycerides and monoglycerides are converted by the same mechanism to a mixture of alkyl esters and glycerol.

$$\mathrm{ROH} + \mathrm{B} \rightleftharpoons \mathrm{RO^-} + \mathrm{BH^+} \qquad (2.7)$$

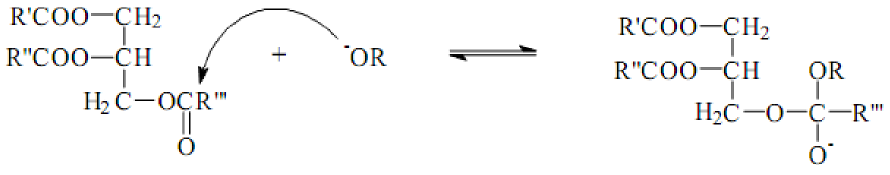

(2.8)

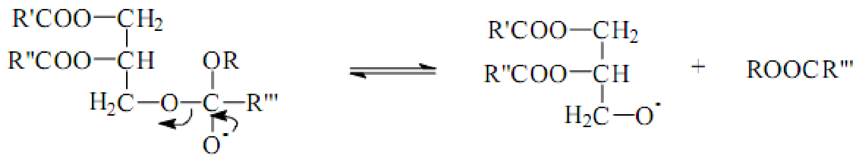

(2.9)

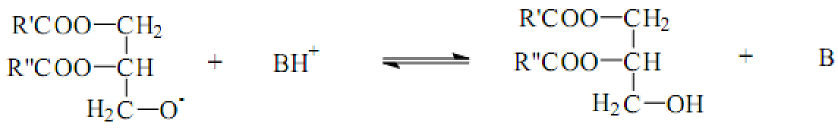

(2.10)

2.5.1.2 Heterogeneous catalysis of transesterification

Many previous works reported that the use of homogeneous catalysts results in undesirable effects when free fatty acids and/or water are present in feedstock, leading to formation of soap and lowering the FAME yield [61]. Moreover, the transesterification via homogeneous catalysis has several drawbacks, for example, difficulty of catalyst removal, a large amount of wastewater discharged, environmental pollution and contaminated glycerol. An alternative method for the FAME production is to use heterogeneous base catalysts. The general advantages of using these catalysts are separation easiness, less soap formation and catalyst reusability [61]. Various types of metal oxides have been investigated as solid base catalysts in the transesterification of triglycerides with methanol to produce FAME [6-10].

Heterogeneously basic catalysis for the transesterification of triglycerides with methanol can be explained by Eley-Rideal mechanism [7]. In the first step (Eq. (2.11)), basic oxygen species subtracts H^+ from methanol to form surface methoxide ion (CH_3O^-), which is a strong nucleophile in the reaction. Subsequently, the carbonyl carbon of the ester molecule attracts the methoxide ion from the surface of catalyst, forming a tetrahedral intermediate as shown in Eq. (2.12). In the next step, the tetrahedral intermediate picks up H^+ from the catalyst surface (Eq. (2.13)). The intermediate can also react with other methanol molecule to generate new methoxide ion as shown in Eq. (2.14). Finally, the tetrahedral intermediate rearranges to form methyl ester. According to Eq. (2.11), the ability of metal oxide to form the methoxide ion on the surface depends on the strength of Lewis basic sites presenting in the metal oxide catalysts. Their basic strength is related to electronegativity (EN) of metal atom that ionically bonds with oxygen atom. The lower the EN of metal atom is, the more the basic strength of the resulting metal oxide is increased. Besides the basic strength, other properties, such as elemental composition, crystalline structure, surface area, porosity, particle size and active site concentration, strongly influence the catalytic performance of metal oxide in the transesterification reaction.

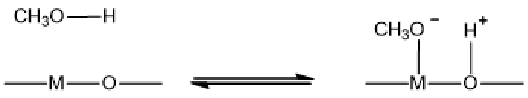

(2.11)

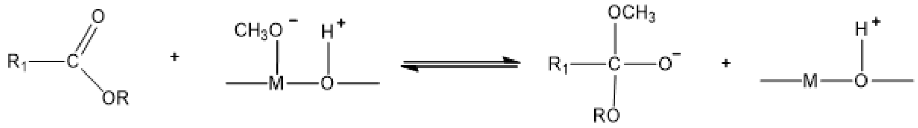

(2.12)

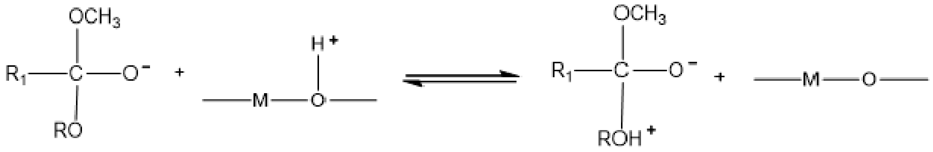

(2.13)

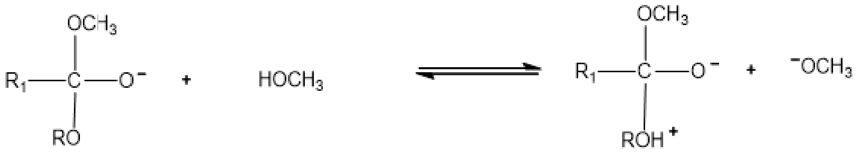

(2.14)

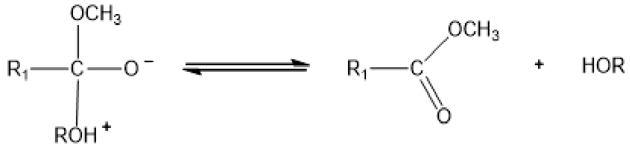

(2.15)

2.6 Literature reviews

2.6.1 Synthesis of $SrTiO_3$ and mesostructured Sr and Ti mixed oxides (MST)

Klaytae *et al*. [29] focused on preparing the $SrTiO_3$ nanocrystalline by sol-gel combustion method. The effects of molar ratio of total metal nitrates: citric acid and calcination temperature on the structural properties of resulting materials were investigated. The XRD data indicated that the content of perovskite $SrTiO_3$ increased by the amount of citric acid added and the calcination temperature. The results showed that the highest percent of perovskite phase of $SrTiO_3$ was obtained at the molar ratio of total metal nitrates: citric acid =1: 3 and the calcination temperature = 800 °C. However, $SrCO_3$ as a minor phase was detected. An acid post-treatment process using 1 M of nitric acid solution was applied to removal of the impurity phase.

Grosso *et al*. [53] reported the success of synthesizing mesoporous $SrTiO_3$ thin film via evaporation-induced self-assembly (EISA) method using a specially designed nonionic block-polymer template (KLE3739) as structure-directing agent. The structural evolution of mesoporous networks during crystallization was proposed. The crystallization of amorphous starting materials with three-dimensional spherical mesopores was observed at around 600–660 °C above which the mesoporous structure was destroyed due to a sintering effect.

Zuo *et al.* [65] synthesized N-doped mesoporous $SrTiO_3$ (STON) with disordered wormhole-like mesopores via template-free synthesis method for photocatalysis application. In the synthesis process, glycine appears to function as coordinating reagent, N_2 source for N-doping and pore creator. The results showed that STON exhibits an enhanced absorbance in a broad UV-visible and its absorption edge red shifts by ca. 25 nm in comparison with commercial $SrTiO_3$ (STO). The corresponding E_g of STON and STO were 2.9 and 3.2 eV, respectively. Moreover, a large surface area of STON could enhance photocatalytic efficiency, which confirmed by a high activity in photodegradation of organic dyes under visible-light.

Puangpetch *et al*. [66] investigated the use of a sol-gel method with aid of the structure-directing surfactant for synthesis of mesoporous-assembly $SrTiO_3$ nanocrystals as photocatalysts. The effects of types of structure-directing surfactants, including laurylamine hydrochloride (LAHC), cetyltrimethyl ammonium bromide (CTAB) and cetyltrimethyl ammonium chloride (CTAC), on the textural and catalytic properties were examined. The pore size distribution was found to be narrow and unimodal when LAHC was used as the structure-directing surfactant. However, mesoporous-assembly $SrTiO_3$ possessed the lower specific surface area than commercial $SrTiO_3$. The photocatalytic activity depended on surface area, crystallinity, pore structure and molar ratio of structure-directing surfactant: tetraisopropyl orthotitanate as titanium precursor.

2.6.2 Transesterification over heterogeneous catalysts

Liu *et al*. [7] reported the success of synthesizing biodiesel from soybean oil with methanol using SrO as heterogeneous base catalyst. SrO was prepared via direct calcination of $SrCO_3$ at 1200 °C. The SrO catalyst possessed a high basic strength ($H\_=26.5$). The results showed that a biodiesel yield greater than 95 wt% was achieved within 30 min at 650 °C using 3 wt% catalyst adding and methanol: oil molar ratio of 12: 1. In addition, SrO catalyst had a good catalyst life time up to 10 cycles with only a slight decrease in biodiesel yield.

Dias *et al*. [8] synthesized biodiesel via transesterification of soybean oil with methanol over MgO supported SrO catalyst. The catalyst was prepared via wet impregnation, and then calcined at various temperatures. The effect of molar ratio of Sr: Mg and calcination temperature on the catalytic performance was investigated. The results showed that the basicity of catalyst increased by increasing Sr loading. However, the catalysts attained had $SrCO_3$ and $Sr(OH)_2$ as impurity phases. The X-ray diffraction (XRD) data indicated that the calcination temperature was a crucial factor in the catalyst preparation because impurity phases are only removed at high temperatures. Moreover, this catalyst revealed a drastic loss of activity after repetitive uses. The deactivation can be ascribed to Sr leaching as evidenced by means of XRD and energy dispersive X-ray spectroscopy (EDS).

Wen *et al*. [11] reported the preparation of TiO_2-MgO mixed oxides as heterogeneous base catalyst for the transesterification of waste cooking oil with methanol. The catalyst was prepared via sol-gel method and then calcined at various temperatures. The influence of molar ratio of Ti: Mg and calcination temperature on the catalytic activity was investigated. The results showed that the substitution of Ti ions into magnesia lattice on (200) plane generated defects on the mixed oxides surfaces. The defects on catalyst surfaces improved the catalytic activity. The best catalyst was consisted of the molar ratio of Ti: Mg at 1: 1 and calcined at 650 °C, which was obtained the biodiesel yield of 92.3 wt%. After regeneration, the activity of spent catalyst was slightly increased, probably as a result of an increase in specific surface area and average pore size diameter.

Rashtizadah *et al.* [15] focused on the preparation of Sr-Ti mixed oxide nanocomposites as heterogeneous base catalyst for transesterification of soybean oil with methanol. The catalyst was prepared *via* sol-gel method and then calcined at various temperatures. The effects of molar ratio of Sr: Ti and calcination temperature on structural properties of resulting catalysts were investigated. From the XRD data, Sr_2TiO_4 as an active phase increased with the calcination temperature. However, the XRD patterns indicated the mixed phases of $SrTiO_3$ and $SrCO_3$ as impurity phases. The specific surface area of catalyst attained was found to be 1.33 m^2 g^{-1}. The best catalyst was consisted of the molar ratio of Sr: Ti at 0.8: 1 and calcined at 965 °C. In addition, the reaction parameters, including molar ratio of methanol: oil, amount of catalyst, reaction temperature and reaction time, were examined. To achieve the conversion of oil >98% the transesterification was performed at molar ratio of methanol: oil =15: 1, catalyst loading =1 wt%, reaction temperature =60 °C and reaction time =15 min.

2.6.3 Nature of active sites of metal oxides

Rabuffetti *et al.* [67] examined the surface acidity by chemisorption of pyridine followed by means of visible Raman and DRIFT spectroscopy of $SrTiO_3$ samples synthesized via three different methods, including, solid-state reaction, molten salt, and sol-precipitation–hydrothermal treatment. Raman and DRIFT spectra of pyridine chemisorbed on $SrTiO_3$ samples demonstrate the weak Lewis acid character of these surfaces, as well as the absence of Brønsted acid sites. It is clear from chemisorption of pyridine that the differences in surface acidity are rather slight, the surface of $SrTiO_3$ grains consisting of a mixture of SrO-based and TiO-based terminations, regardless of the synthetic approach employed in their preparation.

Navajas *et al.* [68] studied the nature of basic sites by chemisorption of methanol followed by diffuse reflectance infrared Fourier transform spectroscopy (DRIFTS) on Mg–Al hydrotalcites for methanolysis of vegetable oils. The correlation between basic sites and oil conversion was also investigated. The results showed that methanol adsorbed on Mg–Al hydrotalcites with different species, including species I (monodetate adsorption), species II (bidentate adsorption), and species H (hydrogen bonding). The total amount of methoxy species formed after methanol adsorption is related to the basicity of the sample. Interestingly, a linear correlation between the amount of adsorbed methanol on Mg–Al hydrotalcites with species I and the catalytic activity in the biodiesel production was found. Therefore, it should be proposed that monodentate adsorption of methanol on catalyst surface was mainly involved in the transesterification reaction.

CHAPTER III

Experimental and analytical method

3.1 Materials

3.1.1 Chemicals for synthesis mesostructure Sr and Ti mixed oxides (MST)

- Strontium nitrate ($Sr(NO_3)_2$) (AR grade, 99%, Wako)
- Titanium butoxide ($Ti(OC_4H_9)_4$) (AR grade, 97% Wako)
- Citric acid ($C_6H_8O_7$) (AR grade, 99%, Wako)
- Pluronic® P123 (Mn = 5800 g mol^{-1}, AR grade, Aldrich)
- Super-dehydrated ethanol (C_2H_5OH) (AR grade, 99.5%, Wako)
- Hydrochloric acid (HCl) (AR grade, 37%, Merck)
- Deionized water

3.1.2 Chemicals for determining of acidity and basicity of MST

- Thymol blue (pk_a = 2.8)
- Methyl yellow (pk_a = 3.3)
- Methyl red (pk_a = 4.8)
- Neutral red (pk_a = 6.8)
- Bromothymol blue (pk_a = 7.2)
- Phenolphthalein (pk_a = 9.8)
- 2,4-Dinitroaniline (pk_a = 15.0)
- n-Buthylamine ($CH_3(CH_2)_3NH_2$) (AR grade, 99.5%, Sigma-Aldrich)
- Super-dehydrated benzene (C_6H_6) (AR grade, 99.5%, Wako)
- Benzoic acid ($C_7H_6O_2$) (AR grade, 99%, Aldrich)

- Super-dehydrated methanol (CH_3OH) (AR grade, 99.5%, Wako)

3.1.3 Chemicals for transesterification reaction

- Refined bleach deodorized palm kernel oil; PKO (Chumporn Palm Oil Industries)
- Methanol (CH_3OH) (Commercial grade, 99.8%, Zen point)
- Oleic acid ($CH_3(CH_2)_7CH=CH(CH_2)_7COOH$) (65–88 %, Sigma-Aldrich)
- Sodium sulfate (Na_2SO_4) (AR grade, 99%, Aldrich)

3.1.4 Chemicals for reaction product analysis

- Methyl heptadecanoate ($C_{18}H_{36}O_2$) (Standard grade, 99.5%, Fluka)
- n-Heptane (C_7H_{16}) (AR grade, 99.9%, Merck)

3.1.5 Chemicals for determining of nature of catalytically active sites on MST

- Anhydrous pyridine (C_5H_5N) (AR grade, 99.8%, Sigma-Aldrich)
- Pyrrole (C_4H_5N) (AR grade, 98%, Sigma-Aldrich)
- Super-dehydrated methanol (CH_3OH) (AR grade, 99.5%, Wako)
- Ethyl propionate ($CH_3CH_2COOC_2H_5$) (AR grade, 99%, Sigma-Aldrich)

3.2 Instruments and equipment

- Beakers, 100, 250 and 500 mL
- Volumetric flasks, 250 and 500 mL
- Droppers
- Spatulas
- Test tubes

- Burettes, 50 mL
- Crucibles
- Magnetic bars
- Hot plate stirrers
- Thermocouples (model: ETS-D5)
- Filter papers, No. 42
- Micro pipettes
- Electric oven
- Silicone oil bath
- Muffle furnace
- Desiccator
- PTFE-lined autoclave reactor
- Centrifuge
- Rotary evaporator

3.3 Preparation of mesostructure Sr and Ti mixed oxides (MSTs)

MSTs were synthesized via neutral-templated self-assembly sol-gel combustion method. Typical synthesis of MST was carried out as follow; Pluronic P123 (0.17 mmol) was dissolved in super-dehydrated ethanol (12 g) and a mixture of $Ti(OC_4H_9)_4$ (10 mmol) and HCl (16 mmol) was added dropwise into this solution. To this solution an aqueous solution containing $Sr(NO_3)_2$ (10 mmol) and citric acid (20 mmol) was gradually dropped. After vigorously stirring at room temperature for 3 h, the resulting solution was dried in oven at 100 °C overnight. The as-synthesized material was calcined for crystallization at 600 °C for 4 h in a muffle furnace. The white powder obtained is denoted as MST-*x*C-*y*P(*z*), where *x* is the molar ratio of citric acid: total metals, *y* is mmol of Pluronic P123 used, and *z* is the calcination temperature in degree Celsius or as-syn for material without calcination. The synthesis condition including chemical reagent in synthesis mixture and calcination temperature are summarized in Table 3.1.

Table 3.1 Synthesis conditions of different MSTs

Sample	Composition of synthesis mixture (mmol)							Calcination temp. (°C)
	$Ti(OC_4H_9)_4$	$Sr(NO_3)_2$	Citric acid	Pluronic P123	HCl	H_2O	C_2H_5OH	
MST-0C-0.17P(600)	10	10	0	0.17	16	667	375	600
MST-0.5C-0.17P(600)	10	10	10	0.17	16	667	375	600
MST-1C-0.17P(600)	10	10	20	0.17	16	667	375	600
MST-2C-0.17P(600)	10	10	40	0.17	16	667	375	600
MST-1C-0P(600)	10	10	20	0	16	667	375	600
MST-1C-0.34P(600)	10	10	20	0.34	16	667	375	600
MST-1C-0.17P(500)	10	10	20	0.17	16	667	375	500
MST-1C-0.17P(700)	10	10	20	0.17	16	667	375	700
MST-1C-0.17P(800)	10	10	20	0.17	16	667	375	800

3.4 Material characterization procedure

3.4.1 Structural analysis

Powder X-ray diffraction (XRD)

X-ray powder diffraction (XRD) is a unique and non-destructive method in determination of crystal structure and crystallinity of a sample. The conditions for constructive interference are derived from the simple geometrical picture for the scattering of an X-ray beam by planes of atoms in a crystal, shown in Figure 3.1. Imagine the X-ray beam of wavelength λ, incident on the crystal at an angle θ with respect to equidistant h k l lattice-planes, with interplanar distance d_{hkl}. This condition is summarized in the Bragg's law.

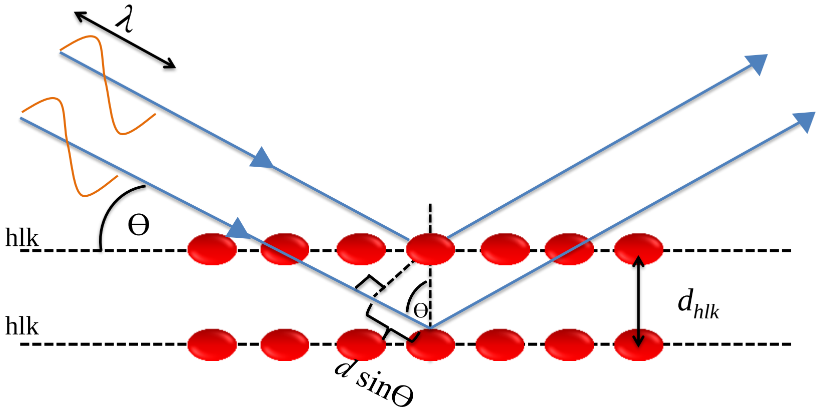

Figure 3.1 Diffraction of X-ray by regular planes of atoms.

Braggs' law is able to determine the interplanar spacing of the samples, from diffraction peak according to Bragg's angle using Eq. (3.1).

$$n\lambda = 2d\sin\theta \tag{3.1}$$

where n = integer

λ = wavelength of the X-rays, Å

d = interplanar spacing, Å

θ = the diffraction angle.

In this work the structural properties of synthesized MST were characterized at room temperature by on a Rigaku Ultima III X-ray diffractometer equipped with a Cu Kα radiation at 40 kV voltages and 40 mA current, shown in Figure 3.2. The diffraction angle was started from 2θ of 10° to 80° with a scanning step of 0.02° and a count time of 1 sec. The results shown in term of XRD pattern which plot between the angle 2θ and signal count (count per second, cps). The XRD data showed crystalline phase of sample that were compared with library patterns database.

Moreover, the data from XRD pattern gave unit cell parameter using Lattice's equation and average crystalline size using Scherrer's equation.

Figure 3.2 Rigaku Ultima III X-ray diffractometer.

Since the $SrTiO_3$ is cubic crystals. Therefore, the unit cell parameter in this study calculated by Lattice's equation, shown in Eq. (3.2).

$$a_0 = d_{hkl} \times \sqrt{h^2 + k^2 + l^2} \qquad (3.2)$$

where a_0 = unit cell parameter, Å

d_{hkl} = interplanar spacing, Å

h,k,l = Miller indexes

The crystallite size of sample was calculated by Scherrer's equation as showed in Eq. (3.3).

$$\Gamma = \frac{K\lambda}{\beta\cos\theta} \qquad (3.3)$$

where Γ = crystallite size, Å

K = shape factor (in case of cubic $SrTiO_3$, $K = 0.94$)

β = full width at half maximum (FHHM), radian

3.4.2 Compositional and elemental analysis

Thermo gravimetric/ differential thermal analysis (TG/DTA)

Thermal decomposition of as-synthesized MST materials was investigated with a Rigaku Thermo plus TG 8120 thermal analyzer operating from room temperature to 1000 $^{\circ}$C at a heating rate of 8 °C min^{-1} under a dry air flow of 50 mL min^{-1}. Approximately, 10 mg of sample was loaded into alumina pan and put on the microbalance. The microbalance sensitivity of the thermal analyzer is less than ±0.1 μg and its temperature precision is ±0.5 °C. The obtained data, including TG and DTA curves, can be used to explain the behavior of MST during thermal treatment.

Figure 3.3 Rigaku thermo plus TG 8120 thermal analyzer.

Inductively coupled plasma atomic emission spectrometer (ICP)

The elemental analyses of the samples (Sr: Ti ratio) were performed on a Shimadzu ICPE-9000 spectrometer. The Sr and Ti metal solutions (Wako) as internal standards were prepared by 5 concentrations for making the calibration curve. Approximately, 1 mg of synthesis sample was digested in 10 mL of 4M KOH at 80 °C, and then the resulting solution was diluted with deionized water in a 50-mL volumetric flask. The resulting solution was analysed and the obtained data were corrected with calibration curve.

Figure 3.4 Shimadzu ICPE-9000 spectrometer.

3.4.3 Textural properties

N_2 adsorption-desorption technique

Textural properties, including surface area, pore volume, pore diameter and pore-size distribution, of the synthesis materials were analyzed by N_2 adsorption-desorption measurement at -196 °C on a BEL Japan BELSORP-mini II instrument as shown in Figure 3.5. The sample was weighted around 600 mg, and then was measured exactly after pretreatment at 300 °C for 2 h under vacuum. The specific surface area (S_{BET}) was calculated based on the Brunauer–Emmett–Teller (BET) equation in the relative pressure (P/P_0) ranging from 0.05 to 0.1. The pore size distribution was calculated from the adsorption branch of physisorption isotherms using the Barrett–Joyner–Halenda (BJH) method.

In this study, textural properties of the synthesis materials were analyzed by nitrogen (N_2) adsorption-desorption measurement at -196 °C on a BEL Japan BELSORP-mini II instrument, shown in Figure 3.5. The sample was weighted around 600 mg and then was measured exactly after pretreatment at 300 °C for 2 h under vacuum. The specific surface area (S_{BET}) was calculated based on the Brunauer–Emmett–Teller (BET) equation in the relative pressure (P/P_0) ranging from 0.05 to 0.1. The pore size distribution was calculated from the adsorption branch of physisorption isotherms using the Barrett–Joyner–Halenda (BJH) method.

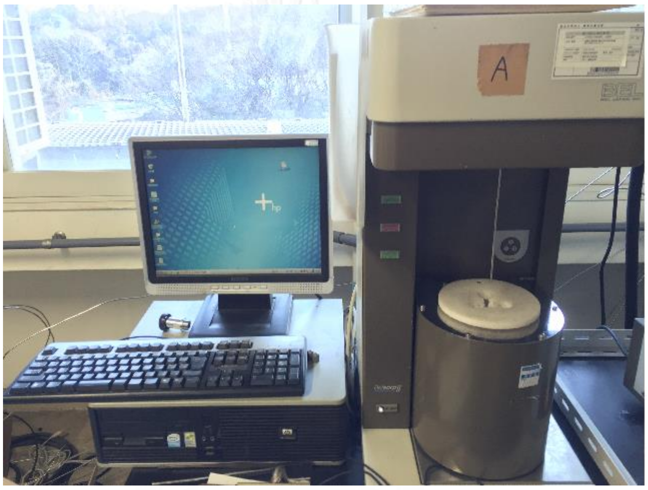

Figure 3.5 BEL Japan BELSORP-mini II instrument.

3.4.4 Morphology

Scanning transmission electron microscope (STEM)

In this study, STEM images were recorded on a Hitachi S-5200 electron microscope (Figure 3.6) operated at 30 kV and 20 µA. The samples (~1 mg) were suspended in ethanol, and then there were deposited on copper grids. The powder samples for the STEM observation were examined without any metal coating.

Figure 3.6 Hitachi S-5200 scanning electron microscope.

Transmission electron microscopy (TEM)

TEM images were record on a JEOL JEM-2010 transmission electron microscope, as shown in Figure 3.7, transmission electron microscope using an accelerating voltage of 200 kV. In this study, TEM specimen was prepared by dispersion of MST sample (~1 mg) in anhydrous ethanol under sonication. Then, the colloidal solution was dropped onto the copper grid, and then to insert copper grid into sample holder. The TEM images revealed the two dimensional morphology of MST sample, which reveal shape, size and mesopore arrangement. In addition, the pore size and pore size distribution of MST were analysed by using ImageJ software (version 1.49)

Figure 3.7 JEOL JEM-2010 transmission electron microscope.

3.4.5 Acidic and basic properties

Hammett indicator method

Acidic and basic strength of the catalysts were determined by using Hammett indicators. The indicators used included thymol blue, methyl yellow, methyl red, neutral red, bromothymol blue, phenolphthalein and 2,4-dinitroaniline. The indicators for acidic test were dissolved in benzene, while indicators were dissolved in anhydrous methanol. The catalyst (~10 mg) was suspended in test-tube containing 20 mL of benzene for acidic test and anhydrous methanol for basic test. Then, 5 drops of indicator solution were put into the test-tube and then it was shaken for 5 min. Finally, a color change was observed.

Table 3.2 Indicators used for the measurement of acid and basic strength [69]

Indicator	Color acid form	Color base form	pK_a
Thymol blue	red	yellow	2.8
Methyl yellow	red	yellow	3.3
Methyl red	red	yellow	4.8
Neutral red	red	yellow	6.8
Bromothymol blue	yellow	blue	7.2
Phenolphthalein	colorless	pink	9.8
2,4-dinitroaniline	yellow	red	15.0

Titration method

The measurement of total number of acidic and basic sites was performed according to the n-buthylamine and benzoic acid titration method, respectively [70]. The catalysts (~10 mg) were suspended in 10 mL of 5 wt% methyl red/benzene solution for acidic test and 5 wt% phenolphthalein/methanol solution for basic test. The mixtures were stirred at room temperature for 30 min, and then titrated with 0.01M n-buthylamine solution in benzene for acidic test and 0.01 M benzoic acid solution in methanol for basic test until a color change was observed.

The total acidity and basicity were calculated from Eq. (3.4);

$$N = \frac{0.01 \times V}{1000 \times W} \tag{3.4}$$

where N is total acidity or basicity (mmol g^{-1}), V is volume of titrant solution consumed in the titration (mL), and W is sample weight (mg).

3.4.6 Nature of active sites on MST surface

In situ Fourier-transform infrared spectroscopy (in-situ FTIR)

IR spectroscopy is one of powerful and useful techniques to investigate the nature (type, amount, and strength) of acid/base sites in solid catalysts. It can distinguish between Lewis and Brønsted site by using probe molecules such as, pyridine or ammonia for acid site and carbon dioxide or pyrrole for basic site. In addition, acid and base strength of solid catalysts can be determined from band of adsorbed probe molecules versus desorption temperature. Moreover, the number of active site can be determined by using integrated molar extinction coefficients [71].

In this work, pyridine was widely used as a probe molecule in IR study. It can simultaneously determine the existence of Lewis acid sites (LAS) and Brønsted acid site (BAS). The characteristic bands originated from the pyridine coordinated to LAS appear at around 1441-1445, 1491, 1575, and 1620 cm^{-1}, corresponding to C=C vibrations 19b, 19a, 8b and combination of 1+6a, while the characteristic bands of pyridine protonated by BAS (pyridinium cations) appear at 1635, and 1545 cm^{-1} [67, 71].

Pyrrole (PYH) was used as a probe molecule for determination of basicity on various metal oxides. Pyrrole adsorption on metal oxides can be an either non-dissociative or dissociative, the pyrrolate anion (PY^-) then being formed. Pyrrole has H-bond donor and H-acceptor properties. So, the species adsorbed formed may be surface-stabilized by basic site on the metal oxide surface. In case of pyrrole adsorption on basic site, the band at 3527 cm^{-1} as ν (N-H) of pyrrole in gaseous state [72] was disturb and shift to lower wavenumber. The ν (N-H) frequency shift is related to the basic strength of the basic sites as O^{2-} or OH^- group.

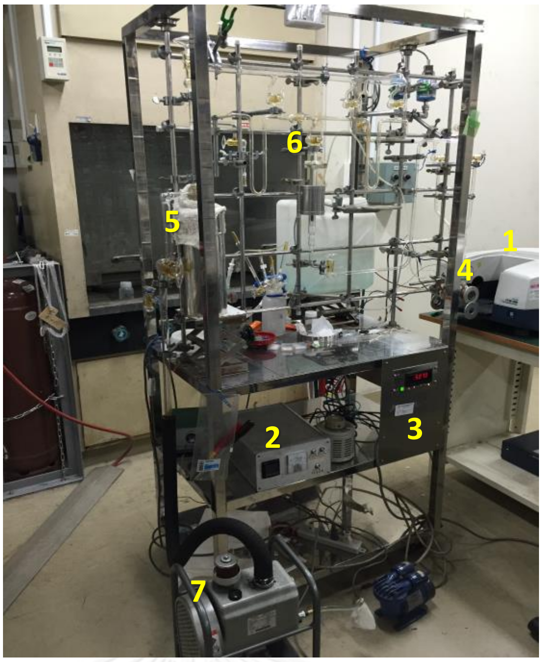

Figure 3.8 *In situ* FTIR set up: (1) JASCO FT/IR-6100 Fourier-transform infrared spectrometer; (2) temperature controller; (3) pressure transducer; (4) quartz-made IR cell; (5) liquid-nitrogen trap; (6) molecular probe reservoirs, and (7) rotary pump.

The high vacuum glass employs for the FTIR analysis and FTIR spectrometer are shown in Figure 3.8. About 40 mg of the sample (without KBr) was pressed into self-supporting disk with diameter of 20 mm at the pressure of 300 kg cm^{-2}. The obtained disk was mounted in a sample holder and then placed in a quartz-made IR cell. CaF_2 plates are used as the IR cell windows. The IR beam from the spectrometer is transmitted through the sample disk via the set of these windows. The FTIR spectra were obtained by using a JASCO FT/IR-6100 Fourier-transform infrared spectrometer equipped with a mercury cadmium telluride (MCT) detector as shown in Figure 3.8 (1). A total of 64 scans over 1000–4000 cm^{-1} at a resolution of 4 cm^{-1} were averaged for each spectrum. The background spectrum was recorded without any sample and measured spectrum was always automatically subtracted. The sample was pretreated for removing moisture and organic at 300 °C under evacuation for 1 h. Following this pretreatment, the sample was cooled to room temperature, and the spectrum of sample attained was recorded as reference spectrum.

Pyridine adsorption was carried out by equilibrating the pretreated sample with 100 Pa pressure of probe molecule vapor at 150 °C for 30 min. The sample was evacuated for 10 min at the same temperature, and the IR spectrum was collected. The study on pyrrole adsorption was performed under the same experimental conditions as the pyridine adsorption but the equilibrating the pretreated sample with pyrrole vapor and recording IR the spectrum were conducted at 30 °C.

The *in situ* FTIR of sample after desorption of probe molecules at various temperatures was used to study the acid and basic strength. In case of pyridine molecules were desorbed at 150 °C, 200 °C, and 250 °C, while pyrrole molecules were desorbed at 30 °C, 50 °C, 100 °C, and 150 °C.

Since, the obtained MSTs were applied as catalyst in transesterification. Therefore, the adsorption of methanol and triglyceride as reactant molecules on active sites of MST provided the information about transesterification mechanism of MST surface. The methanol adsorption was carried out by equilibrating the pretreated sample with 100 Pa pressure of methanol vapor at 30 °C for 30 min. The sample was evacuated for 10 min at the same temperature. Furthermore, the sample was heat stepwise to 65 °C, 120 °C, 150 °C and 170 °C and held for 30 min, and the IR spectrum was collected. In case of triglyceride, ethyl propionate was chosen as model ester molecule because triglyceride possessed large molecule and high boiling point. The ester adsorption was conducted similar procedure to methanol adsorption.

3.5 Transesterification procedure

3.5.1 Effect of catalyst type

The transesterification of PKO with methanol was carried out in a 100-mL PTFE-lined autoclave reactor equipped with a magnetic stirrer and temperature controller. In this study, two MST catalysts (MST-C-0 and MST-C-1) were used. Firstly, a calcined catalyst was mixed with 19.7 g of methanol in the reactor vessel at room temperature for 10 min, followed by adding 10 g of PKO. The reactor was then sealed and heated to 150 or 170 °C under vigorous stirring. The temperature was controlled by a silicone oil bath. After the reaction course (3 h), the reaction mixture was centrifuged to recover the solid catalyst. The excess methanol was removed by using the rotary evaporator at 60 °C and 100 mbar. Layer of FAME was washed by deionized water to remove glycerol, and then dried with anhydrous Na_2SO_4. Subsequently, the FAME product was subjected to sample preparation for composition analysis by gas chromatography (GC).

3.5.2 Effect of reaction condition

In this work, the reaction condition including molar ratio of methanol: PKO, catalyst loading, reaction temperature and reaction time were varied to find the suitable transesterification conditions. All of effects of reaction condition on FAME yield studied as procedure in Section 3.5.1. The molar ratio of methanol: PKO was varied as 5: 1, 10: 1 and 20: 1. The catalyst loading was used in different amount such as 1 wt%, 5 wt% and 10 wt% based on amount PKO. The reaction temperature and reaction time for transesterification were studied at 120 °C, 150 °C and 170°C for 1 h, 2 h and 3 h, respectively.

3.5.3 Effect of FFA and H_2O addition on catalytic activity

Free fatty acid (FFA) and water containing in the oil feedstock are usually defined as poisons for alkaline catalysts used in conventional biodiesel production [73, 74]. A similar detrimental effect was also observed in the transesterification over solid base catalysts. In this work, oleic acid, as a model FFA, and water were added into PKO at different amounts (1 wt%, 5 wt%, and 10 wt% based on the amount of PKO). The reaction was conducted as procedure in Section 3.5.1.

3.6 Catalyst reusability of MST

In order to study reusability, the MST catalyst used in the first run was separated from the reaction mixture by centrifugation, followed by washing with methanol. The washed catalyst was dried at 100 °C overnight, and then calcined at

350 °C for 4 h before being used in the next run. The transesterification was carried out under suitable conditions for each MST catalyst.

3.7 Kinetic and thermodynamic study

In this work, transesterification of PKO with methanol was assumed to follow pseudo-first order kinetics because methanol in reactions is employed in excess to the required stoichiometric amount [69]. The reaction was performed at 3 temperature levels (120 °C, 150 °C, and 170°C) and kinetic data were collected every 30 min until 2 h. The reaction rate constant was calculated by following pseudo-first order Eq. (3.5).

$$-\ln(1-X) = kt \tag{3.5}$$

where k = the first order rate constant (h^{-1})

X = FAME yield (mol%).

t = reaction time (h)

The Arrhenius equation was employed to estimate the activation energy (E_a) and pre-exponential factor (A) following Eq. (3.6) [69].

$$\ln k = \ln A - E_a/RT \tag{3.6}$$

where E_a = activation energy (kJ mol^{-1})

A = pre-exponential factor (h^{-1})

R = gas constant (8.314×10^{-3} kJ K^{-1} mol^{-1})

T = reaction temperature (K).

3.8 Reaction product analysis

The FAME composition of product was analyzed with a Shimadzu 14A gas chromatograph equipped with a 30-m DB-Wax capillary column and a flame ionization detector (FID) as shown in Figure 3.9. The quantity of FAME produced was determined in accordance with the standard method EN 14103 using methyl heptadecanoate as the reference standard. The FAME yield was defined in Eq. (3.7).

$$\text{FAME yield (wt\%)} = \frac{\text{Weight of FAME attained by GC}}{\text{Theoretical weight of FAME}} \times 100 \qquad (3.7)$$

The example chromatogram of product attained is shown in APPENDIX B. The GC conditions for determination of FAME composition are summarized in Table 3.3.

Figure 3.9 Shimadzu 14A gas chromatograph.

Table 3.3 GC conditions for determination of FAME composition

Conditions	Value
Carrier gas (He) flow rate	100 kPa
Make up gas (HE) pressure	20 kPa
Hydrogen pressure (for FID)	50 kPa
Air pressure (for FID)	30 kPa
Detector temperature	250 °C
Spilt ratio	1: 20
Injection port temperature	250 °C
Inject volume	0.1 μl
Initial column temperature	120 °C
Ramp rate	10 °C /min
Final column temperature	230 °C

CHAPTER IV

Development of mesostructured Sr and Ti mixed oxides

In this Chapter, the development of mesostructured Sr and Ti mixed oxides (MST) was focused. These materials were prepared via a self-assembly sol-gel combustion method using a commercial non-ionic triblock copolymer (Pluronic P123) as a structure-directing agent. The effect of adding citric acid as a metal-ion complexing agent and fuel in the combustion step on the formation of crystalline $SrTiO_3$ with enhanced surface area and mesoporosity was investigated. Moreover, the effects of synthesis parameters, such as molar ratio of citric acid: total metals, amount of structure-directing agent and calcination temperature, on the physicochemical properties of MSTs obtained were investigated.

4.1 Effect of citric acid addition

Thermal decomposition profiles of MSTs synthesized without (MST-0C-0.17P(as-syn)) and with citric acid addition using different molar ratios of citric acid: total metals (MST-0.5C-0.17P(as-syn), MST-1C-0.17P(as-syn), and MST-2C-0.17P(as-syn)) are shown in Figure 4.1. Weight loss of MST-0C-0.17P(600) occurred in two stages. The first weight loss (22.89 wt%) with endothermic peak in the range of 200–250 °C was ascribed to a loss of water from $Sr(NO_3)_2$. The endothermic peak at 298 °C was attributed to the decomposition of templating agent [75]. The next weight loss (14.65 wt%) with multi-step exothermic changes between 480 °C and 650 °C was divided into 2 steps for interpreting thermal decomposition. Firstly, the exothermic change at 497 °C was attributed to the formation of crystalline phases such as $SrCl_2$, $SrCl_2{\cdot}H_2O$, and $SrTiO_3$. Then, an exothermic change observed above 600 °C was probably due to impurity phase decomposition concomitant with $SrTiO_3$ crystallization.

MSTs synthesized with citric acid addition exhibited three-stage weight loss. The first weight loss with exothermic change between 200 and 220 °C corresponded to auto-combustion of metal citrate complexes [17, 76]. The amount of weight loss in this region increased with increasing amount of citric acid addition. The subsequent exothermic weight loss between 300 and 350 °C was derived from the decomposition of the polymeric template [75]. The endothermic peak at 515 °C and 461 °C for MST-0.5C-0.17P(as-syn) and MST-1C-0.17P(as-syn), respectively, corresponded to the decomposition of carbon residue on metal oxides. Possibly, the combustion of citrate complexes generated heat and oxygen-deficient atmosphere, leading to carbonization of the triblock copolymer template to form in situ carbon residue as amorphous metal oxides-carbon composite [57]. Lastly, the weight loss with exothermic change that appeared above 500 °C was mainly due to the crystallization of $SrTiO_3$ via solid state reaction, as evidenced by the XRD result of MST-1C-0.17P(500) as shown in Figure 4.10. However, MST-0.5C-0.17P(600) had endothermic change between 580 and 650 °C was ascribed to decomposition of $SrCl_2$, $SrCl_2{\cdot}H_2O$ and $SrCl_2{\cdot}6H_2O$ phases. The presence of impurity phases in MST-0.5C-0.17P(600) was confirmed by the XRD result of MST-0C-0.17P(600) as shown in Figure 4.2.

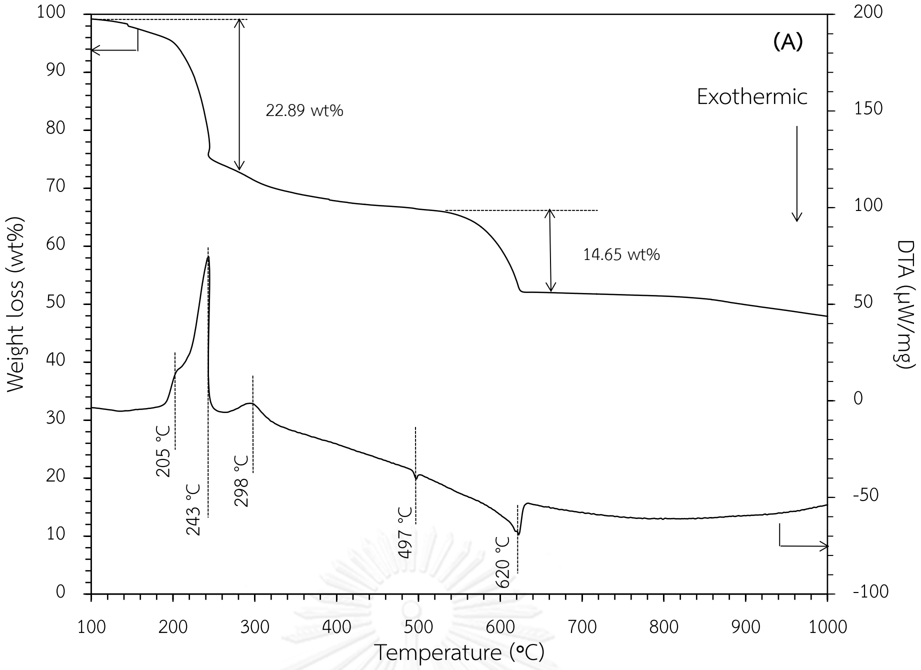

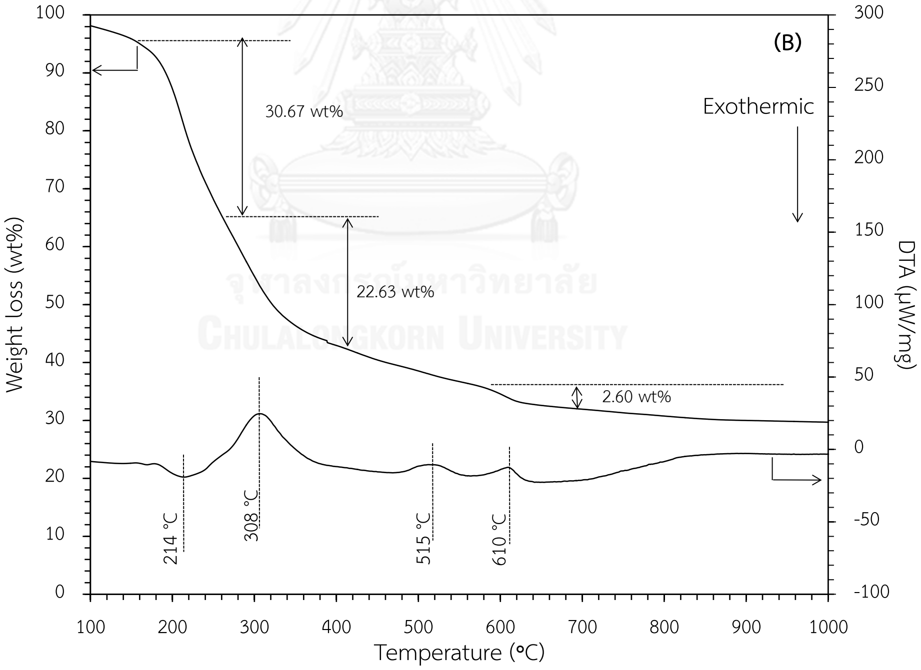

Figure 4.1 Weight loss and DTA curves of as-synthesized (A) MST-0C-0.17P(as-syn), (B) MST-0.5C-0.17P(as-syn), (C) MST-1C-0.17P(as-syn), and (D) MST-2C-0.17P(as-syn).

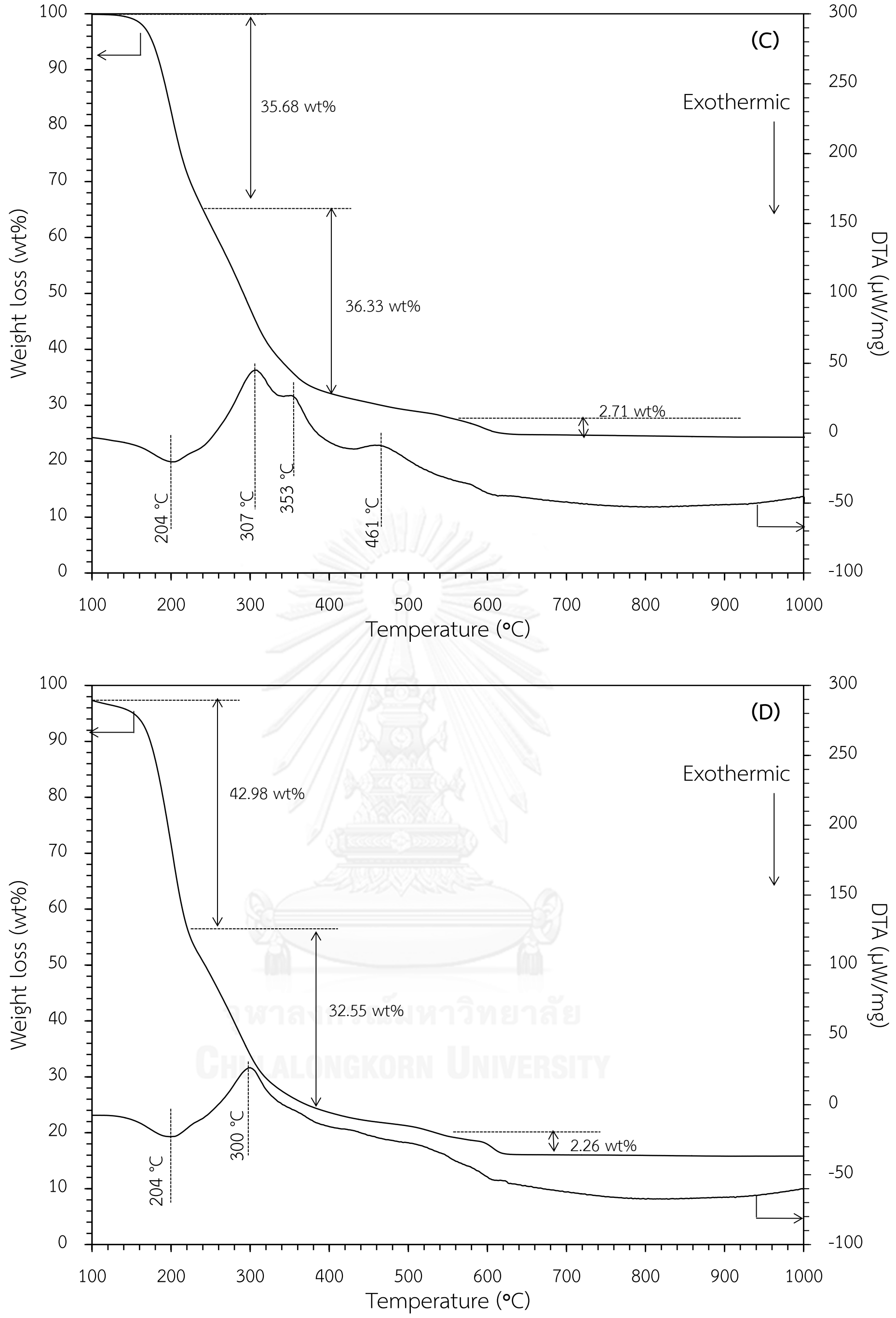

Figure 4.1 (cont.) Weight loss and DTA curves of as-synthesized (A) MST-0C-0.17P(as-syn), (B) MST-0.5C-0.17P(as-syn), (C) MST-1C-0.17P(as-syn), and (D) MST-2C-0.17P(as-syn).

The XRD patterns of MSTs synthesized with different molar ratios of citric acid: total metals are shown in Figure 4.6. The major diffraction peaks were indexed to cubic-perovskite $SrTiO_3$ phase (JCPDS file: 00-035-0734). The XRD patterns of MST-0C-0.17P(600) and MST-0.5C-0.17P(600) exhibited the impurity phases including, $SrCO_3$, $SrCl_2$, $SrCl_2•H_2O$ and $SrCl_2•6H_2O$. It can be explained by reactivity of Sr^{2+} that easily formed salts with several anions in the synthesis mixture [77]. With increasing the amount of citric acid in the synthesis mixture, the impurity phases were not detected and diffraction pattern of $SrTiO_3$ exhibited higher intensity. The results can be explained that citric acid acted as complexing agent, which reduced the amount of isolated Sr^{2+} and retarded the salt formation. The XRD result indicated that the MST-1C-0.17P(as-syn) was amorphous in nature and free of detectable salts as shown in Figure A1. Moreover, elemental analysis using an inductively coupled plasma technique indicated that the Sr: Ti molar ratio of MST-1C-0.17P(600) was 1.09: 1, which was closer to the theoretical ratio (Sr: Ti = 1: 1) than that of MST-0C-0.17P(600) (Sr: Ti = 1.34: 1). In addition, citric acid acted as fuel to promote auto-combustion reaction that generated exothermic heat and induced the crystallization of $SrTiO_3$ during thermal treatment. Therefore, the increasing of citric acid improved both the purity and crystallinity of MSTs. However, the XRD pattern of (MST-2C-0.17P(600)) exhibited a lower intensity than that of MST-1C-0.17P(600) and $SrCO_3$ as impurity phase was detected. The presence of $SrCO_3$ resulted from chemisorption of CO_2, generated from decomposition of citric acid, onto the Sr^{2+}. Moreover, previous work reported that an excess amount of citric acid retarded the crystallization of $SrTiO_3$ [78].

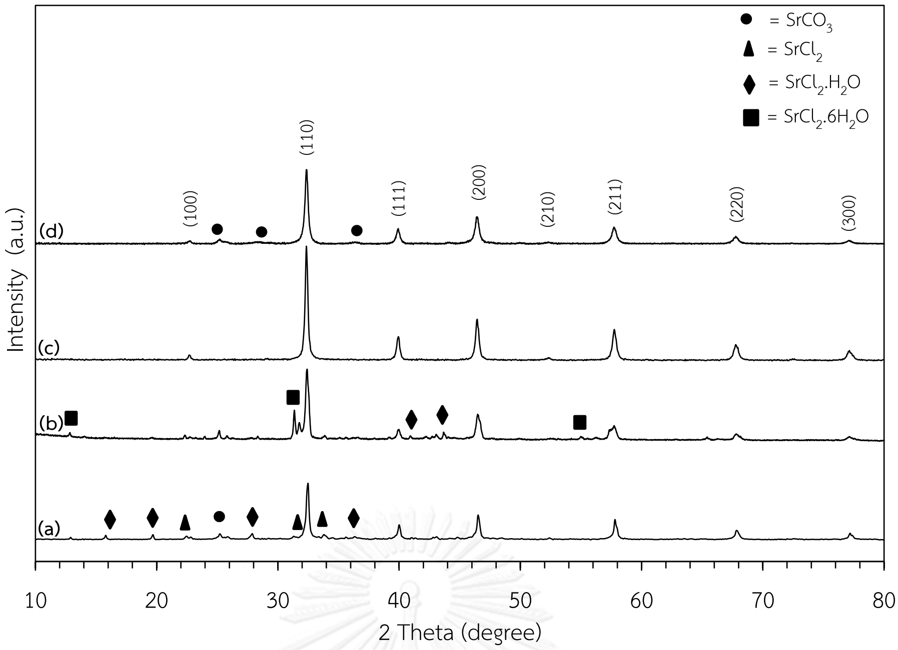

Figure 4.2 XRD patterns of calcined (a) MST-0C-0.17P(600), (b) MST-0.5C-0.17P(600), (c) MST-1C-0.17P(600), and (d) MST-2C-0.17P(600). Miller indexes indicate $SrTiO_3$ with perovskite structure.

The N_2 adsorption–desorption isotherms of MSTs materials prepared with different molar ratio of citric acid: total metals are shown in Figure 4.3. Isotherm of MST-0C-0.17P(600) showed a type II isotherm according to the IUPAC classification with a type H3 hysteresis loop, indicating aggregation of nonporous materials [79]. MST-0.5C-0.17P(600) and MST-1C-0.17P(600) exhibited a type IV isotherm according to the IUPAC classification, which is characteristic of mesoporous materials. The presence of a type H1 hysteresis loop indicated its cylindrical mesopores. The isotherm of MST-2C-0.17P(600) was also classified as a type IV with the hysteresis loops at the relative pressure (P/P_0) ranging from 0.5-0.7, which is the characteristics of small mesopore. The BJH plots (inset) of all MSTs revealed mesopores with ca. 2-nm diameter, probably related to a transformation of amorphous oxides to crystalline phase during calcination. An increase in density of material upon the crystallization can create free spaces between crystals as new porosity [56]. MST-0.5C-0.17P(600) exhibited bimodal pore size distribution, while the BJH plot of MST-1C-0.17P(600) showed tri-modal pore size distribution. The mesopores with diameters larger than ca. 20-nm might be generated in association with the mixed oxide nanoparticles that aggregate around the molecular self-assembly of triblock copolymer as the template. It is noteworthy that the size of large mesopores is similar to that of Pluronic P123 micelle formed under acid conditions [80]. On the contrary, the BJH plot of MST-2C-0.17P(600) revealed only pore sizes with ca. 2-5 nm diameter were observed. It should be collapse of mesopore.

Textural properties of MST materials synthesized with different molar ratios of citric acid: total metals are shown in Table 4.1. It can be seen that the BET surface area, pore diameter, and total pore volume of MSTs increased with increasing citric acid: total metals, which resulted from the generation of mesopores. Therefore, the addition of citric acid should be promoted the formation of mesoporous character, which enhanced the textural properties of the materials attained. However, the BET surface area, average pore size diameter and total pore volume of MST-2C-0.17P(600) possessed lower than those of other samples. The results suggested that a large amount of citric acid added released an excessive heat during calcination, which induced sintering of $SrTiO_3$ [81].

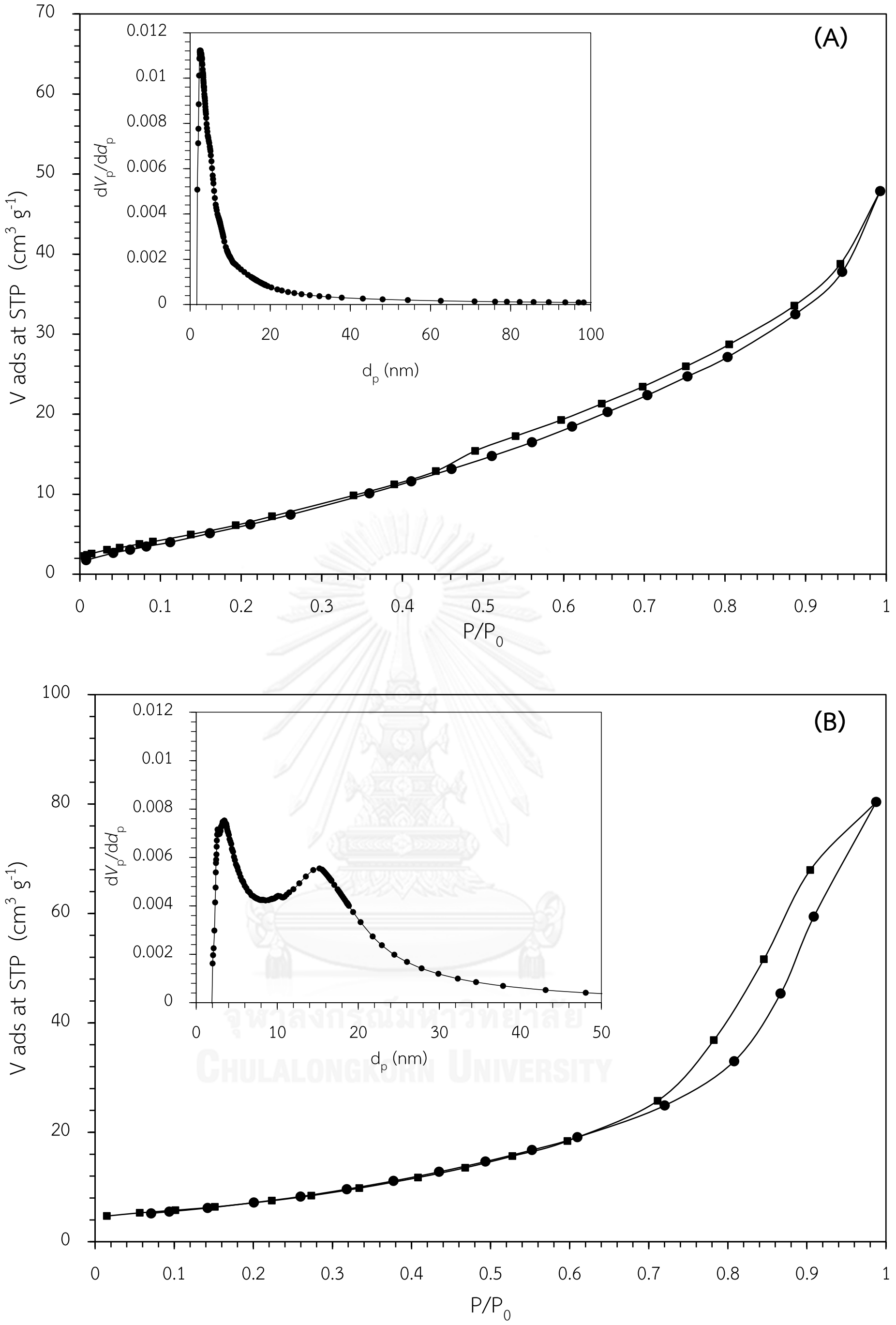

Figure 4.3 N_2 adsorption-desorption isotherms of (A) MST-0C-0.17P(600), (B) MST-0.5C-0.17P(600), (C) MST-1C-0.17P(600), and (D) MST-2C-0.17P(600). (Symbol: ● = adsorption branch and ■ = desorption branch). The insets show BJH pore size distribution.

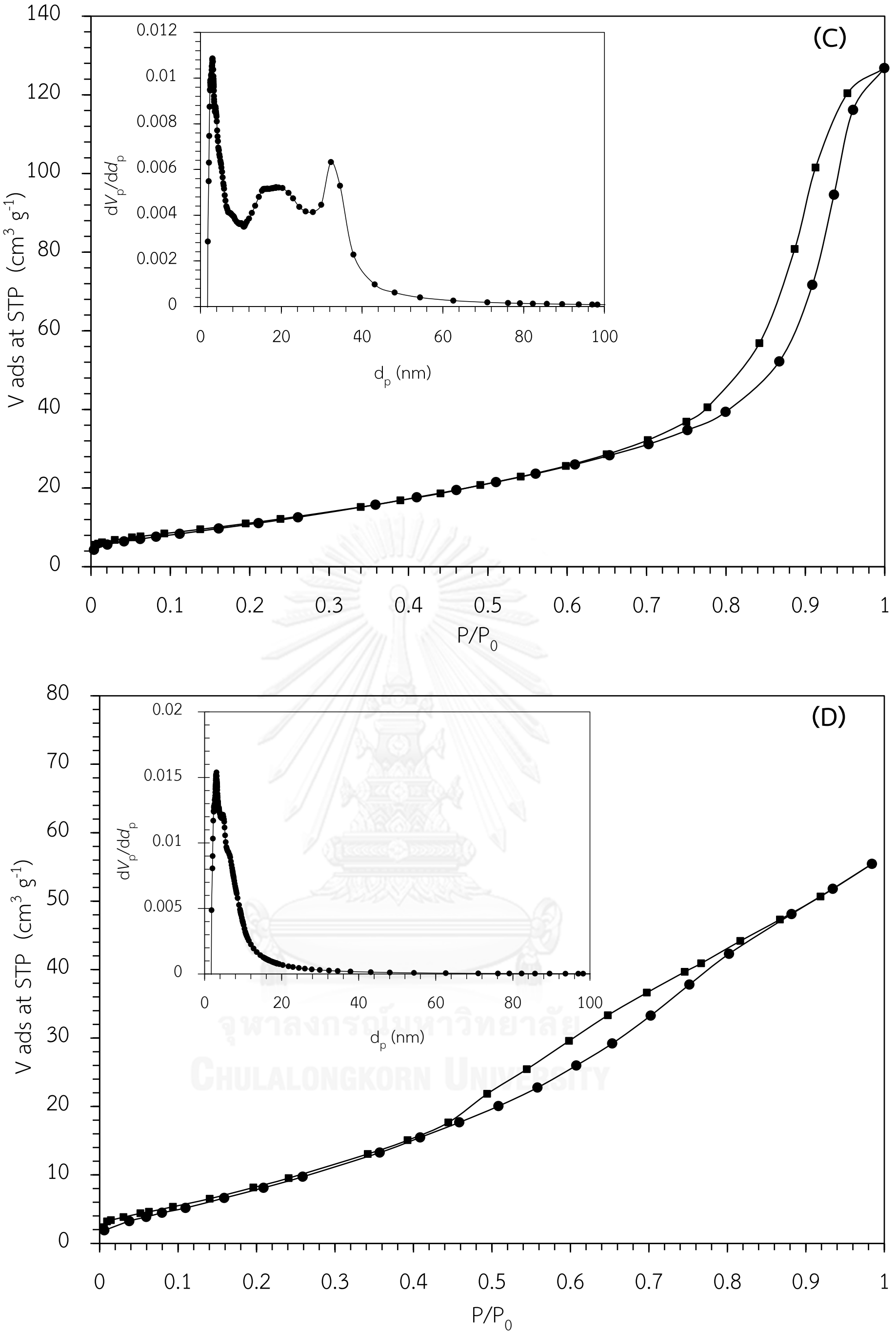

Figure 4.3 (cont.) N_2 adsorption-desorption isotherms of (A) MST-0C-0.17P(600), (B) MST-0.5C-0.17P(600), (C) MST-1C-0.17P(600), and (D) MST-2C-0.17P(600). (Symbol: ● = adsorption branch and ■ = desorption branch). The insets show BJH pore size distribution.

Table 4.1 Textural properties of MSTs synthesized with different molar ratios of citric acid: total metals

Sample	S_{BET} (m^2 g^{-1})	D_p (nm)	V_p (cm^3 g^{-1})
MST-0C-0.17P(600)	20.3	11.2	0.08
MST-0.5C-0.17P(600)	27.0	18.4	0.13
MST-1C-0.17P(600)	41.5	18.5	0.20
MST-2C-0.17P(600)	16.9	9.3	0.09

The morphologies of MSTs synthesized with different amount of citric acid are shown in Figure 4.4. The MST-0C-0.17(600) particles exhibited cubic shape typically to the cubic perovskite $SrTiO_3$ [14]. It is suggested that the inorganic species could not sufficiently assemble around the template micelle, because they possessed high reactivity toward hydrolysis and condensation to chelate or to form with other anions in the synthesis solution [82, 83]. In addition, the commercial block copolymer molecules failed to template ordered mesoporous mixed oxides because of their small contrast in the hydrophilicity/hydrophobicity of head and tail groups [43]. The STEM micrograph of MST-0.5C-0.17(600) revealed the cubic particles connected together through their edges and corners. The MST-1C-0.17(600) exhibited distinctly globular particle agglomerates (average size = 300 nm) in which the $SrTiO_3$ crystals also shared edges and corners. Their distorted shape was due to the rigid crystalline $SrTiO_3$ structure. No separate cubic crystals were observed. Moreover, MST-1C-0.17(600) possessed open mesopores with average diameters of 20 and 32 nm on the agglomerate surface. In case of MST-2C-0.17(600), the $SrTiO_3$ crystals aggregated to bigger particles with reduced porosity. It can be explained that a massive heat released from the combustion of citric acid [81] induced sintering and agglomeration of crystals.

TEM images of MST-0C-0.17(600) and MST-1C-0.17(600) are presented in Figure 4.5 (A) and (B), respectively. MST-0C-0.17(600) showed an aggregation of cubic crystals, whereas MST-1C-0.17(600) revealed accessible mesopores with similar sizes, which dispersed throughout the crystal agglomerates. These results were consistent with the BJH plot in Figure 4.3 (C).

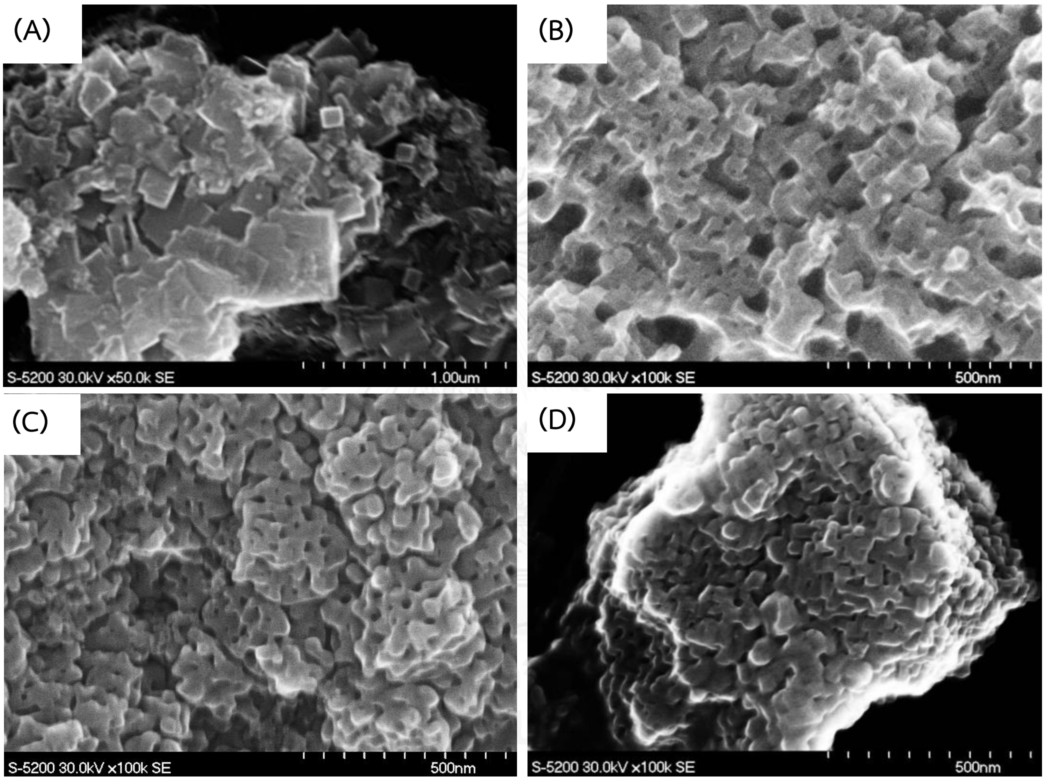

Figure 4.4 STEM micrographs of (A) MST-0C-0.17P(600) at magnification of 50000×, (B) MST-0.5C-0.17P(600), (C) MST-1C-0.17P(600), and (D) MST-2C-0.17P(600) at magnification of 100000×.

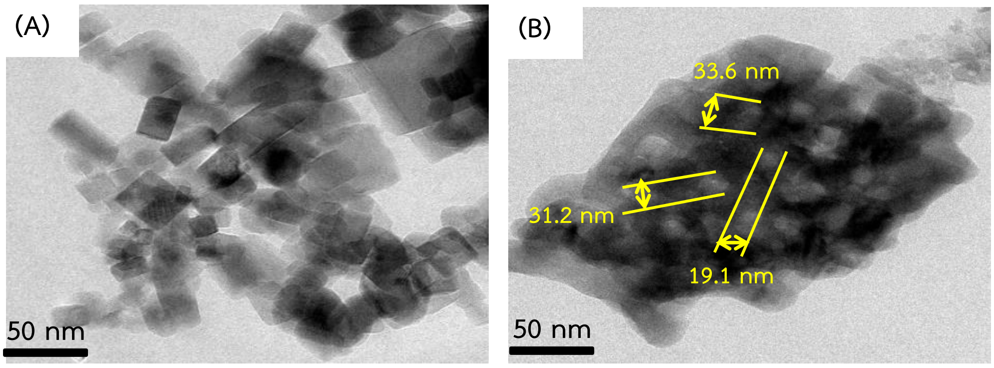

Figure 4.5 TEM micrographs of (A) MST-0C-0.17P(600), and (B) MST-1C-0.17P(600) at magnification of 50000×.

4.2 Effect of amount of structure-directing agent

Figure 4.6 (A) and (B) show TG/DTA curves of MST synthesized by without structure-directing agent (MST-1C-0P(as-syn)) and with addition of structure-directing agent (MST-1C-0.34P(600)), respectively. Both MSTs showed three-stage weight loss. MST-1C-0P(600) showed major weight loss (54.51 wt%) between 180 and 350 °C. In this range, both endothermic and exothermic changes were observed. The exothermic peak was detected at 195 °C, indicating auto-combustion of metal citrate complexes. The endothermic peak centered at 280°C should be due to dehydroxylation of metal species [15]. The third weight loss (14.30 wt%) with endothermic peak centered at 535 °C should be attributed to decomposition of impurity phases. It can be seen that the thermal decomposition profile of MST-1C-0P(600) was different from that of MST synthesized with Pluronic P123 addition. In case of MST-1C-0.34P(600), its TG/DTA curve was similar to that of MST-1C-0.17P(600) as shown in Figure 4.1 (C). The first weight loss (31.82 wt%) with exothermic peak centered at 202 °C was ascribed to the auto-combustion of metal citrate complexes. Then, the major weight loss (44.08 wt%) with endothermic change between 300 and 360 °C was derived from the decomposition of polymeric templating molecules. Interestingly, the amount of weight loss in this range increased with increasing the amount of Pluronic P123, which confirmed that the weight loss between 300 and 350 °C was derived from decomposition of Pluronic P123. The last step weight loss (1.2 wt%) was due to the crystallization of $SrTiO_3$ via solid state reaction.

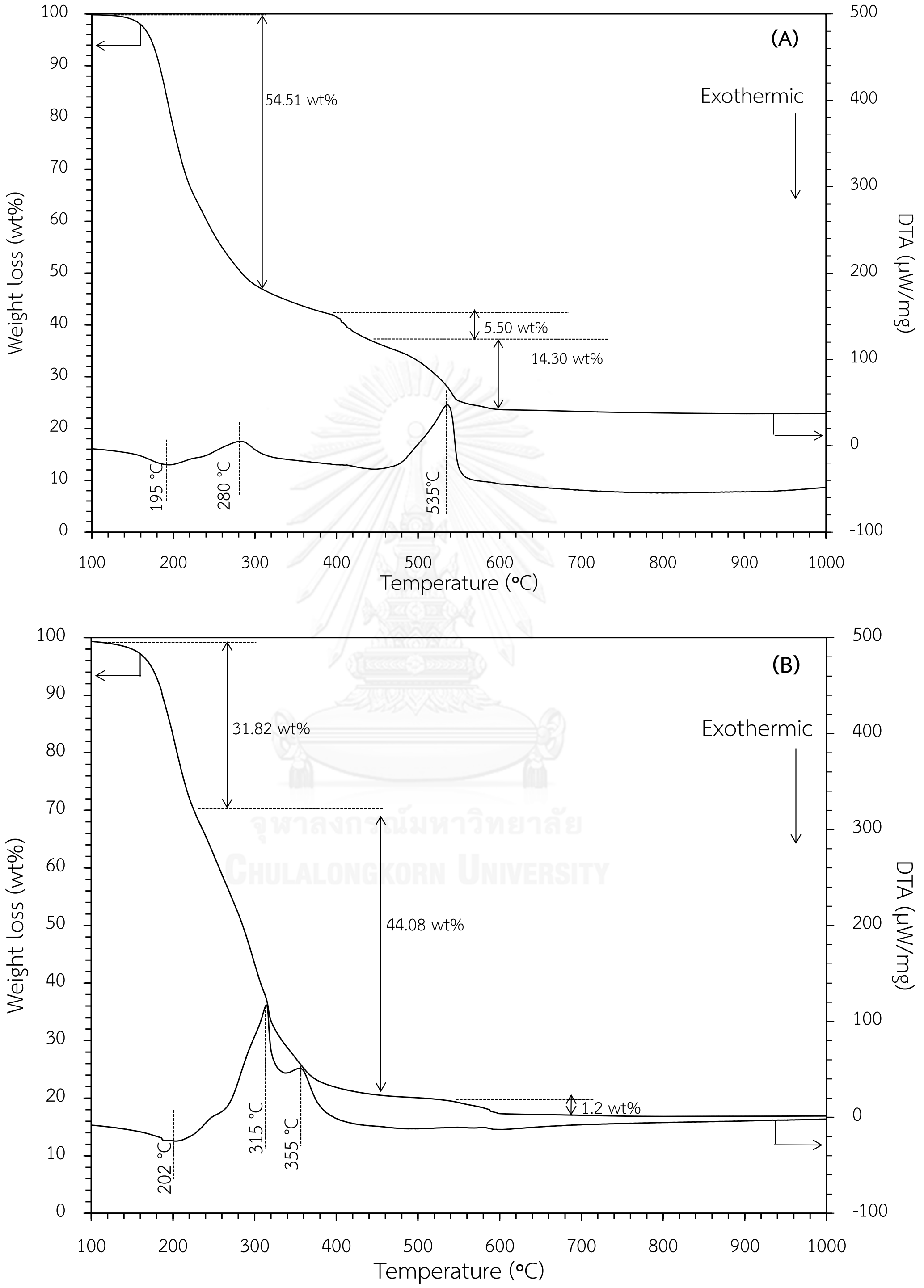

Figure 4.6 Weight loss and DTA curves of as-synthesized (A) MST-1C-0P(as-syn) and (B) MST-1C-0.34P(as-syn).

The XRD patterns of calcined MSTs prepared with different amount of structure-directing agent are shown in Figure 4.7. The diffraction patterns indicated a pure phase of $SrTiO_3$ with the perovskite structure. The XRD patterns of MST-1C-0P(600) and MST-1C-0.17P(600) had sharp and intense peaks, indicating that they possessed large crystals and high crystallinity. On the other hand, MST-1C-0.34P(600) possessed lower crystallinity. The increasing of structure-directing agent loading increased the groups of micelle, which might affect the wall thickness and crystallite size of $SrTiO_3$. This reason was confirmed by the STEM technique as shown in Figure 4.9.

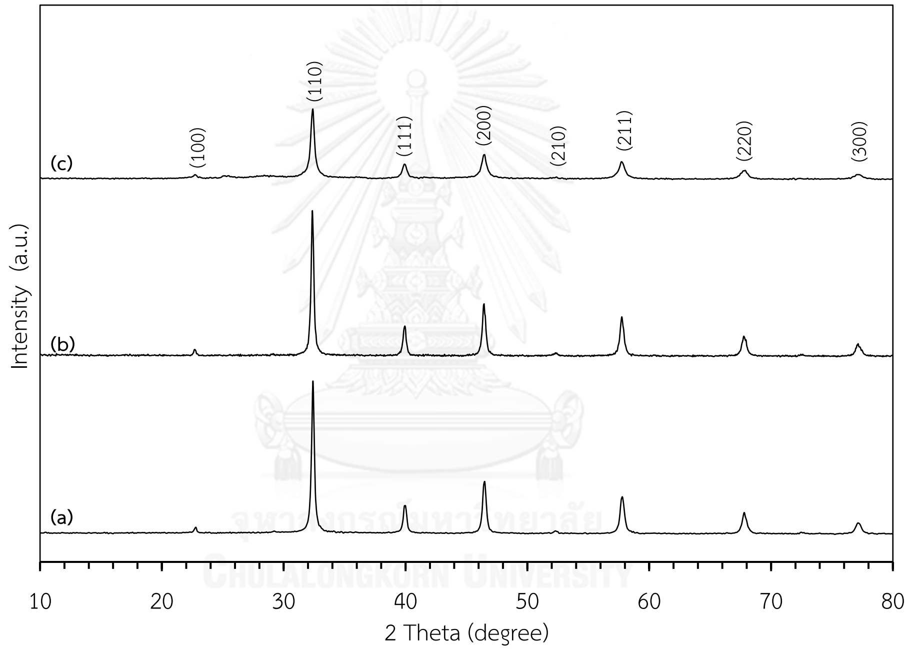

Figure 4.7 XRD patterns of calcined (a) MST-1C-0P(600), (b) MST-1C-0.17P(600), and (c) MST-1C-0.34P(600). Miller indexes indicate $SrTiO_3$ with perovskite structure.

The N_2 adsorption-desorption isotherms and BJH pore size distribution of MST-1C-0P(600) and MST-1C-0.34P(600) are shown in Figure 4.8. The textural properties of these materials are summarized in Table 4.2. Both MSTs exhibited a type IV isotherm according to the IUPAC classification, which is characteristic of mesoporous materials. The BJH plot of MST-1C-0P(600) indicated bimodal pore sizes. The 2-nm pore should be related to free space generated from amorphous to crystalline transformation [84], while the mesopore with diameter of ca. 15-nm should be interparticle void of nanoparticle aggregates. On the contrary, MST-1C-0.34P(600) possessed peak at around 3-5 nm in which MST-1C-0.34P(600) had only mesopores from amorphous to crystalline transformation. The BET surface area of materials attained increased with increase amount of Pluronic P123 added in the synthesis mixture. The results should be attributed to the generation of mesopore formed by $SrTiO_3$ assembled around the template micelles. However, MST-1C-0.17P(600) possessed lager pore diameter than MST-1C-0.34P(600). It was revealed that the amount of structure-directing agent affected size and arrangement of template self-assembly, which determined morphology and porous structure of the resulting materials.

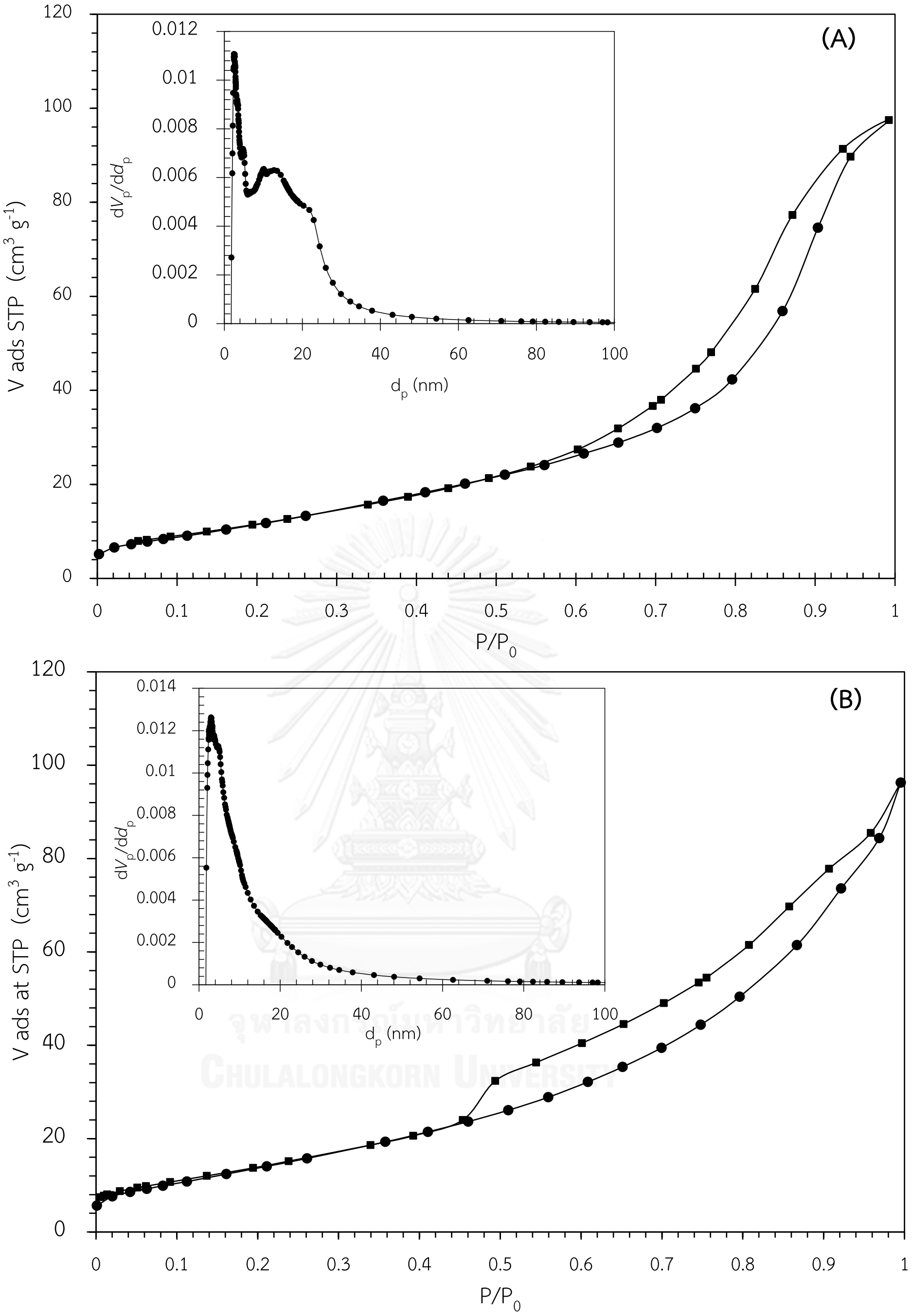

Figure 4.8 N_2 adsorption-desorption isotherms of (A) MST-1C-0P(600) and (B) MST-1C-0.34P(600). (Symbol: ● = adsorption branch and ■ = desorption branch). The insets show BJH pore size distribution.

Table 4.2 Textural properties of MST synthesized with different amount of structure-directing agent

Sample	**S_{BET} (m^2 g^{-1})**	**D_p (nm)**	**V_p (cm^3 g^{-1})**
MST-1C-0P(600)	23.3	13.9	0.11
MST-1C-0.17P(600)	41.5	18.4	0.20
MST-1C-0.34P(600)	51.9	10.9	0.15

Figure 4.9 illustrates STEM micrographs of MST-1C-0P(600), MST-1C-0.17P(600) and MST-1C-0.34P(600). MST-1C-0P(600) showed cubic shape crystals, likely to perovskite $SrTiO_3$ [14]. The cylindrical mesopores generated from particles assembled around template molecules were not observed for MST-1C-0P(600). Hence, this result indicated that the presence of both citric acid and structure-directing agent is necessary for the formation of mesostructure $SrTiO_3$. Comparing with MST-1C-0.17P(600), MST-1C-0.34P(600) exhibited higher porosity but had smaller pore diameter than MST-1C-0.17P(600). The results should be explained by an increase in a number of template micelles due to increased loading of Pluronic P123. Thus, a number of pores per unit area of MST-1C-0.34P(600) was higher than that of MST-1C-0.17P(600). However, MST-1C-0.17P(600) and MST-1C-0.34P(600) had the same amount of inorganic species, so the pore wall of MST-1C-0.17P(600) might be thicker than MST-1C-0.34P(600). These results were in agreement with the XRD (Figure 4.7), which MST-1C-0.17P(600) had more intense and shaper pattern, so higher crystallinity than MST-1C-0.34P(600). Therefore, the addition of Pluronic P123 at 0.17 moles was the suitable amount for preparing MST with a high crystallinity and good textural properties.

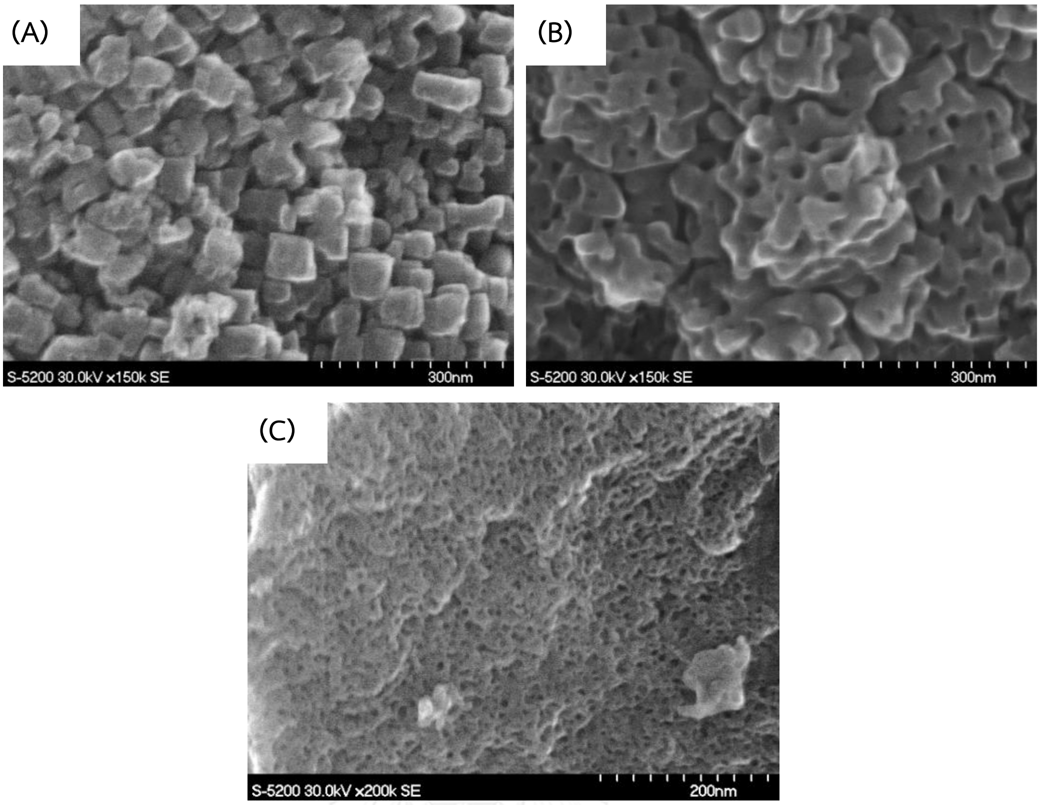

Figure 4.9 STEM micrographs of (A) MST-1C-0P(600) and (B) MST-1C-0.17P(600) at magnification of 150000×, and (C) MST-1C-0.34P(600) at magnification of 200000×.

4.3 Effect of calcination temperature

The XRD patterns of MSTs calcined at different temperatures (MST-1C-0.17P(500), MST-1C-0.17P(600), MST-1C-0.17P(700), and MST-1C-0.17P(800)) are shown in Figure 4.10. The XRD patterns of all samples exhibited cubic perovskite $SrTiO_3$ without any impurity phases. Furthermore, the intensity of diffraction peaks increased with increasing the calcination temperature. This was probably due to a sintering effect, which promoted the crystal growth of $SrTiO_3$ phase.

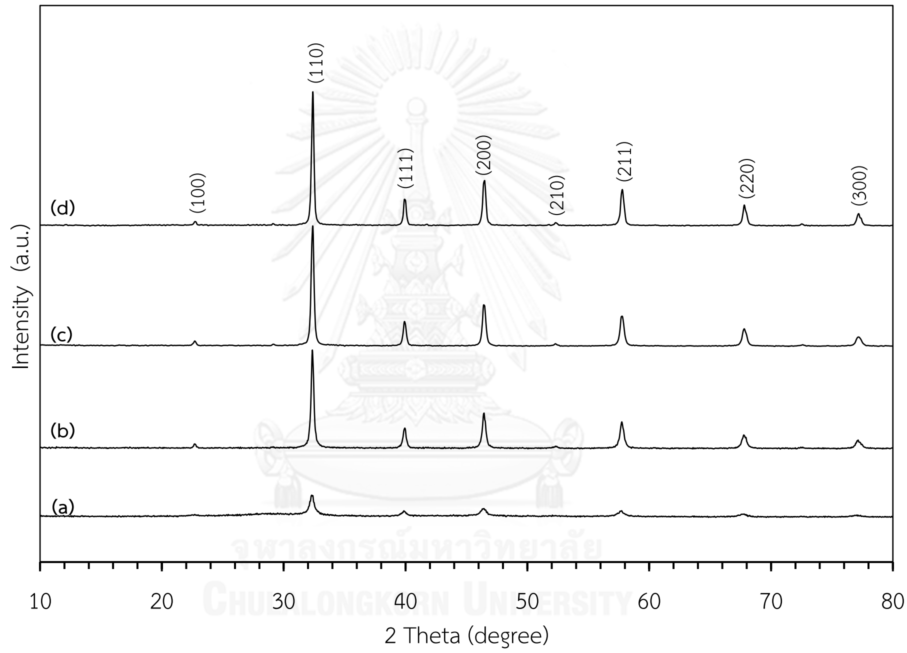

Figure 4.10 XRD patterns of calcined (a) MST-1C-0.17P(500), (b) MST-1C-0.17P(600), (c) MST-1C-0.17P(700), and (d) MST-1C-0.17P(800). Miller indexes indicate $SrTiO_3$ with perovskite structure.

The N_2 adsorption-desorption isotherms and BJH pore size distribution of MST-1C-0.17P(500), MST-1C-0.17P(600), MST-1C-0.17P(700), and MST-1C-0.17P(800) are shown in Figure 4.11. The textural properties of these materials are summarized in Table 4.3. All MST samples exhibited the type IV isotherms in accordance with the IUPAC classification. However, the hysteresis loop of each MST had different shapes. The hysteresis loop of MST-1C-0.17P(500) was classified to be type H2 appearing at a relative pressure (P/P_0) range of 0.45–0.90, which is characteristic of mesoporous materials with narrow necks and wider bodies (ink-bottle pores) [85]. In case of MST-1C-0.17P(700) and MST-1C-0.17P(800), the hysteresis loops for filling and emptying of mesopores were shifted to higher P/P_0 ranges (0.8–0.9), which were associated with the presence of large diameter pores [86]. The pore size distribution of MST-1C-0.17P(500) was broad between 2 and 15 nm. The result showed that MST-1C-0.17P(500) was semi-crystalline material. On the other hand, the BJH plots of MST-1C-0.17P(700) and MST-1C-0.17P(800) were bimodal pore size distribution. The first peak at ca. 2-nm was derived from the free space between crystal due to transformation of amorphous oxides to crystalline phase [84]. Other pores with lager diameters were probably formed by a sintering effect, resulting in fusion of $SrTiO_3$ crystals at high temperatures. The BET surface area of the materials attained decreased with increasing the calcination temperature (Table 4.3). The high temperature, at which the MST samples were calcined, should induce the crystal growth and morphological change of resulting materials.

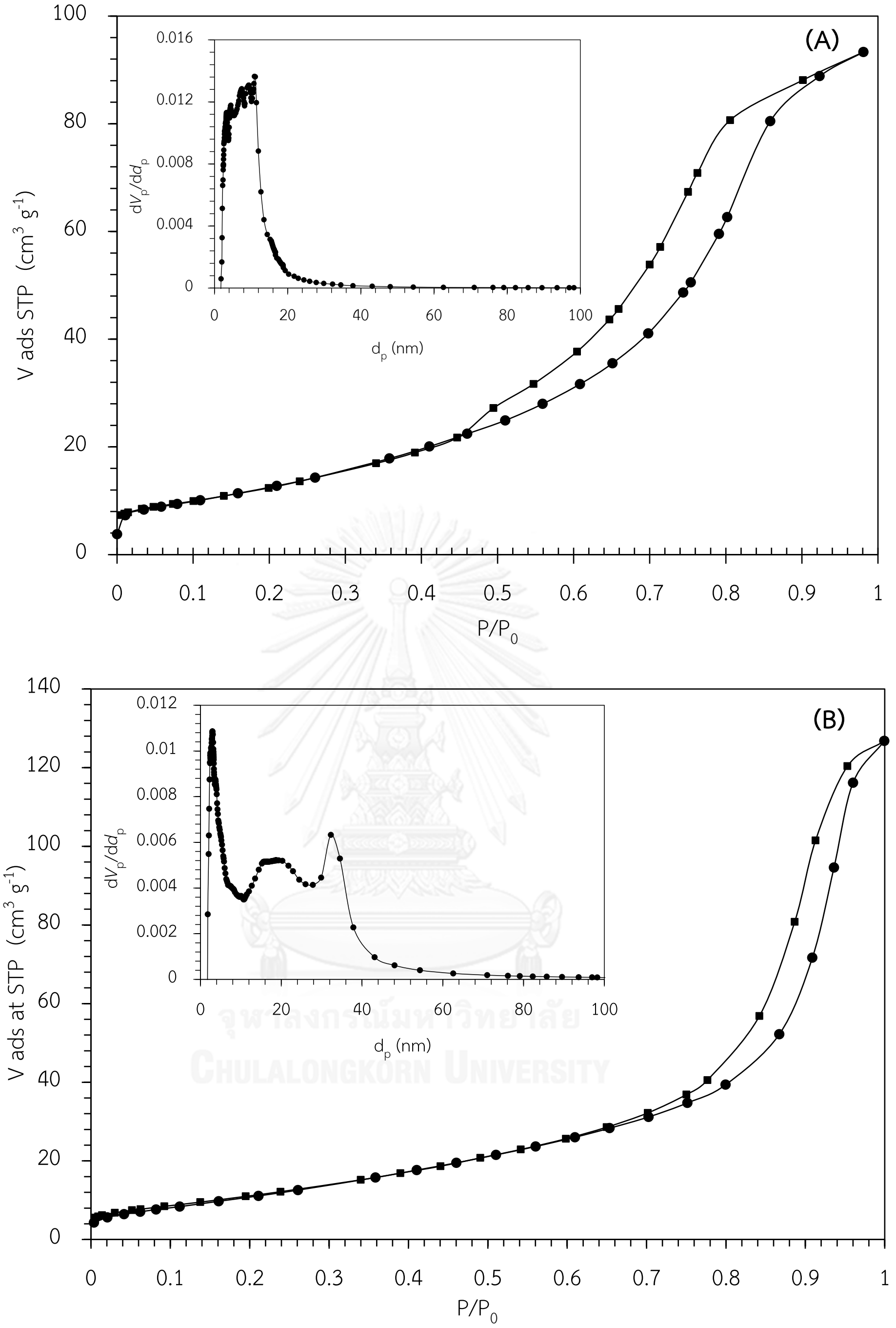

Figure 4.11 N_2 adsorption-desorption isotherms of (A) MST-1C-0.17P(500), (B) MST-1C-0.17P(600), (C) MST-1C-0.17P(700), and (C) MST-1C-0.17P(800). (Symbol: ● = adsorption branch and ■ = desorption branch). The insets show BJH pore size distribution.

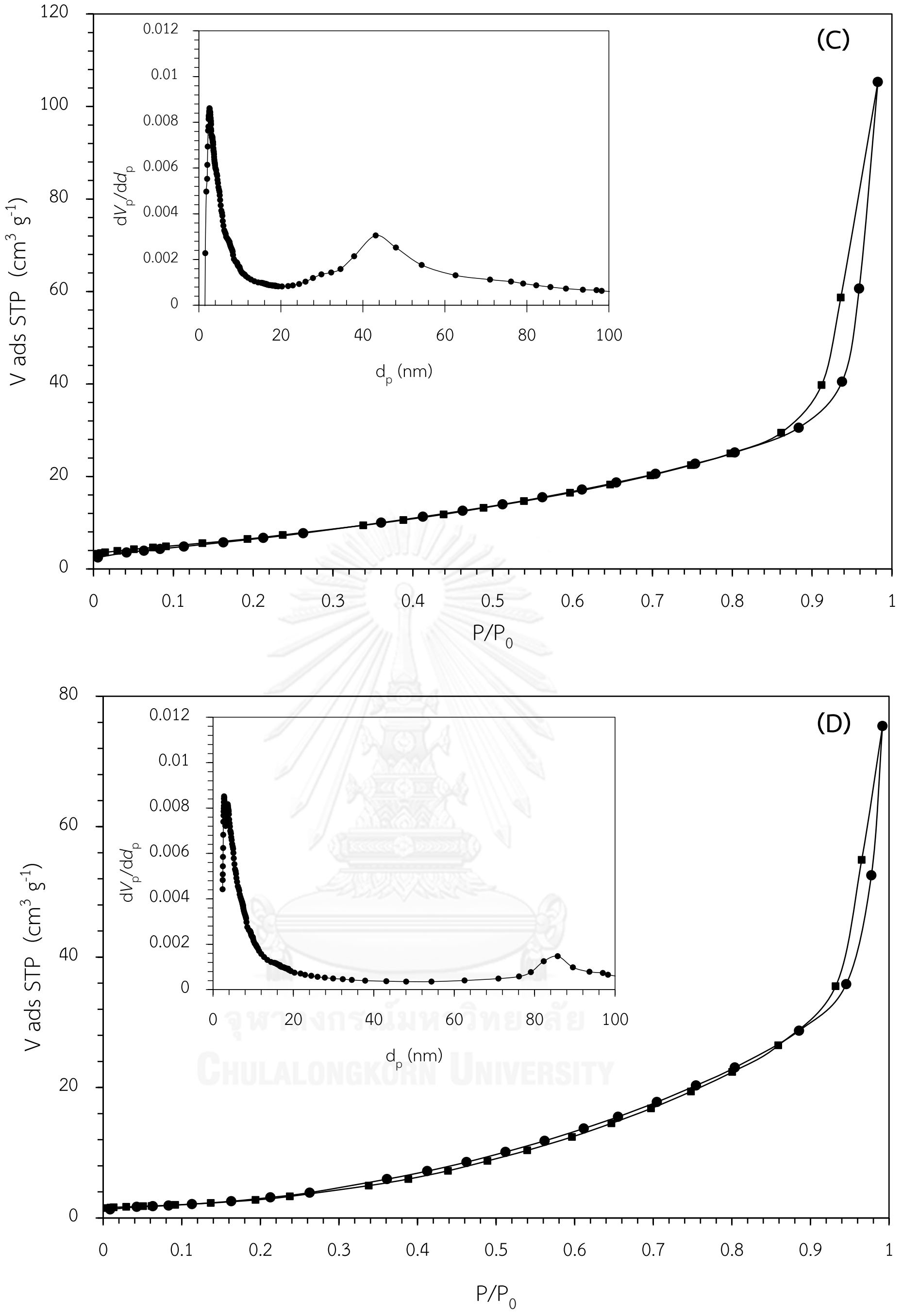

Figure 4.11 (cont.) N_2 adsorption-desorption isotherms of (A) MST-1C-0.17P(500), (B) MST-1C-0.17P(600), (C) MST-1C-0.17P(700)มand (C) MST-1C-0.17P(800). (Symbol: ● = adsorption branch and ■ = desorption branch). The insets show BJH pore size distribution.

Table 4.3 Textural properties of MSTs calcined at different temperatures

Sample	S_{BET} (m^2 g^{-1})	D_p (nm)	V_p (cm^3 g^{-1})
MST-1C-0.17P(500)	46.8	11.2	0.14
MST-1C-0.17P(600)	41.5	18.4	0.20
MST-1C-0.17P(700)	25.7	25.4	0.16
MST-1C-0.17P(800)	11.9	37.7	0.11

Figure 4.12 shows morphology of MST-1C-0.17P(500), MST-1C-0.17P(600), MST-1C-0.17P(700), and MST-1C-0.17P(800). It can be seen that the crystallite size of $SrTiO_3$ increased with increasing the calcination temperature. This observation corresponded with the XRD results in Figure 4.10. The porosity of MST decreased with increasing the calcination temperature, whereas a high calcination temperature promoted pore enlargement. The results were consistent with the N_2 adsorption desorption isotherms and BJH plots. The results indicated that sintering effect reduced edges and corners in $SrTiO_3$ crystals, which is active site for adsorption and catalysis. Therefore, the suitable calcination temperature to prepare the MST with good structural and textural properties was 600 °C.

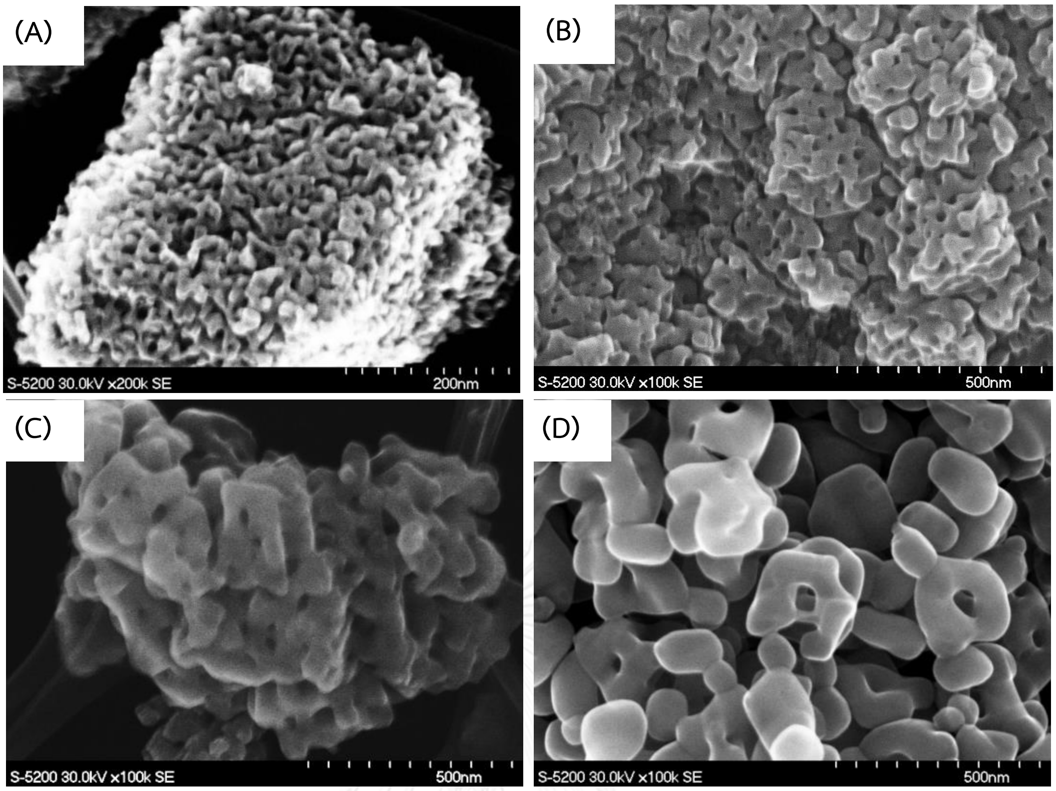

Figure 4.12 STEM micrographs of (A) MST-1C-0.17P(500) at magnification of 200000×, (B) MST-1C-0.17P(600), (C) MST-1C-0.17P(700) and (D) MST-1C-0.17P(800) at magnification of 100000×.

4.4 Pathway for the formation of mesoporous $SrTiO_3$.

The formation of mesoporous $SrTiO_3$ materials under these conditions cannot be simply explained by a soft template mechanism [42]. The pathway to obtain MST was presented in Figure 4.16. The added citric acid helped to stabilize the metal species by decreasing hydrolysis and condensation rates [82, 83], providing the homogeneous distribution of metal ions as the citrate complexes that sufficiently interacted with hydrophilic domains of tri-block copolymers, which lead to mesophase assembly during ageing solution. As suggested by the TG/DTA results, the combustion of citrate complexes induced carbonization of the block copolymer molecules, producing in situ carbon residue and metal oxides-carbon composite as a hard template. The rigidness and thermal stability of the carbon template could retain the self-assembly of mesoporous $SrTiO_3$ crystallized during the calcination. Unlike the typical $SrTiO_3$, the crystals of MST synthesized with citric acid addition were linked their edges and corners together. It should be accounted for by the combustion of metal citrates generating high thermal energy that induced the crystals fusion [57] and burn out the carbon template, creating mesoporous $SrTiO_3$.

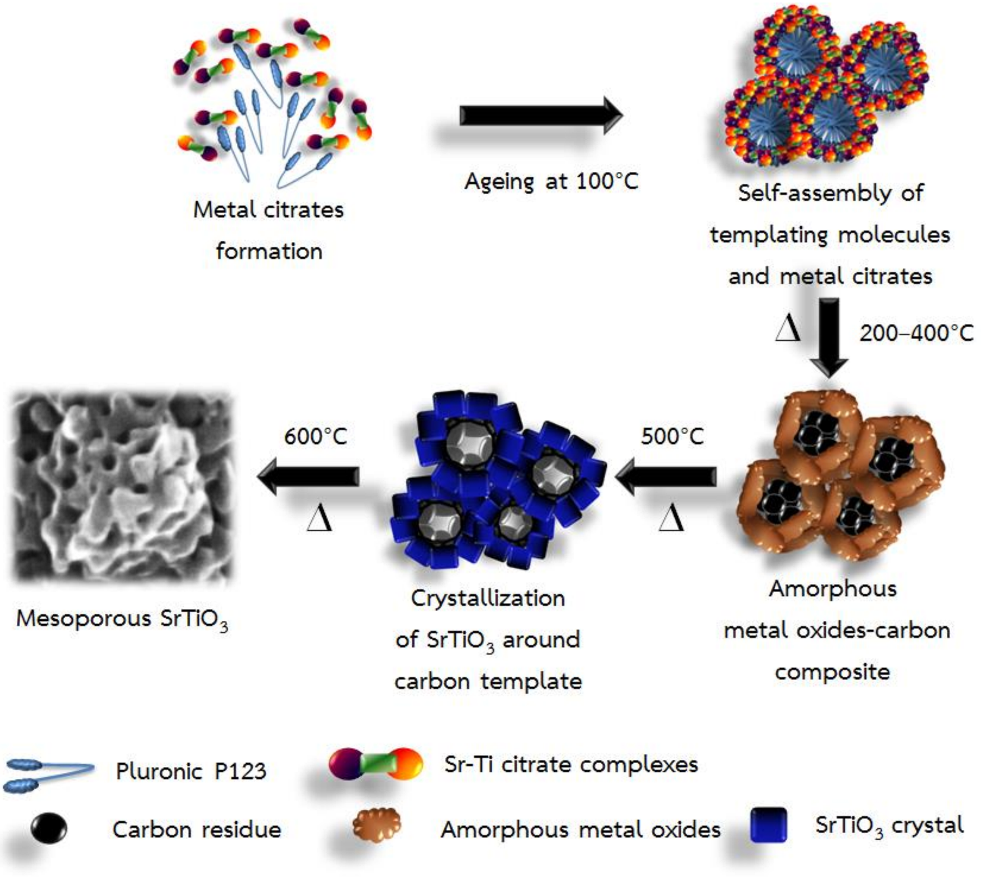

Figure 4.13 The pathway for the formation of MST.

CHAPTER V

Catalytic performance of MSTs in synthesis of fatty acid methyl esters via transesterification

In this Chapter, two MST samples prepared under different conditions (MST-0C-0.17P(600) and MST-1C-0.17P(600)) were comparatively investigated as heterogeneous catalysts in the transesterification of palm kernel oil (PKO) with methanol to produce fatty acid methyl esters (FAMEs). The reaction parameters, including the molar ratio of methanol: oil, catalyst loading, reaction time and reaction temperature, were optimised. Moreover, this chapter reported the effect of adding free fatty acid (FFA) and water in the reaction mixture on FAME yield of the resultant products. Finally, the kinetics and thermodynamics of the transesterification of PKO with methanol were examined.

5.1 Determination of acidic and basic properties of MSTs by Hammett indicator and titration methods

The acidity and basicity of catalyst are important properties, which determine reaction rate and FAME yield in transesterification of triglyceride with methanol. MST-0C-0.17P(600) and MST-1C-0.17P(600) were analysed for their a basic properties by using Hammett indicators and titration with benzoic acid. As shown in Table 5.1, although both of the freshly prepared MST catalysts exhibited basic strength in the same range of $15.0< H\_<9.8$, MST-0C-0.17P(600) possessed higher total basicity than the MST-1C-0.17P(600). After washing with 50 mL of methanol at room temperature for 15 min, followed by calcining at 350 °C for 4 h, a remarkable loss of total basicity, from 0.298 mmol g^{-1} to 0.188 mmol g^{-1}, was observed for MST-0C-0.17P(600). This result suggested that the basic sites of MST-0C-0.17P(600) were easily leached in the presence of excess methanol. Thus, MST-0C-0.17P(600) was expected to have a low stability in the transesterification. Interestingly, the number of basic sites remained intact in the case of MST-1C-0.17P(600) after washing with methanol. The results emphasised that the crystallinity of the $SrTiO_3$ can enhance the chemical stability of the catalyst.

In addition, MST samples were analysed for their acid strength and acid amount by using Hammett indicators and *n*-buthylamine titration method, respectively. Similar to the case of basic properties, acid strength of both MSTs was in the same range of $3.3< H\_<4.8$ but MST-1C-0.17P(600) had higher total acidity than MST-0C-0.17P(600). A dramatic loss of total acidity was observed for MST-0C-0.17P(600) after washing with methanol.

These results emphasized that MST samples possesses both acid and basic sites on their surface due to acidity and basicity of TiO-based and SrO-based termination, respectively. Moreover, this material exhibited more basic character than acid character. The ratio of basicity: acidity of MST depended on terminating species on $SrTiO_3$ crystals.

Table 5.1 Acidic and basic properties of the MST-0C-0.17P(600) and MST-1C-0.17P(600)

Sample	Basic properties		Acidic properties	
	Basic strength ($H\_$)[a]	Total basicity (mmol g^{-1})[b]	Acidic strength ($H\_$)[a]	Total acidity (mmol g^{-1})[c]
MST-0C-0.17P(600)	$15.0<H\_<9.8$	0.298	$3.3<H\_<4.8$	0.078
MST-1C-0.17P(600)	$15.0<H\_<9.8$	0.200	$3.3<H\_<4.8$	0.098
MST-0C-0.17P(600) (washed with methanol)	$15.0<H\_<9.8$	0.188	$3.3<H\_<4.8$	0.026
MST-1C-0.17P(600) (washed with methanol)	$15.0<H\_<9.8$	0.200	$3.3<H\_<4.8$	0.089
MST-0C-0.17P(600) (spent)	$15.0<H\_<9.8$	0.126	*n.d.*[d]	*n.d.*
MST-1C-0.17P(600) (spent)	$15.0<H\_<9.8$	0.199	*n.d.*	*n.d.*

[a] Determined by using Hammett indicators.

[b] Determined by benzoic acid titration method.

[c] Determined by *n*-buthylamine titration method.

[d] *n.d.* = not determined.

5.2 Effect of reaction parameters on the FAME yield

Table 5.2 summarizes the FAME yield attained from the transesterification of PKO with methanol using MST-0C-0.17P(600) as the catalyst under different reaction conditions. The FAME yield increased remarkably from 31.2 to 99.8 wt% when the molar ratio of methanol: oil was increased from 5: 1 to 20: 1 (Entry 1,2 and 3, respectively). The transesterification is an equilibrium reaction that theoretically requires 3 mole of methanol per 1 mole of triglyceride. An excess amount of methanol is beneficial to shift the equilibrium to the product formation side. Moreover, the surplus methanol was necessary in the studied conditions under which the reaction was carried out at 150–170 °C and the autogenous pressure induced by the methanol vaporised. When the amount of MST-0C-0.17P(600) used in the reaction was increased from 1 to 10 wt% (Entry 4, 5, and 3, respectively), the formation of FAME was enhanced due to an increase in the number of active sites responsible for the transesterification. The FAME yield of 99.8 wt% was achieved at 10 wt% catalyst loading. In addition, the effect of reaction time on the FAME yield was studied at 1, 2 and 3 h (Entry 6, 7 and 3, respectively). The FAME yield increased from 31.3 to 99.8 wt% when the reaction time was prolonged to 3 h. Generally, the reaction catalyzed via the heterogeneous route requires a relatively long time when compared to the conventional homogeneous catalysis, since the diffusion of reactants through the external surface film and intraparticle pores inserts the mass transfer limitation.

Table 5.2 Effect of reaction parameters on the FAME yield attained from the transesterification of PKO with methanol over the MST-0C-0.17P(600) catalyst at 150 °C

Entry	Methanol: oil	Catalyst loading (wt%)	Reaction time (h)	FAME yield (wt%)
1	5	10	3	31.2
2	10	10	3	78.2
3	20	10	3	99.8
4	20	1	3	51.1
5	20	5	3	77.9
6	20	10	1	31.3
7	20	10	2	83.3

The effect of reaction parameters on the FAME yield attained from the transesterification over the MST-1C-0.17P(600) catalyst is shown in Table 5.3. When the reaction temperature was set at 150 °C, MST-1C-0.17P(600) gave the FAME yield of 81.1 wt% (Entry 1), which was lower than using MST-0C-0.17P(600) as the catalyst. This should be explained by the presence of soluble base species leached from MST-0C-0.17P(600), as suggested by the basicity measurement (Table 5.1). To obtain the highest FAME yield (99.8 wt%) comparable to the case of MST-0C-0.17P(600), the transesterification over the MST-1C-0.17P(600) catalyst had to be performed at 170 °C (Entry 4). For the effect of other reaction parameters, MST-1C-0.17P(600) exhibited a similar trend to MST-0C-0.17P(600). An additional experiment was also carried out to investigate the homogeneous catalysis contributed by the leached metals. The fresh catalysts were mixed with methanol at 150 °C (MST-0C-0.17P(600)) or 170 °C (MST-1C-0.17P(600)) for 3 h. After removing the solid catalyst by centrifugation, the supernatant was subjected to the transesterification of PKO with methanol under the suitable conditions for each catalyst. It was found that the FAME yield of 21.2 and 5.8 wt% was attained in the supernatant separated from MST-0C-0.17P(600) and MST-1C-0.17P(600), respectively. This result indicated that a significant homogeneous catalysis was inevitable when using the MST-0C-0.17P(600) catalyst, whereas the MST-1C-

0.17P(600) with a highly crystalline perovskite phase was more chemically stable in methanol.

Table 5.3 Effect of reaction parameters on the FAME yield attained from the transesterification of PKO with methanol over the MST-1C-0.17P(600) catalyst at 170 °C

Entry	Methanol: oil	Catalyst loading (wt%)	Reaction time (h)	FAME yield (wt%)
1	20	10	3	81.1[a]
2	5	10	3	41.2
3	10	10	3	89.3
4	20	10	3	99.8
5	20	1	3	30.3
6	20	5	3	81.9
7	20	10	1	30.4
8	20	10	2	78.9

[a] Reaction temperature = 150 °C.

5.3 Effect of adding free fatty acid (FFA) and water in the transesterification

Free fatty acid (FFA) and water containing in the oil feedstock are usually defined as poisons for alkaline catalysts used in conventional biodiesel production [73, 74, 87]. A similar detrimental effect was also observed in the transesterification over solid base catalysts [74, 88]. Figure 5.1 reveals the effect of adding oleic acid (oleic acid = 65.0–88.0 wt%, linoleic acid ≤ 18.0 wt%, palmitic acid ≤ 16.0 wt%, and stearic acid ≤ 8.0 wt%) as model FFA on the FAME yield obtained from the transesterification of PKO with methanol using MST-0C-0.17P(600) and MST-1C-0.17P(600) as heterogeneous catalysts. An amount of added FFA of less than 10 wt% (based on the weight of PKO) slightly affected the FAME formation over the MST-1C-0.17P(600) catalyst. At the FFA content of 5 wt%, however, the FAME yield was dramatically decreased when the reaction was catalyzed by MST-0C-0.17P(600).

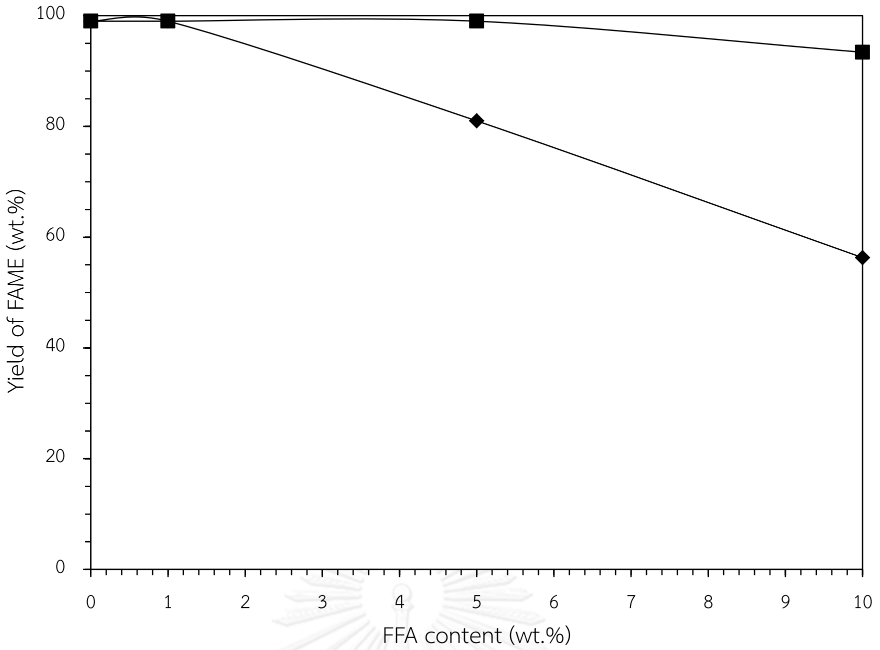

Figure 5.1 Effect of adding FFA on the FAME yield attained from the transesterification of PKO with methanol over (◆) MST-0C-0.17P(600) and (■) MST-1C-0.17P(600). Reaction conditions: methanol: oil molar ratio, 20; catalyst loading, 10 wt%; time, 3 h; temperature, 150 °C (for MST-0C-0.17P(600)) and 170 °C (for MST-1C-0.17P(600)).

The FAME composition of the products attained from the transesterification over MST-0C-0.17P(600) and MST-1C-0.17P(600) with and without the FFA addition was normalised. As shown in Figure 5.2, both catalysts exhibited an increase in the proportion of C16 and C18:1 FAMEs to a similar extent when adding 5 wt% FFA in the feedstock. Since the model FFA used was composed of 65–88 wt% oleic acid and also contained C16 fatty acids, this result suggested that the esterification of FFA added with methanol occurred in the reaction system. The esterification of carboxylic acid with alcohol is an endothermically autocatalytic reaction. However, the measurement of acid value and FFA content of the reaction mixture (Table 5.4) before and after heating PKO mixed with methanol and 10 wt% FFA, in the absence of any solid catalyst at 170 °C for 3 h (Entry 1), indicated that the autocatalysis was not significant under the studied conditions. The FFA content was remarkably decreased in the presence of either MST-0C-0.17P(600) (Entry 3) or MST-1C-0.17P(600) (Entry 6). There was no soap visually observed in any cases. These results suggested that the MST catalysts had esterification activity. As shown in Table 5.1, a small amount of weak acid sites was detected on both catalysts, probably related to the acidity of TiO_2 [89].

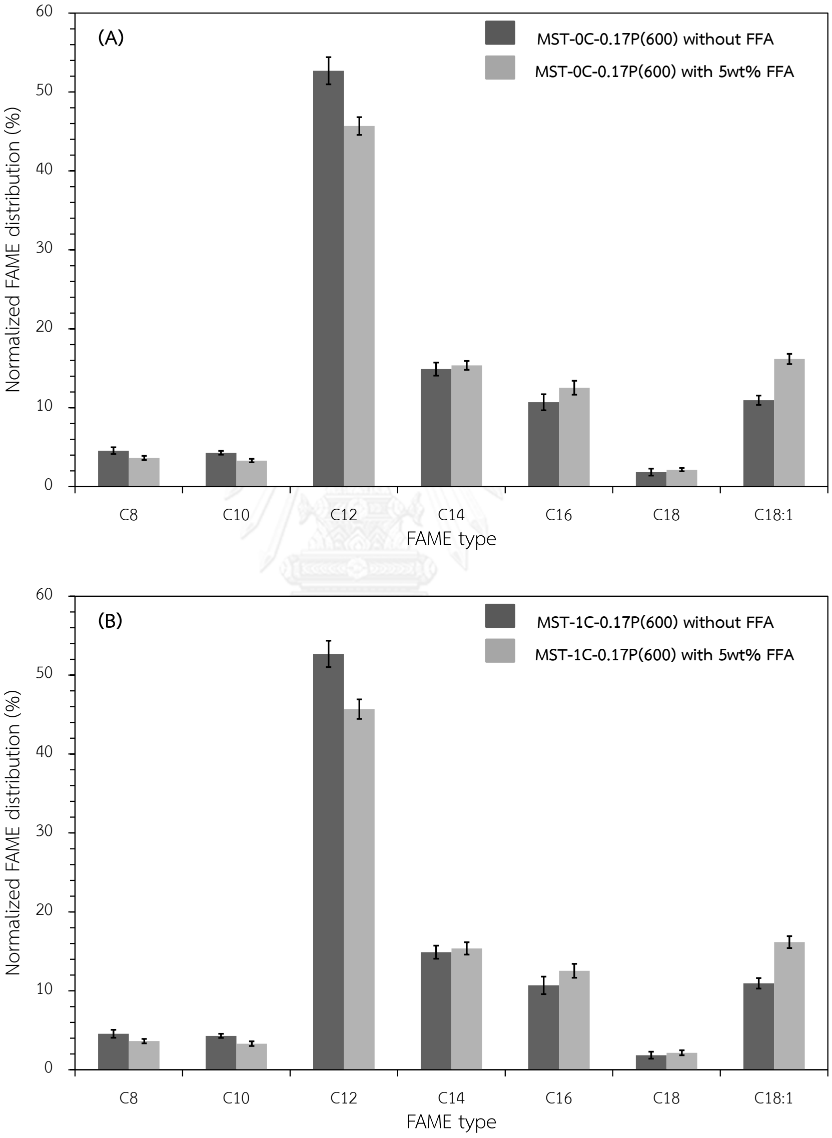

Figure 5.2 Effect of adding oleic acid as model FFA on the normalized composition of FAME products attained from the transesterification of PKO with methanol over (A) MST-0C-0.17P(600) and (B) MST-0C-0.17P(600). Reaction conditions: methanol: oil molar ratio, 20; catalyst loading, 10 wt%; time, 3 h; temperature, 150 °C (for MST-0C-0.17P(600)) and 170 °C (for MST-1C-0.17P(600)).

Table 5.4 Effects of adding FFA and water in the transesterification[a] of PKO with methanol on the acid value and FFA content of the resulting product mixture

Entry	Catalyst	Feedstock	Acid value (mg KOH/g oil)[b]	FFA content (wt%)[b]
1	No catalyst[c]	PKO + 10 wt% FFA	23.75±0.32	11.95±0.16
2	MST-0C-0.17P(600)	PKO	1.13±0.04	0.57±0.012
3	MST-0C-0.17P(600)	PKO + 10 wt% FFA	1.94±0.03	0.98±0.01
4	MST-0C-0.17P(600)	PKO + 10 wt% water	1.69±0.07	0.85±0.01
5	MST-1C-0.17P(600)	PKO	1.39±0.08	0.70±0.02
6	MST-1C-0.17P(600)	PKO + 10 wt% FFA	6.16±0.14	3.10±0.07
7	MST-1C-0.17P(600)	PKO + 10 wt% water	2.26±0.10	1.14±0.02

[a] Reaction conditions: methanol: oil molar ratio, 20; catalyst loading, 10 wt%; time, 3 h; temperature, 150 °C (for MST-0C-0.17P(600)) and 170 °C (for MST-1C-0.17(600)).

[b] Determined by titration method.

[c] Reaction temperature = 170 °C.

Although the amount of FFA added could be reduced by the catalytic esterification, a severe drop of FAME yield was only observed in the case of the MST-0C-0.17P(600) catalyst. It is likely that the basic sites responsible for the transesterification on MST-0C-0.17P(600) were deactivated more easily than those on MST-1C-0.17P(600). The XRD patterns of MST-0C-0.17P(600) before and after being used in the transesterification of PKO with the addition of 10 wt% FFA are compared in Figure 5.3. The spent MST-0C-0.17P(600) catalyst (Figure 5.3 (b)) exhibited not only a decrease in the intensity of perovskite $SrTiO_3$ but also an undetectable the impurity phase such as $SrCO_3$, $SrCl_2$, and $SrCl_2.H_2O$.

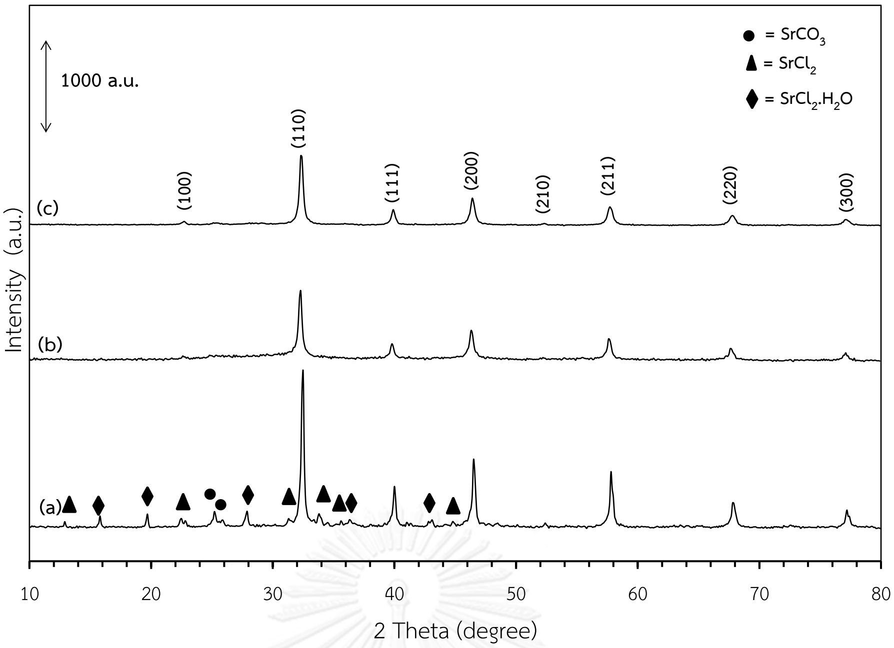

Figure 5.3 XRD patterns of (a) fresh MST-0C-0.17P(600), (b) MST-0C-0.17P(600) spent in the transesterification with addition of 10 wt% FFA, and (c) spent MST-0C-0.17P(600) after calcination at 350 °C. Miller indexes indicate $SrTiO_3$ with perovskite structure.

On the other hand, the crystalline structure of MST-1C-0.17P(600) remained intact after being used in the reaction with adding 10 wt% FFA, as evidenced by the XRD patterns in Figures 5.4(a) and 5.4(b). Therefore, the catalytic stability of MST-1C-0.17P(600) in the presence of high FFA content can be attributed to the high crystallinity of the perovskite phase.

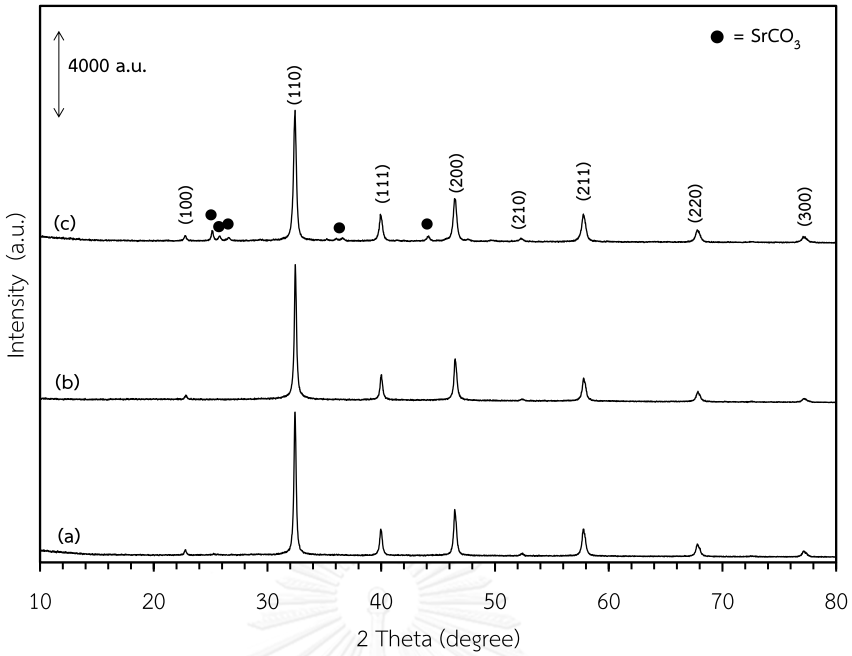

Figure 5.4 XRD patterns of (a) fresh MST-1C-0.17P(600), (b) MST-1C-0.17P(600) spent in the transesterification with addition of 10 wt% FFA, and (c) spent MST-1C-0.17P(600) after calcination at 350 °C. Miller indexes indicate $SrTiO_3$ with perovskite structure.

Figure 5.5 shows the FAME yield attained from the transesterification of PKO with methanol in the presence of water (1–10 wt% based on the weight of PKO). Likely to the effect of FFA, the MST-1C-0.17P(600) was remarkably tolerant to the water added, of which the 10 wt% content decreased the FAME yield to 88.4 wt%. However, the amount of FAME formed over the MST-0C-0.17P(600) catalyst was severely dropped when the amount of water added was 5 wt%. As shown in Table 5.4, the titration of the reaction products attained from the transesterification with adding 10 wt% water indicated that the acid value and the FFA content were slightly increased (Entries 4 and 7). This should be accounted for by hydrolysis of triglycerides, which is favourable at high temperatures. The catalytic stability of MST-1C-0.17P(600) a in high water content should be related to the crystallinity of the Sr and Ti mixed oxide phase, in which the basic sites are strongly attached and secured. It is worth noting that the detrimental effect of water is more harmful to the FAME yield than that of FFA because the water molecule is much smaller and more polar than oleic acid as FFA model.

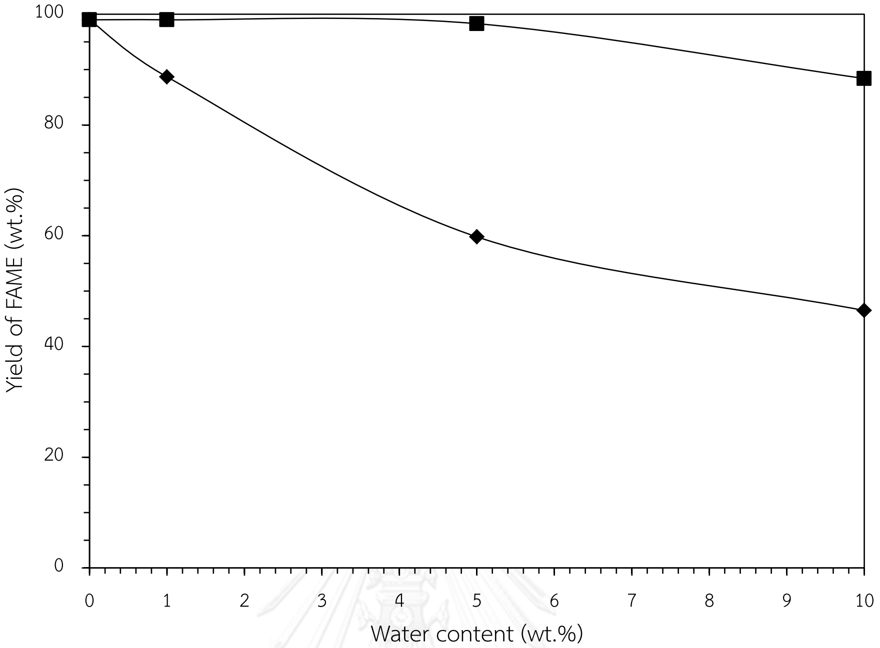

Figure 5.5 Effect of water addition on the FAME yield attained from the transesterification of PKO with methanol over (♦) MST-0C-0.17P(600) and (■) MST-1C-0.17P(600). Reaction conditions: methanol: oil molar ratio, 20; catalyst loading, 10 wt%; time, 3 h; temperature, 150 °C (for MST-0C-0.17P(600)) and 170 °C (for MST-1C-0.17P(600)).

5.3 Catalyst reusability and deactivation

In order to study reusability, the MST catalysts (MST-0C-0.17P(600) and MST-1C-0.17P(600)) used in the first run were separated from the reaction mixture by centrifugation, followed by washing with methanol. The washed catalysts were calcined at 350 °C for 4 h before being used in the next run. The transesterification was carried out under the suitable conditions for each MST catalyst. It was found that the FAME yield decreased from 99.8 wt% to 75.9 wt% and 85.7 wt% in the cases of MST-0C-0.17P(600) and MST-1C-0.17P(600), respectively. The observed loss of activity corresponded with a decrease in the total basicity of the catalysts. As shown in Table 5.1, the basicity of MST-0C-0.17P(600) was reduced by more than 50% after the first use. This should be attributed to a loss of catalytically basic sites by the leaching effect. However, the number of basic sites was slightly decreased for the spent MST-1C-0.17P(600) catalyst, probably as a result of its highly crystalline $SrTiO_3$ perovskite. The structural analysis of the MST-1C-0.17P(600) spent in the transesterification, followed by calcination at 350 °C, evidenced the formation of $SrCO_3$ as a new phase (Figure 5.4 (c)). The metal carbonate, derived from the chemisorption of CO_2 onto the basic sites during the catalyst recovery, had much lower basic strength than the corresponding metal oxide [90]. Therefore, the FAME yield drop in the second use of the MST-1C-0.17P(600) catalyst should be related to the transformation of active strontium species to $SrCO_3$. To reactivate the spent catalyst, it must be calcined at temperatures of >1000 °C [91]. In addition, the elemental analysis of both MST catalysts before and after being used in the reaction was conducted by ICP technique. As shown in Table 5.5, the results indicated that molar ratio of Sr: Ti of MST-0C-0.17P(600) was dramatically decreased after the first run while that of MST-1C-0.17P(600) was not significantly changed. It was explained by leaching of the Sr salts as impurity phases in MST-0C-0.17P(600) during reaction. The result was consistent with the XRD analysis in Figure 5.3 (c). The impurity phases ($SrCO_3$, $SrCl_2$, and $SrCl_2.H_2O$) were not detected in the spent MST-0C-0.17P(600). The elemental analysis of the spent catalyst confirmed the beneficial effect of high crystallinity on chemical and structural stability of MST-1C-0.17P(600).

Table 5.5 Elemental compositions of fresh MST-0C-0.17P(600) and MST-1C-0.17P(600) before and after being used in the transesterification of PKO with methanol[a] for 2 cycles.

Sample	Sr (ppm)	Ti (ppm)	Sr: Ti (wt)	Sr: Ti (mol)
Fresh MST-0C-0.17P(600)	2.82	1.15	2.45:1	1.34:1
Spent MST-0C-0.17P(600)[b]	2.36	1.09	2.16:1	1.18:1
Fresh MST-1C-0.17P(600)	2.76	1.38	2.00:1	1.09:1
Spent MST-1C-0.17P(600)[b]	2.70	1.37	1.97:1	1.07:1

[a] Reaction conditions: methanol: oil molar ratio, 20; catalyst loading, 10 wt%; time, 3 h; temperature, 150 °C (for MST-0C-0.17P(600)) and 170 °C (for MST-1C-0.17P(600)).

[b] Spent MSTs were washed with methanol, dried in oven at 100 °C overnight, and the calcined at 350 °C for 4 h.

5.4 Kinetics and thermodynamics of transesterification over MST catalyst

Figure 5.6 shows PKO conversion at any given time. The PKO conversion is defined as mole of triglycerides (TG) converted per mole of the initial TG used in the reaction. If a volume change during the reaction was neglected, FAME yield (*X*) is given by Eq (4.1) [92].

$$X = 1 - ([TG]_t / [TG]_0) \qquad (4.1)$$

where X = FAME yield (mol%).

$[TG]_t$ = molar concentration of TG at time = t

$[TG]_0$ = molar concentration of TG at initial time

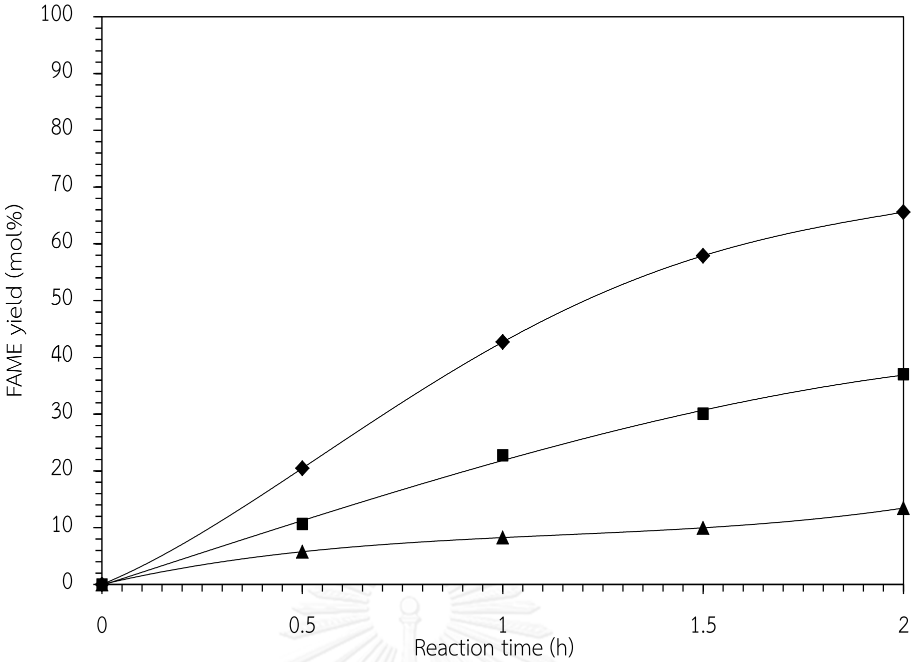

Figure 5.6 FAME yield vs time plot obtained from transesterification of PKO with methanol over MST-1C-0.17P(600) catalyst at different temperatures; (▲) 120 °C (■) 150 °C and (♦) 170 °C. Reaction conditions: methanol: oil molar ratio, 20; catalyst loading, 10 wt%.

In this work, the transesterification of PKO with methanol was assumed to follow pseudo-first-order kinetics because the reaction was carried out in an excess of methanol. This assumption was in accord with the previous research [69]. Thus, the kinetic model of MST-1C-0.17P(600)-catalyzed transesterification can be calculated as Eq. (3.5).

$$-\ln(1-X) = kt \tag{3.5}$$

where k = the first order rate constant (h^{-1})

X = FAME yield (mol%).

t = reaction time (h)

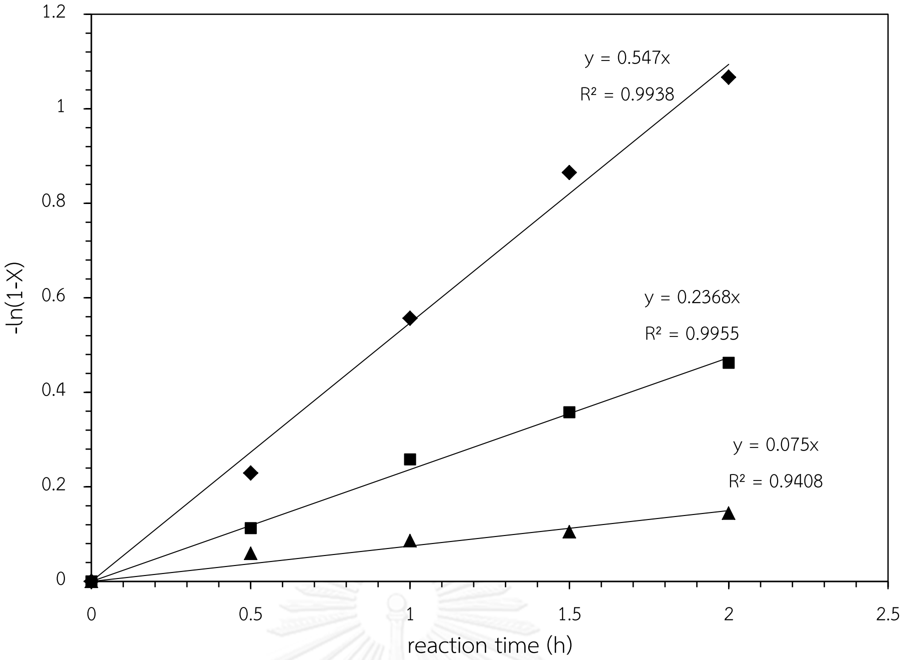

Figure 5.7 Plots of -ln(1-*X*) vs. reaction time at different temperatures for kinetic study of transesterification of PKO with methanol over MST-1C-0.17P(600) catalyst; (▲) 120 °C (■) 150 °C -and (♦) 170 °C. Reaction condition methanol: oil molar ratio, 20; MST-C1-P0.17(600) loading, 10 wt%.

As shown in Figure 5.7, the linear plots between -ln(1-*X*) and t confirmed that the transesterification over MST-1C-0.17P(600) has followed the pseudo-first order rate law. The apparent first order rate constants (k) derived from the slopes were found to be 0.075 h^{-1}, 0.2368 h^{-1} and 0.547 h^{-1} at 120 °C, 150 °C and 170 °C, respectively.

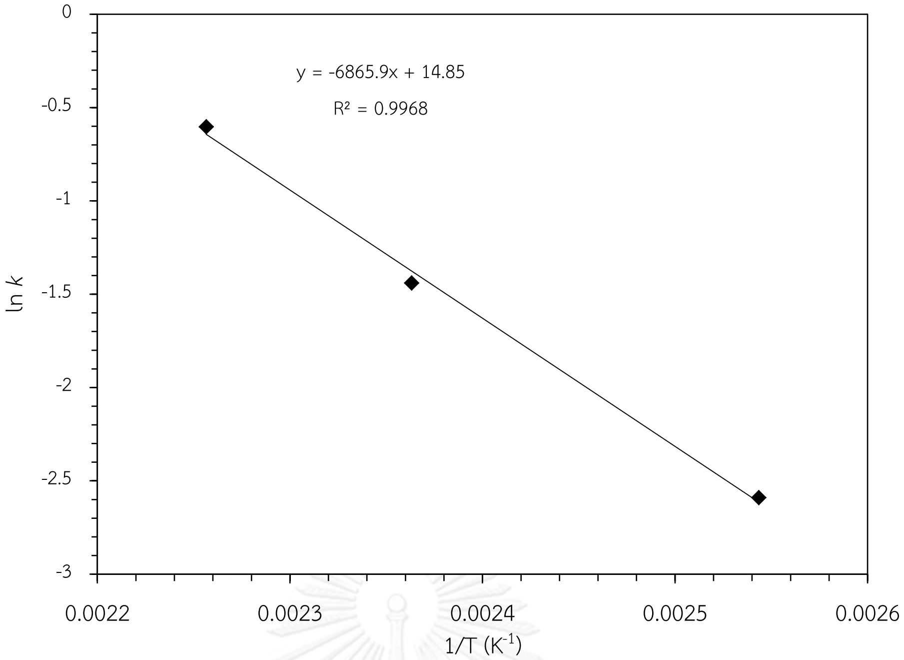

Figure 5.8 Arrhenius plot of ln *k* vs 1/T for the transesterification of PKO with methanol over MST-1C-0.17P(600) catalyst. Reaction condition methanol: oil molar ratio, 20; MST-C1-P0.17(600) loading, 10 wt%.

Subsequents, the activation energy (E_a) of the transesterification was calculated by Arrhenius equation as followed Eq.(3.6).

$$\ln k = \ln A - E_a/RT \qquad (3.6)$$

where E_a = activation energy (kJ mol^{-1})
A = pre-exponential factor (h^{-1})
R = gas constant (8.314 x 10^{-3} kJ K^{-1} mol^{-1})
T = reaction temperature (K).

A liner plot between ln *k* vs 1/T is shown in Figure 58. The value of E_a from Arrhenius plot was found to be 57.1 kJ mol^{-1}. The E_a obtained in this work was in the range of the reported values (26–82 kJ mol^{-1}) for the transesterification reaction catalyzed by other heterogeneous catalysts [69, 93]. Moreover, the E_a of >26 kJ mol^{-1}

indicated that the transesterification of PKO with methanol over MST-1C-0.17P(600) is a chemically controlled reaction, and not controlled by a mass diffusion step [69].

CHAPTER VI

Nature of active site on MST surface

The results in Chapter VI were divided into two parts. The first part focused on clarification of acidic and basic nature of MST-1C-0.17P(600). The acid properties were determined by adsorption of pyridine, as probe molecule, onto the MST sample, followed by Fourier-transform infrared (FTIR) spectroscopic study. The basic properties were also examined using a similar procedure but probe molecule was changed to pyrrole. In the other part, adsorption of methanol and ethyl propionate as model reactant molecules on the MST-1C-0.17P(600) surface was studied by *in situ* FTIR technique. Finally, mechanism for the transesterification over MST-1C-0.17P(600) was proposed.

6.1 Acidic and basic properties of MST

6.1.1 Pyridine adsorption

Pyridine is a basic molecule that has been extensively used to probe the presence and nature of acid sites on surface of metal oxides [71]. The acidity of MST-1C-0.17P(600) was determined by adsorption of pyridine at 150 °C followed by FTIR spectroscopic study. The FTIR spectra of MST-1C-0.17P(600) adsorbed with pyridine, followed by desorption of pyridine at different temperatures are shown in Figures 6.1 and 6.2. The observed IR bands of in the ring breathing vibration (ν_{CCN}) region are summarized in Table 6.1. Moreover, different configurations of adsorbed pyridine species on general oxide surfaces are illustrated in Figure 6.3.

Figure 6.1 shows the FTIR bands at wavenumbers between 3700 and 3300 cm^{-1}, which can be used to categorize the type of hydroxyl group (O-H) on the MST-1C-0.17P(600) surface. The band at 3665 cm^{-1} was attributed to the O-H stretching of Sr-O-H and/or Ti-O-H [67, 94]. This band became negative upon contacting the MST sample with pyridine vapor, indicating that of Sr-O-H was perturbed by pyridine molecule. The bands at 3565, 3470, 3405 and 3340 cm^{-1} should be assigned to the

O-H stretching vibration of Sr-(O-H)-Ti species locating in different crystallographic plane of $SrTiO_3$. The band at 3065 cm^{-1} corresponded to the C-H stretching of aromatic ring pyridine [67, 71].

The FTIR spectra in region of 1700 and 1400 cm^{-1} presented in Figure 6.2, which can be used to differentiate the configuration of pyridine adsorbed on MST-1C-0.17P(600) surface. The bands at 1443, 1596, and 1620 cm^{-1} corresponded to the ν_{CCN} of pyridine coordinated with Lewis acid sites (LPyri) of MST-1C-0.17P(600). The band at 1575 cm^{-1} was derived from pyridine interacted with weakly acidic hydroxyl groups via hydrogen bonding (HPyri). The band at 1490 cm^{-1} was associated with both Lewis and Brønsted sites (BPyri). However, none of band was detected at 1545 and 1635 cm^{-1}, which is characteristic band of pyridium ion interacted with Brønsted acid sites [71]. Therefore, the band at 1490 cm^{-1} should be only related to pyridine adsorbed on Lewis acid site. According to the literature [67], the presence of band at 1596 cm^{-1} and a shoulder at 1606 cm^{-1} was attributed to pyridine coordinated with Sr^{2+} and Ti^{4+}, respectively. Hence, the Lewis acidity of MST materials was possibly present in metal cations (Sr^{2+} and Ti^{4+})

After the pyridine adsorption at 150 °C, the sample was heated stepwise from 150 °C to 200 °C and 250 °C to probe the strength of the acid sites. It can be seen that the band intensity was decreased with increasing the desorption temperature. The H-bonded pyridine species (1575 cm^{-1}) nearly disappeared at 200 °C (Figure 6.2(b)), confirming its weak interacting on the MST surface. Moreover, none of band was observed at 250 °C (Figure 6.2(c)), indicating that all pyridine molecules were desorbed from the acid sites. Thus, it can be concluded that the Lewis acid sites of MST-1C-0.17P(600) have weak-to-moderate strength.

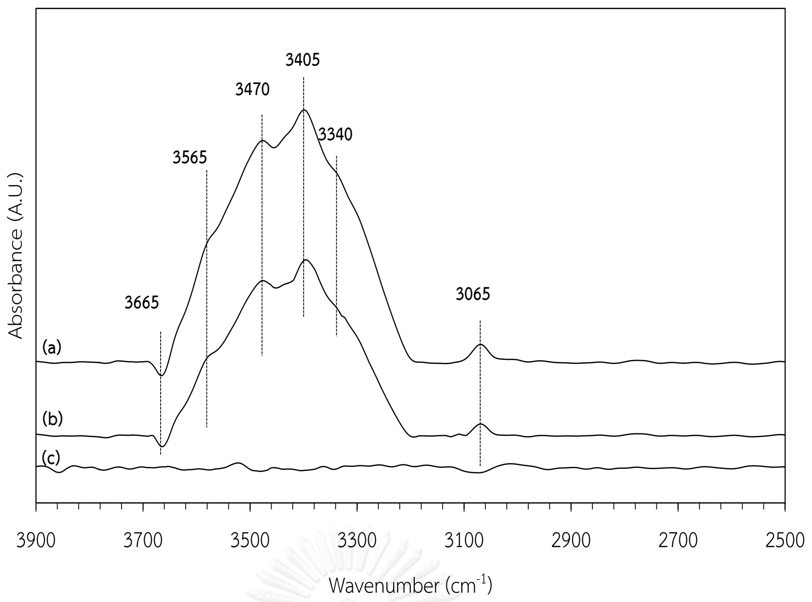

Figure 6.1 FTIR spectra in the O-H stretching region of MST-1C-0.17P(600) after pyridine adsorption at 150 °C, followed by desorption at different temperatures: (a) 150 °C, (b) 200 °C, and (c) 250 °C. The reported spectra were subtracted by the spectrum of MST-1C-0.17P(600) without pyridine adsorption.

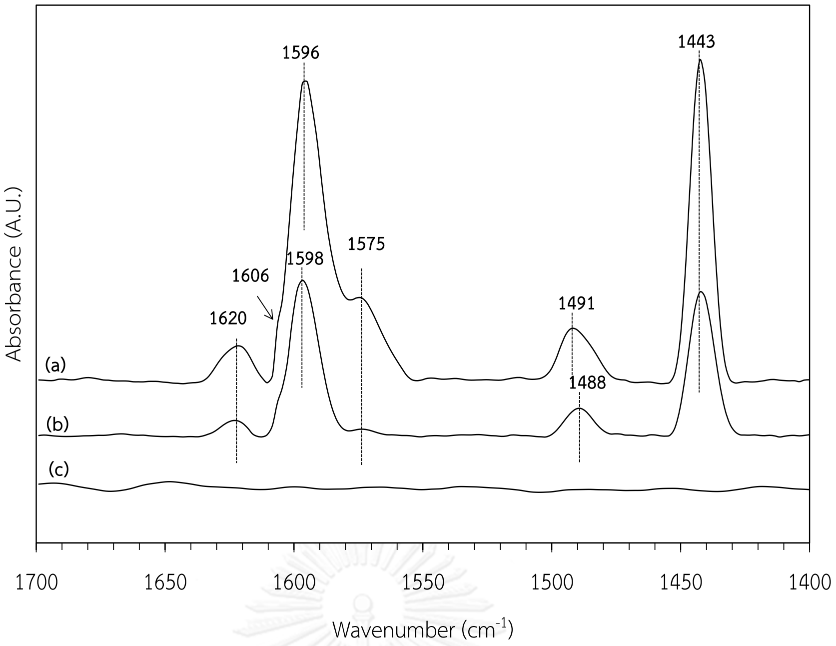

Figure 6.2 FTIR spectra in the ring breathing vibration region of pyridine adsorbed on MST-1C-0.17P(600) at 150 °C, followed by desorption at different temperatures: (a) 150 °C, (b) 200 °C, and (c) 250 °C. The reported spectra were subtracted by the spectrum of MST-1C-0.17P(600) without pyridine adsorption.

Table 6.1 The ring breathing vibration (ν_{CCN}) bands of pyridine adsorbed on MST-1C-0.17P(600)

Adsorbed pyridine species [a]	Ring breathing vibration (ν_{CCN}); cm^{-1}			
	ν_{19b}	ν_{19a}	ν_{8a}	ν_{1+6a}
HPyri			1575	
LPyri	1443		1596	1620
LPyri+BPyri		1491		

[a] HPyri, pyridine H-bonded with weak acidichydroxyl group; LPyri, pyridine coordinated to Lewis acid site; BPyri, pyridine protonated on BrØnsted acid site.

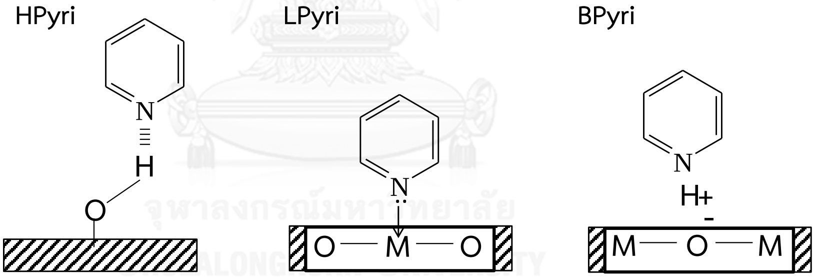

Figure 6.3 Configurations of adsorbed pyridine species on metal oxide surfaces [95].

The amount of Lewis acid sites referenced to unit weight of dry sample, q_H (μmol g^{-1}), can be calculated from Eq. (6.1) [71].

$$q_H = \frac{A_I S}{w \varepsilon} \qquad (6.1)$$

where A_I = integrated absorbance of band (cm^{-1})

S = cross-sectional area of sample disc (cm^2)

w = sample weight (g)

ε = molar extinction coefficient (cm μmol^{-1})

The integrated molar extinction coefficient of the band at 1443 cm^{-1}, corresponding to pyridine adsorption on Lewis acid site, is 1.63 cm μmol^{-1} [96]. Therefore, the amount of acid sites on the MST-1C-0.17P(600) surface was 78.8 μmol g^{-1}.

6.1.2 Pyrrole adsorption

Pyrrole (PYH) is a well-known probe molecule for determination of basic properties [72]. In contrast to pyridine adsorption, since pyrrole readily polymerizes or decomposes upon heating [97], the adsorption of pyrrole on MST-1C-0.17P(600) was conduct at 30 °C and the pyrrole desorption was performed up to 150 °C. The FTIR spectra of MST-1C-0.17P(600) after pyrrole adsorption at 30 °C, followed by desorption at different temperatures are shown in Figures 6.4 and 6.5. The observed IR bands are summarized in Table 6.2. Furthermore, the characteristic bands of gaseous pyrrole and adsorbed pyrrole species are categorized in Table 6.3. The possible configurations of pyrrole adsorbed on different metal oxide surfaces are shown in Figure 6.6.

It was found that there were 4 types of interaction between pyrrole and MST-1C-0.17P(600) surface. Firstly, The bands at 3130, 3055, and 2950 cm^{-1} corresponded to the C-H stretching (ν(CH)) of pyrolate ion, generating form pyrrole molecule was abstracted H^+ by coordinatively unsaturated O^{2-} as strong basic site on MST-1C-

0.17P(600) surface to form surface hydroxide. Furthermore, the pyrrolate anion is hydrogen bonded with the O-H bond on MST-1C-0.17P(600) (OH····PY^-). The bands at 3250 and 1530 cm^{-1}, corresponding to the N-H stretching (ν(NH)) and ring stretching (ν(ring)), respectively, were ascribed to pyrrole H-bonded to oxygen atom of metal-oxygen ion pair (PYH···· O). In case of pyrrole bonded with surface hydroxyl group (PYH···· (OH)), it can be divided into two types. The pyrrole linearly H-bonded to surface OH related to the band at 3585, 3310, 3350, 3130, 1530, and 1049 cm^{-1}. On the other hand, the pyrrole H-bonded to surface OH via cyclic bridge was evidenced by the ν(OH) band at 3450 cm^{-1}, ν(NH) band at 3250 cm^{-1}, and ν(CH) band at 3130 cm^{-1}.

By comparing the wavenumbers of N-H stretching originated from gaseous pyrrole (3527 cm^{-1}), the red shift of ν(NH) corresponded to the strength of basic site. Therefore, the strength of interaction between the adsorbed pyrrole and basic sites was ranked: OH····PY^- > PYH···· O = PYH···· (OH) cyclic bridge > PYH···· (OH) linear bridge.

As a result, it can be concluded that the basicity of MST materials consisted of 4 types of basic site with different basic strength including, coordinatively unsaturated O^{2-}, metal-oxygen ion pairs, monodentate surface hydroxide and bidentate surface hydroxide.

After the pyrrole adsorption, the sample was heated stepwise from 30 °C to 50 °C, 100 °C and 150 °C. Although the band intensity was decreased with increasing the desorption temperature, the characteristic bands of adsorbed pyrrole species were still detected. However, pyrrole desorption was not conducted at temperature higher than 150 °C because pyrrole molecules polymerized [97]. The results suggested that MST-1C-0.17P(600) possessed strong basic sites.

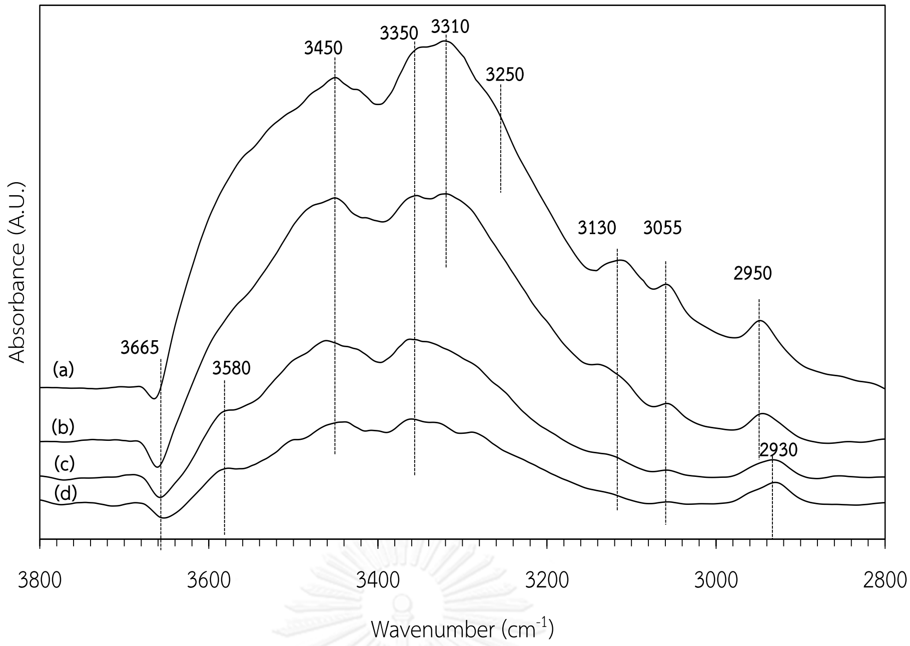

Figure 6.4 FTIR spectra in the O-H, N-H and C-H stretching region of pyrrole adsorbed on MST-1C-0.17P(600) at 30 °C, followed by desorption at different temperatures: (a) 30 °C, (b) 50 °C, (c) 100 °C and (d) 150 °C. The reported spectra were subtracted by the spectrum of MST-1C-0.17P(600) without pyrrole adsorption.

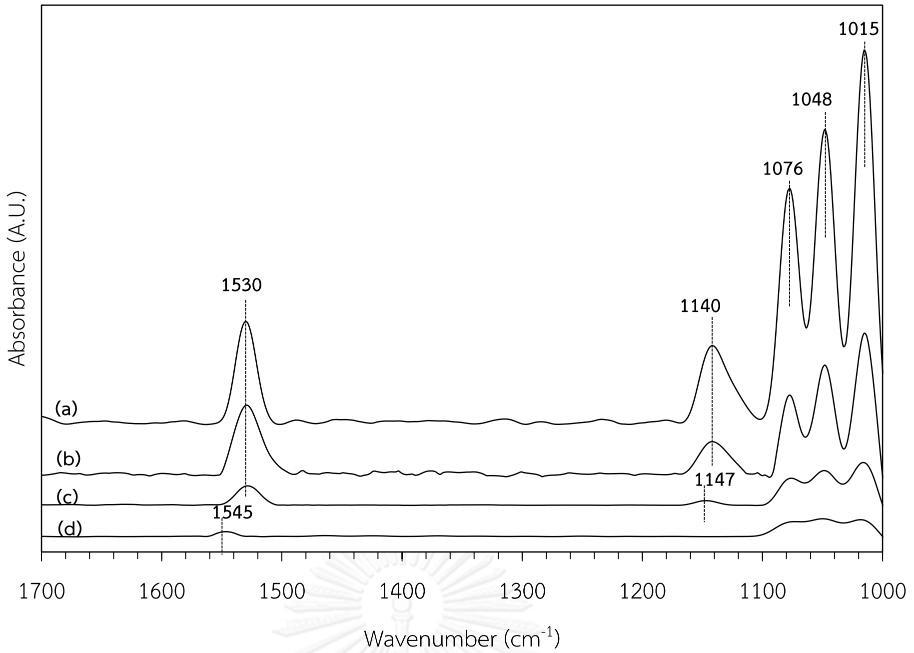

Figure 6.5 FTIR spectra in the ring vibration, N-H and C-H deformation regions of pyrrole adsorbed on MST-1C-0.17P(600) at 30 °C, followed by desorption at different temperatures: (a) 30 °C, (b) 50 °C, (c) 100 °C and (d) 150 °C. The reported spectra were subtracted by the spectrum of MST-1C-0.17P(600) without pyrrole adsorption.

Table 6.2 Assignment of vibration bands observed from pyrrole adsorption on MST-1C-0.17P(600)

Wavenumber (cm^{-1})	Assignment
3665	O-H stretching (surface hydroxyl group of metal hydroxide)
3580	O-H stretching (H-bonded)
3450	N-H stretching (H-bonded)
3350	N-H stretching (H-bonded)
3310	N-H stretching (H-bonded)
3250	N-H stretching (H-bonded)
3105	C-H stretching
3055	C-H stretching
2950	C-H stretching
1530	ring stretching
1140	N-H in plane deformation
1076	C-H out of plane deformation
1048	C-H in plane deformation
1015	C-H in plane deformation

Table 6.3 The characteristic bands of gaseous pyrrole and adsorbed pyrrole species on MST-1C-0.17P(600) [72]

Pyrrole adsorbed species [a]	**Characteristic bands; cm^{-1}**				
	ν (OH)	ν (NH)	ν (CH)	ν (ring)	δ(CH)
PYH(gas)		3527	3148, 3125	1521	1076, 1049, 1015
OH····PY$^-$			3130, 3055, 2950		
PYH···· O		3250		1530	
PYH···· (OH) linear bridge	3580	3350, 3310	3130	1530	1048
PYH···· (OH) cyclic bridge	3450	3250	3130		

[a] OH····PY$^-$, pyrrolate ion interaction; PYH···· O, H-bonded pyrrole; PYH···· (OH), cyclically or linearly H-bonded pyrrole.

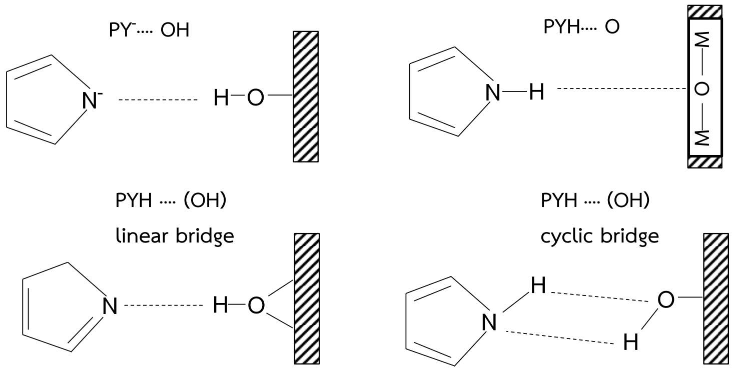

Figure 6.6 Configurations of adsorbed pyrrole species on metal oxide surfaces [72].

6.2 Active sites for adsorption of methanol and ester onto MST catalyst

Although a number of metal oxides were proved to be active catalysts in transesterification of triglyceride with methanol, the intrinsic catalysis taking place is still obscured by a lack of knowledge about the nature of active sites responsible for activating and converting the reactant molecules to the corresponding FAME. In this work, the nature of active sites for adsorption of methanol and ethyl propionate, as the model ester, onto the MST catalyst was examined by contacting the calcined MST-1C-0.17P(600) with vapor of methanol, model ester or both substrates, followed by the FTIR spectroscopic study. The information obtained provided correlations between the active sites and the configurations of adsorbed reactant molecules on the MST surface. By increasing the desorption temperatures, the molecules strongly adsorbed on the active sites were activated, giving details about surface intermediates that are possibly relevant to the reaction. As a result, the reaction mechanism on the MST catalyst can be proposed.

6.2.1 Methanol adsorption

Figure 6.7 shows the FTIR spectra obtained between 3900 and 2800 cm^{-1}, corresponding to the stretching modes of O-H and C-H bonds. The observed bands in this region are summarized in Table 6.4. After the methanol adsorption at 30 °C (spectrum (a)), the negative absorbance at 3695 and 3660 cm^{-1} was attributed to the surface –OH groups on MST-1C-0.17P(600), which were perturbed by methanol molecules [68]. Two broad bands centered at 3455 and 3345 cm^{-1} indicated the presence of methanol molecules H-bonded to different active sites on the MST-1C-0.17P(600) surface [68]. However, the intensity of these two bands decreased with increasing the evacuation temperature (spectrum (b), (c), (d) and (e)). The results indicated that the corresponding adsorbed methanol species were easily desorbed when the temperature was elevated above boiling point of methanol. The bands at 2950, 2845 and 2805 cm^{-1} were ascribed to the stretching vibrations of C-H bonds of methanol (spectrum (a)) [98]. As the evacuation temperature increased, the bands at 2950 and 2845 cm^{-1} were decreased, whereas the new bands at 2928 and 2880 cm^{-1} were observed (spectrum (b), (c), (d) and (e)), indicating a structural change of adsorbed methanol species. This suggested that the active sites of MST-1C-0.17P(600) was able to dissociate the adsorbed methanol, possibly due to its strong basic character [68, 98].

Figure 6.8 shows the FTIR spectra obtained between 1200 and 1000 cm^{-1}, corresponding to the vibration mode of C-O bond, which can be used to classify the nature of adsorbed methanol species on active sites of MST catalyst. According to the previous study, the methanol adsorption on solid base materials gave three distinct bands in this region 1160, 1080 and 1050 cm^{-1}, which correspond to three different adsorbed species, namely species I, II, and H, respectively, as illustrated in Figure 6.9. Species H is molecularly adsorbed methanol without dissociation. This species weakly coordinates with surface metal cation (M^+) and oxygen ion (O^{2-}). In case of species I and II, they are defined as methoxy species, resulting from dissociative adsorption of methanol via breaking of O-H bond of methanol molecule. Species I forms a monodentate linkage, whereas species II is coordinated with two metal ions, so-called bidentate bridge [68]. The band at 1028 cm^{-1} was ascribed to methanol in gas phase. As the evacuation temperature increased, the band at 1028 cm^{-1} was decreased in its intensity, indicating that the gaseous methanol molecules were removed from the MST-1C-0.17P(600) surface. A shift of the C-O stretching band to lower wavenumbers (1020 and 1017 cm^{-1}) indicated that the adsorbed methanol species were activated at increased temperature, resulting in a weaken C-O bond. The three bands at 1160, 1078 and 1051 cm^{-1} should be related to the adsorbed methanol species I, II, and H, respectively. According to the pyrrole adsorption study, methanol adsorbed on MST-1C-0.17P(600) with species I corresponded to dissociated methanol bonded with oxygen atom of basic site types metal-oxygen ion pairs. In case of methanol adsorbed species II, relating to dissociated methanol bonded with oxygen atom of basic site types coordinatively unsaturated O^{2-}. Lastly, the species H should be attributed to the methanol adsorbed on weak acidic and/or weak basic sites by H-bonding. When the temperature was increased (spectrum (b), (c), (d) and (e)), species H is easily desorbed from the MST surface whereas species I and II retained on the active sites as seen from their intense bands. Therefore, the adsorbed species I and II should be involved with the transesterification since the temperatures, at which the reaction was performed, were ranged from 150 °C to 170 °C. However, the previous work found that the methoxy species II had too high stability on the metal oxide surface, and required a high temperature (>300°C) for desorption. Therefore, the methoxy species I and basic site types metal-oxygen ion pairs are of the importance for the transesterification over the MST-1C-0.17P(600) catalyst [68].

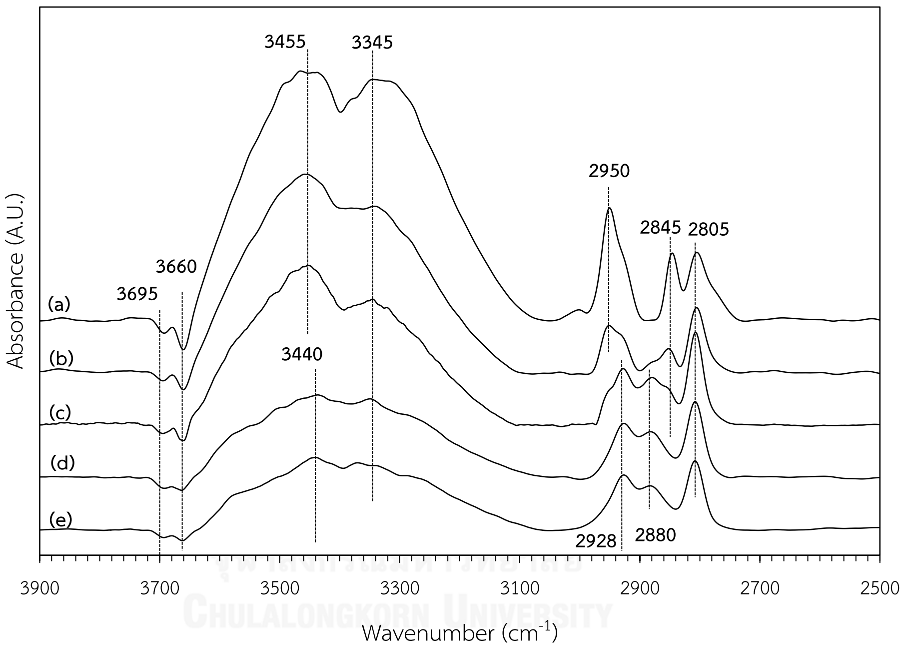

Figure 6.7 FTIR spectra in the O-H and C-H stretching regions of methanol adsorbed on MST-1C-0.17P(600) at 30 °C, followed by desorption at different temperatures: (a) 30 °C, (b) 65 °C, (c) 120 °C, (d) 150 °C and (e) 170 °C. The reported spectra were subtracted by the spectrum of MST-1C-0.17P(600) without methanol adsorption.

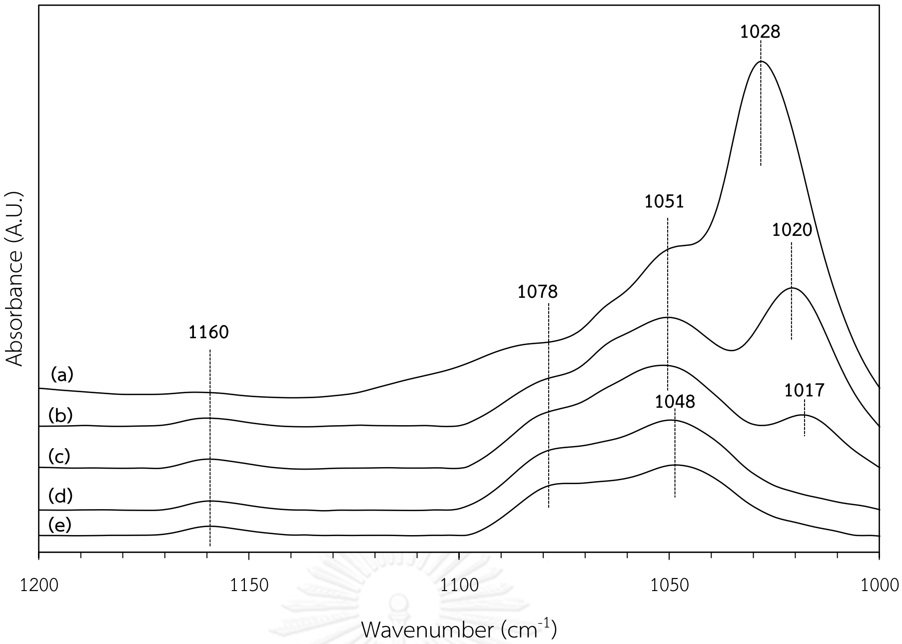

Figure 6.8 FTIR spectra in the C-O vibration region of methanol adsorbed on MST-1C-0.17P(600) at 30 °C, followed by desorption at different temperatures: (a) 30 °C, (b) 65 °C, (c) 120 °C, (d) 150 °C and (e) 170 °C. The reported spectra were subtracted by the spectrum of MST-1C-0.17P(600) without methanol adsorption.

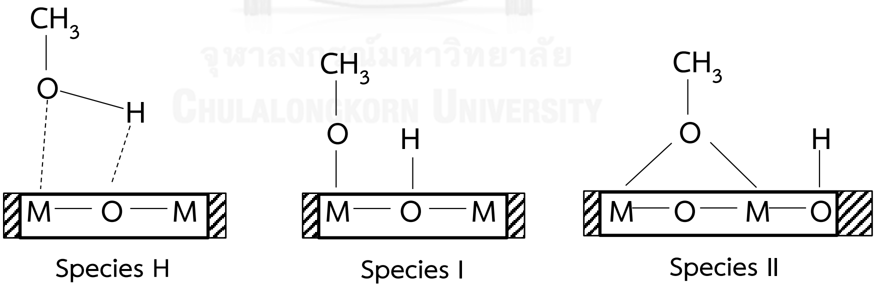

Figure 6.9 Adsorbed methanol species on metal oxide [68].

Table 6.4 Assignment of vibration bands observed from methanol adsorption on MST-1C-0.17P(600)

Wavenumber (cm^{-1})	**Assignment**
3695	O-H stretching (surface hydroxyl group of metal hydroxide)
3665	O-H stretching (surface hydroxyl group of metal hydroxide)
3445	O-H stretching (H-bonded on surface hydroxyl group)
3350	O-H stretching (H-bonded on surface hydroxyl group)
2950	C-H stretching of methyl group (asymmetric vibration)
2845	C-H stretching of methyl group (symmetric vibration)
2805	C-H stretching of methyl group (symmetric vibration)
1160	C-O vibration (species I)
1078	C-O vibration (species II)
1051	C-O vibration (species H)
1028	C-O vibration (free methanol)

6.2.2 Ethyl propionate adsorption

Ethyl propionate was chosen as a model triglyceride molecule because real triglyceride is too bulky and has a high boiling point. Figure 6.10 shows the FTIR spectra obtained between 3900 and 2800 cm^{-1}, corresponding to the stretching modes of O-H and C-H bonds. The observed bands in this region are summarized in Table 6.5. After the ester adsorption at 30 °C (spectrum (a)), the negative absorbance at 3660 cm^{-1} was attributed to the surface –OH groups on MST-1C-0.17P(600), which was perturbed by ethyl propionate molecules. The bands at 3455 and 3340 cm^{-1} were originated from H-bonding between the surface hydroxyl groups and ethyl propionate molecules. The bands at 2983, 2944 and 2890 cm^{-1} corresponded to the stretching vibrations of C-H bonds of methyl group in ethyl propionate [99]. When the desorption temperature was increased, these bands were decreased in their intensity. It should be attributed to desorption of weakly bonded ethyl propionate molecule from the active sites. Interestingly, a small band at 2922 cm^{-1} was observed at the temperature higher than 120 °C (spectrum (d) and (e)). The presence of this band suggested a structural change of ethyl propionate adsorbed on the active sites. Moreover, the nature of adsorbed species was confirmed by the spectra in the regions of C=O and O-C-O stretching modes, which can be used to explain the coordination modes occurring between the ester molecule and the active sites. According to the literature [100], there are three possible coordination modes of ester molecule adsorbed on metal oxides in form of carboxylate species, which are monodentate, bidentate chelating and bidentate bridging as shown in Figure 6.11.

Figure 6.11 shows the FTIR spectra in the C=O stretching region and the C-O, C-H vibration regions of ethyl propionate adsorbed on MST-1C-0.17P(600) at 30 °C (spectrum (a)), followed by desorption at different temperatures. The C=O stretching mode of free ester molecule was observed at 1714 cm^{-1} [99]. With increasing the desorption temperature, this band was decreased in this intensity and shifted to lower wavenumbers. The increased temperature also enhanced the formation of new bands at 1552 and 1430 cm^{-1}, corresponding to the O-C-O asymmetric stretching and symmetric stretching, respectively. Moreover, the bands between 1400 and 1200 cm^{-1}, corresponding to C-H and C-O vibration modes of ester molecule were decreased. The results suggested that the original ester molecule was changed. The possible configurations of the carboxylate adsorbed on the MST-1C-0.17P(600) surface depended on the properties of the active sites as follows.

(1) Formation of bidentate chelating carboxylate

(2) Formation of bidentate bridging carboxylate

The configurations of the carboxylate adsorbed on metal oxides were shown in Figure 6.12.

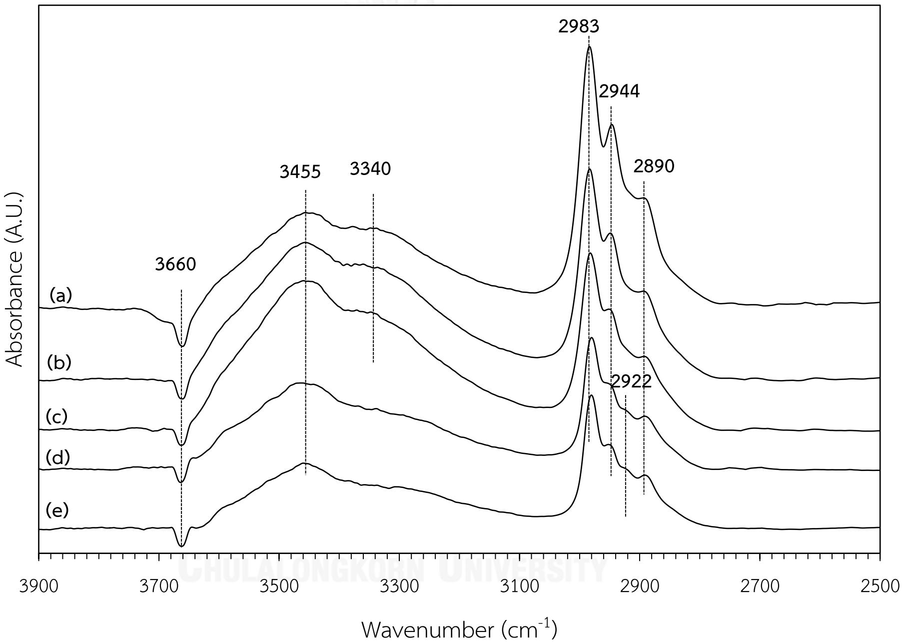

Figure 6.10 FTIR spectra at O-H and C-H stretching region of MST-1C-0.17P(600) after ethyl propionate adsorption at 30 °C followed by ethyl propionate desorption at different temperatures (a) 30 °C, (b) 65 °C, (c) 120 °C, (d) 150 °C and (e) 170 °C. The spectra was subtracted by the spectrum of MST-1C-0.17P(600) without ethyl propionate adsorption.

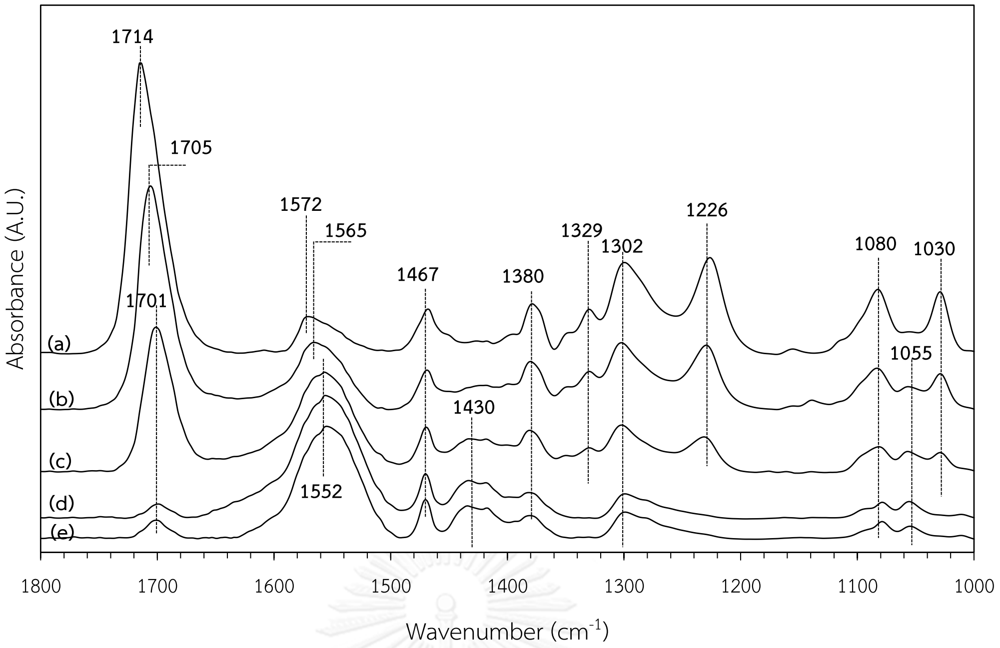

Figure 6.11 FTIR spectra at C=O stretching region and C-O, C-H vibration regions of MST-1C-0.17P(600) after ethyl propionate adsorption at 30 °C followed by ethyl propionate desorption at different temperatures (a) 30 °C, (b) 65 °C, (c) 120 °C, (d) 150 °C and (e) 170 °C. The spectra was subtracted by the spectrum of MST-1C-0.17P(600) without ethyl propionate adsorption.

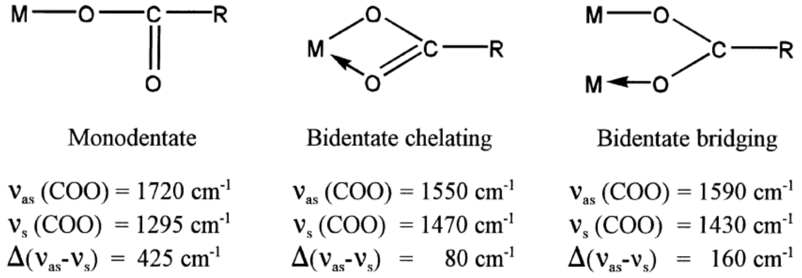

Figure 6.12 Different coordination modes occurring in metal carboxylates [100].

Table 6.5 Assignment of vibration bands observed from ethyl propionate adsorption on MST-1C-0.17P(600)

Wavenumber (cm^{-1})	Assignment	Wavenumber (cm^{-1})	Assignment
3660	O-H stretching (surface hydroxyl group of metal hydroxide)	1467	O-C-O stretching of metal carboxylate (symmetric vibration)
3455	O-H stretching (H-bonded on surface metal oxide)	1430	O-C-O stretching of metal carboxylate (symmetric vibration)
3340	O-H stretching (H-bonded on surface metal oxide)	1380	C-H bending of methyl group (symmetric vibration)
2983	C-H stretching of ester molecule (asymmetric vibration)	1329	C-H deformation of methyl group (symmetric vibration)
2944	C-H stretching of ester molecule (asymmetric vibration)	1302	C-H wagging of methylene
2890	C-H stretching of ester molecule (symmetric vibration)	1226	C-O stretching of ester molecule
1714–1701	C=O stretching of ester molecule	1080	C-H rocking of methyl group in ester molecule
1572	O-C-O stretching of metal carboxylate (asymmetric vibration)	1055	C-O stretching of ester molecule
1565	O-C-O stretching of metal carboxylate (asymmetric vibration)	1030	C-O stretching of ester molecule
1552	O-C-O stretching of metal carboxylate (asymmetric vibration)		

6.2.3 Methanol and ethyl propionate adsorption

To simulate the adsorption of methanol and ethyl propionate in accord with the transesterification procedure described in Chapter III, the MST-1C-0.17P(600) catalyst was first allowed to contact with methanol vapor at 30 °C, and then the ethyl propionate vapor was introduced onto the catalyst sample. Subsequently, the temperature was elevated under evacuation in order to the nature of active sites interacted by both reactant molecules.

Figure 6.13 shows the FTIR spectra obtained between 3900 and 2800 cm^{-1}, corresponding to the stretching modes of O-H and C-H bonds. The observed bands from this experiment are summarized in Table 6.6. After the methanol adsorption at 30 °C (spectrum (a)), the negative absorbance at 3660 cm^{-1} was attributed to the surface –OH groups on MST-1C-0.17P(600), which were perturbed by methanol molecules [71]. Two broad bands centered at 3450 and 3340 cm^{-1} indicated the presence of methanol molecules H-bonded to different active sites on the MST-1C-0.17P(600) surface [71]. However, the intensity of these two bands decreased with increasing the evacuation temperature (spectrum (c), (d), (e) and (f)). The results indicated that the corresponding adsorbed methanol species were easily desorbed when the temperature was elevated above boiling point of methanol. The bands at 2950, 2845 and 2805 cm^{-1} were ascribed to the stretching vibrations of C-H bonds of methanol (spectrum (a)) [98].

After introducing ethyl propionate into the IR cell at 30 °C (spectrum (b)), the intensity of bands at 2950 and 2845 cm^{-1} was decreased, and FTIR bands at 2985, 2945 and 2885 cm^{-1}, corresponding to the C-H stretching vibrations ethyl propionate were observed. It should be attributed to a substitution of the ethyl propionate molecules for the methanol weakly adsorbed on the MST-1C-0.17P(600) surface. However, the band at 2805 cm^{-1} remained intact, indicating that some adsorbed methanol species still retained on the active sites after introducing ethyl propionate. The ester molecules weakly interacted with the active sites were removed, as seen from decrease in the C-H stretching bands (2985, 2945 and 2885 cm^{-1}), when the temperature was increased (spectrum (b), (c), (d), (e) and (f)). Unlike the case of pure methanol adsorption, which revealed a retention of the band at 2805 cm^{-1} even at 170 °C, the presence of both methanol and ethyl propionate facilitated decreasing of this, started at 120 °C and almost disappeared at 170 °C. The results implied that the surface reaction between the adsorbed species occurred at temperature of >120 °C.

Figure 6.14 shows the FTIR spectra in the regions of C=O, C-O, C-H vibrations of methanol and ethyl propionate adsorbed on the MST-1C-0.17P(600) surface. For spectrum (a), the bands at 1050 and 1030 cm^{-1} corresponded to the C-O vibration mode of the adsorbed methanol species H [68] on the MST-1C-0.17P(600) surface and free methanol, respectively. After introducing the ethyl propionate vapor (spectrum (b)), the characteristic peaks of ester molecule were observed. The band of C=O stretching mode was found at 1710 cm^{-1}. This band was decreased and shifted to lower wavenumbers when the desorption temperature increased. Moreover, the bands at 1555 and 1435 cm^{-1}, corresponding to the O-C-O asymmetric stretching and symmetric stretching of ester group [100], respectively, became intense, and the bands between 1400 and 1200 cm^{-1}, corresponding to the C-H vibration of ester molecule [100] were decreased. The results obtained from this experiment were similar to those described in Section 6.2.2., suggesting the formation of adsorbed carboxylate species on the MST-1C-0.17P(600) surface.

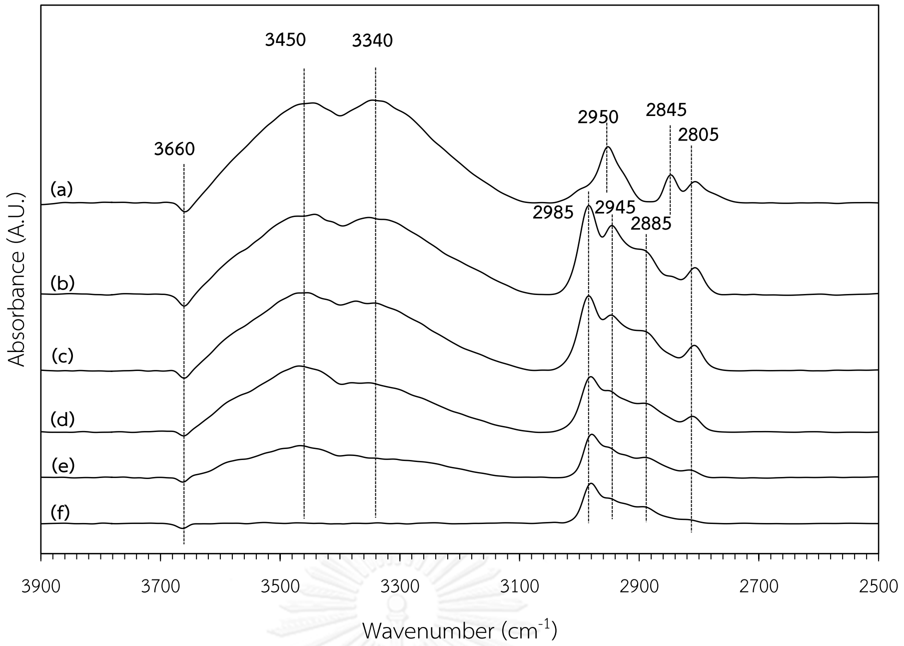

Figure 6.13 FTIR spectra in the O-H and C-H stretching regions of MST-1C-0.17P(600) after methanol adsorption at 30 °C: (a) and then ethyl propionate adsorption at 30 °C, followed by desorption at different temperatures: (b) 30 °C, (c) 65 °C, (d) 120 °C, (e) 150 °C and (f) 170 °C. The spectra was subtracted by the spectrum of MST-1C-0.17P(600) without methanol and ethyl propionate adsorption.

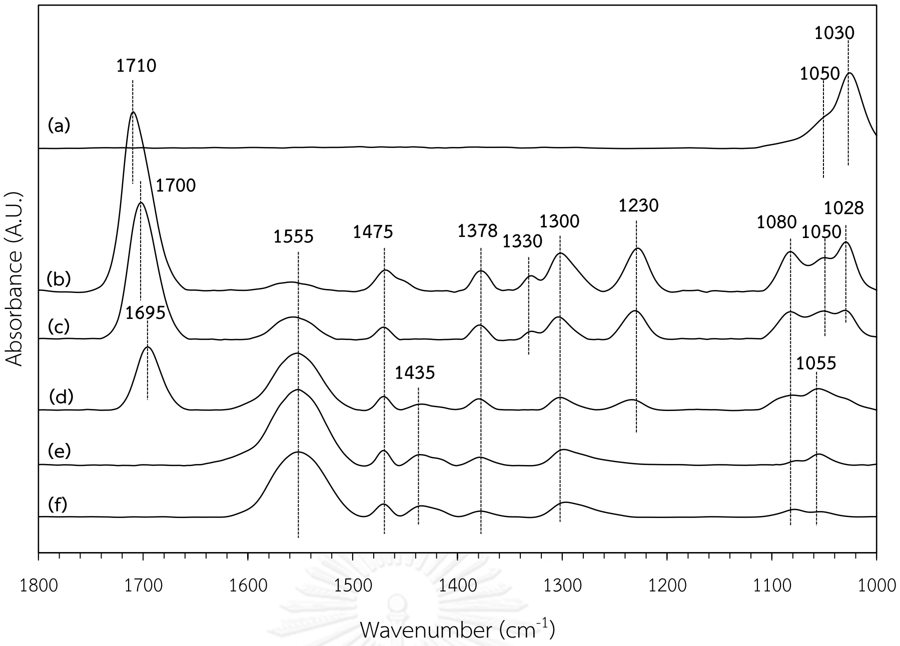

Figure 6.14 FTIR spectra in the C=O stretching region and C-O, C-H vibration regions of MST-1C-0.17P(600) after methanol adsorption at 30 °C: (a) and then ethyl propionate adsorption at 30 °C, followed by desorption at different temperatures: (b) 30 °C, (c) 65 °C, (d) 120 °C, (e) 150 °C and (f) 170 °C. The spectra was subtracted by the spectrum of MST-1C-0.17P(600) without methanol and ethyl propionate adsorption.

Table 6.6 Assignment of vibration bands observed from methanol and ethyl propionate adsorption on MST-1C-0.17P(600)

Wavenumber (cm^{-1})	Assignment	Wavenumber (cm^{-1})	Assignment
3660	O-H stretching (surface hydroxyl group of metal hydroxide)	1475	O-C-O stretching of metal carboxylate (symmetric vibration)
3450	O-H stretching (H-bonded on surface metal oxide)	1435	O-C-O stretching of metal carboxylate (symmetric vibration)
3340	O-H stretching (H-bonded on surface metal oxide)	1378	CH bending of methyl group (symmetric vibration)
2985	C-H stretching of methyl group in ester molecule (asymmetric vibration)	1330	CH deformation of methyl group (symmetric vibration)
2950	C-H stretching of methyl group in methanol molecule (asymmetric vibration)	1300	CH wagging of methylene
2885	C-H stretching of methyl group in ester molecule (symmetric vibration)	1230	C-O stretching of ester molecule
2845	C-H stretching of methyl group in methanol molecule (symmetric vibration)	1080	CH rocking of methyl group in ester molecule
2805	C-H stretching of methyl group (symmetric vibration)	1050	C-O vibration of methanol and CO stretching of ester molecule
1710–1695	C=O stretching of ester molecule	1030	C-O vibration of gaseous methanol and CO stretching of ester molecule
1555	O-C-O stretching of metal carboxylate (asymmetric vibration)		

CHAPTER VII

Conclusions and recommendations

7.1 Conclusions

Mesostructured Sr and Ti mixed oxides (MST) can be fabricated via the neutral-template self-assembly sol-gel combustion method using the commercial triblock copolymer (Pluronic P123) as the structure-directing agent. The addition of citric acid enhanced not only the purity and crystallinity of $SrTiO_3$ but also promoted the mesoporous assembled structure. The route for the mesostructure generation possibly occurred via the combination soft and hard template mechanism in which $SrTiO_3$ was crystallized around the *in situ* carbon residue produced by carbonization of templating molecules during the combustion of metal citrates. Therefore, the presence of both tri-block copolymer and citric acid is necessary to obtain the mesostructured Sr and Ti mixed oxides.

MST with good structural and textural properties could be achieved by carefully adjusting the synthesis composition. The structural and textural properties of the MST enhanced by increasing of citric acid amount, but the excessive molar ratio of citric acid: total metals were detrimental to the mesophase in MST materials. The BET surface area of MST attained increased with increasing amount of Pluronic P123 added in the synthesis mixture. However, crystallinity of MST deceased when increased the adding Pluronic P123 higher than 0.17 mmol. The crystallinity of MST increased with increasing calcination temperature, but its textural properties of MST attained to be decreased when MST calcined at temperature higher than 600 °C. Therefore, the optimal condition for preparing the MST with good structural and textural properties was molar ratio of citric acid: total metals at 1: 1, amount of Pluronic P123 at 0.172 mmol and calcination temperature at 600 °C.

Two MST samples prepared under different conditions (MST-0C-0.17P(600) and MST-1C-0.17P(600)) were applied as catalyst in transesterification of palm kernel oil (PKO) with methanol. Although the MST-0C-0.17P(600) had higher basicity than MST-1C-0.17P(600), the chemical stability of MST-1C-0.17P(600) was superior to that of MST-0C-0.17P(600). To attain the FAME yield of 99.8 wt%, the transesterification of palm kernel oil with methanol over MST-0C-0.17P(600) was performed at 150 °C, whereas a higher temperature (170 °C) was required for the reaction catalysed by MST-1C-0.17P(600). Other parameters that were suitable for achieving the highest FAME yield were the same for both MST catalysts (molar ratio of methanol: oil = 20: 1, catalyst loading = 10 wt% and reaction time = 3 h). Unlike the MST-1C-0.17P(600), the MST-0C-0.17P(600) exhibited a significant homogeneous catalysis contributed by leached metal species and a severe loss of basicity and catalytic activity after the first use in the reaction. The MST-1C-0.17P(600) was more tolerant towards the deactivation by free fatty acid (FFA) and water contained in the feedstock. This work emphasised the advantages of highly crystalline Sr and Ti mixed oxides as a heterogeneous base catalyst in the transesterification of vegetable oils with methanol to the corresponding FAME. The value of E_a from Arrhenius plot was found to be 57.1 kJ mol^{-1}, indicating the transesterification of PKO with methanol over MST-1C-0.17P(600) is a chemically controlled reaction.

The adsorption of pyridine molecule demonstrated that MST-1C-0.17P(600) surface possessed weak to moderate Lewis acid sites from Sr^{2+} and Ti^{4+}. In case of basicity, MST-1C-0.17P(600) had 4 types of basic sites with different basic strength, including coordinatively unsaturated O^{2-}, metal-oxygen ion pairs, monodentate surface hydroxide and bidentate surface hydroxide. The results from methanol adsorption showed that the methanol molecules adsorbed on MST-1C-0.17P(600) with species I, species II and species H. However, methanol adsorbed on MST-1C-0.17P(600) with species I should be involved in transesterification. The results from ethyl propionate as model triglyceride adsorption showed that the originate ester molecule was changed when ethyl propionate adsorbed on the MST-1C-0.17P(600) surface with increasing desorption temperature. The adsorbed ester configurations on the MST-1C-0.17P(600) surface depended on the acid and basic properties of the active sites. Finally, the results from the adsorption of both methanol and ethyl propionate molecules, followed by the FTIR spectroscopic study provided the possible reaction mechanism for the transesterification over the MST-1C-0.17P(600) catalyst as shown in Figure 6.15.

7.2 Recommendations for future works

Although the obtained MST-1C-0.17P(600) exhibited high purity, good structural and textural properties, it has a limitation in term of mesoporous ordering because of weak interaction between inorganic species and poly (ethylene oxide) as hydrophilic part in Pluronic P123. Therefore, the use of other structure-directing agents consisted of high content of polar part, such as oligomer alkyl poly(ethylene oxide) (Brij$^{®}$) and sorbitan ester (Tween$^{®}$), leading to enhance the interaction between hydrophilic domains in template molecule and metal citrate complexes. In addition, MST catalysts exhibited good catalytic activity in transesterification but the reusability limited the use of them for a continuous FAME production. Finally, the amount of basic site on MST-1C-0.17P(600) could not be determined by using pyrrole as probe molecule. Hence, the amount of basic site should be examined by using other acidic probe molecules, such as, chloroform and CO_2.

REFERENCES

1. Refaat, A. A., Biodiesel production using solid metal oxide catalysts. *International Journal of Environmental Science & Technology* **2010,** *8*, 203–221.

2. Leung, D. Y. C.; Wu, X.; Leung, M. K. H., A review on biodiesel production using catalyzed transesterification. *Applied Energy* **2010,** *87*, 1083–1095.

3. Patil, P. D.; Deng, S., Transesterification of Camelina Sativa Oil Using Heterogeneous Metal Oxide Catalysts. *Energy & Fuels* **2009,** *23*, 4619–4624.

4. Sharma, Y. C.; Singh, B.; Korstad, J., Latest developments on application of heterogenous basic catalysts for an efficient and eco friendly synthesis of biodiesel: A review. *Fuel* **2011,** *90*, 1309–1324.

5. Xu, C.; Enache, D. I.; Lloyd, R.; Knight, D. W.; Bartley, J. K.; Hutchings, G. J., MgO Catalysed Triglyceride Transesterification for Biodiesel Synthesis. *Catalysis Letters* **2010,** *138*, 1–7.

6. Liu, X.; He, H.; Wang, Y.; Zhu, S.; Piao, X., Transesterification of soybean oil to biodiesel using CaO as a solid base catalyst. *Fuel* **2008,** *87*, 216–221.

7. Liu, X.; He, H.; Wang, Y.; Zhu, S., Transesterification of soybean oil to biodiesel using SrO as a solid base catalyst. *Catalysis Communications* **2007,** *8*, 1107–1111.

8. Dias, A. P. S.; Bernardo, J.; Felizardo, P.; Correia, M. J. N., Biodiesel production by soybean oil methanolysis over SrO/MgO catalysts. *Fuel Processing Technology* **2012,** *102*, 146–155.

9. Xie, W.; Yang, Z., Ba–ZnO catalysts for soybean oil transesterification. *Catalysis Letters* **2007,** *117*, 159–165.

10. Albuquerque, M. C. G.; Jiménez-Urbistondo, I.; Santamaría-González, J.; Mérida-Robles, J. M.; Moreno-Tost, R.; Rodríguez-Castellón, E.; Jiménez-López, A.; Azevedo, D. C. S.; Cavalcante Jr, C. L.; Maireles-Torres, P., CaO supported on mesoporous silicas as basic catalysts for transesterification reactions. *Applied Catalysis A: General* **2008,** *334*, 35–43.

11. Wen, Z.; Yu, X.; Tu, S. T.; Yan, J.; Dahlquist, E., Biodiesel production from waste cooking oil catalyzed by TiO_2-MgO mixed oxides. *Bioresource technology* **2010,** *101*, 9570–9576.

12. Wang, J.; Yin, S.; Sato, T., Synthesis and characterization of fibrous $SrTiO_3$ particles. *Materials Science and Engineering: B* **2006,** *131*, 248–251.

13. Li, X.; Zhao, H.; Zhou, X.; Xu, N.; Xie, Z.; Chen, N., Electrical conductivity and structural stability of La-doped $SrTiO_3$ with A-site deficiency as anode materials for solid oxide fuel cells. *International Journal of Hydrogen Energy* **2010,** *35*, 7913–7918.

14. Liu, H.; Sun, X.; Zhao, Q.; Xiao, J.; Ouyang, S., The syntheses and microstructures of tabular $SrTiO_3$ crystal. *Solid-State Electronics* **2003,** *47*, 2295–2298.

15. Rashtizadeh, E.; Farzaneh, F., Transesterification of soybean oil catalyzed by Sr–Ti mixed oxides nanocomposite. *Journal of the Taiwan Institute of Chemical Engineers* **2013,** *44*, 917–923.

16. Ishikawa, H.; Oohira, K.; Nakajima, T.; Akiyama, T., Combustion synthesis of $SrTiO_3$ using different raw materials. *Journal of Alloys and Compounds* **2008,** *454*, 384–388.

17. Liu, S.; Xiu, Z.; Liu, J. a.; Xu, F.; Yu, W.; Yu, J.; Feng, G., Combustion synthesis and characterization of perovskite $SrTiO_3$ nanopowders. *Journal of Alloys and Compounds* **2008,** *457*, L12–L14.

18. Nuntang, S.; Poompradub, S.; Butnark, S.; Yokoi, T.; Tatsumi, T.; Ngamcharussrivichai, C., Novel mesoporous composites based on natural rubber and hexagonal mesoporous silica: Synthesis and characterization. *Materials Chemistry and Physics* **2014,** *143*, 1199–1208.

19. She, X.; Chen, L.; Velleman, L.; Li, C.; Zhu, H.; He, C.; Wang, T.; Shigdar, S.; Duan, W.; Kong, L., Fabrication of high specificity hollow mesoporous silica nanoparticles assisted by Eudragit for targeted drug delivery. *Journal of colloid and interface science* **2015,** *445*, 151–160.

20. Stucky, G. D.; Yang, P.; Zhao, D.; Margolese, D. I.; Chmelka, B. F., Generalized syntheses of large-poremesoporous metal oxides with semicrystalline frameworks. *Nature* **1998,** *396*, 152–155.

21. Strontium Titanate ($SrTiO_3$) - Properties and Applications. http://www.azom.com/article.aspx?ArticleID=2362 (accessed 13 May).

22. Shi, J.; Guo, L., ABO_3-based photocatalysts for water splitting. *Progress in Natural Science: Materials International* **2012,** *22*, 592–615.

23. Ishikawa, Y. Physicochemical properties of $SrTiO_3$. http://www.chem.kit.ac.jp/lab/apspishi.html (accessed 15 May).

24. de Groot, F. M. F.; Grioni, M.; Fuggle, J. C.; Ghijsen, J.; Sawatzky, G. A.; Petersen, H., Oxygen 1s X-ray-absorption edges of transition-metal oxides. *Physical Review B* **1989,** *40*, 5715–5723.

25. Kim, K. H.; Park, J. K.; Kim, C. H.; Park, H. D.; Chang, H.; Choi, S. Y., Synthesis of $SrTiO_3$: Pr,Al by ultrasonic spray pyrolysis. *Ceramics International* **2002,** *28*, 29–36.

26. Zorel, H. E.; Guinesi, L. S.; Ribeiro, C. A.; Crespi, M. S., $SrTiO_3$ preparation through coprecipitation methods. *Materials Letters* **2000,** *42*, 16–20.

27. Pontes, F. M.; Lee, E. J. H.; Leite, E. R.; Longo, E.; Varela, J. A., High dielectric constant of $SrTiO_3$ thin films prepared by chemical process. *Journal of Materials Science* **2000,** *35*, 4783–4787.

28. Sulaeman, U.; Yin, S.; Sato, T., Solvothermal synthesis and photocatalytic properties of nitrogen-doped $SrTiO_3$ nanoparticles. *Journal of Nanomaterials* **2010,** *2010*, 1–6.

29. Klaytae, T.; Panthong , P.; Thountom, S., Preparation of nanocrystalline strontium titanate ($SrTiO_3$) powder by sol-gel combustion method. *Academic Journals* **2013,** *8*, 32–38.

30. Corma, A., From microporous to mesoporous molecular sieve materials and their use in catalysis. *Chemical Reviews* **1997,** *97*, 2373–2420.

31. Perego, C.; Millini, R., Porous materials in catalysis: challenges for mesoporous materials. *Chemical Society reviews* **2013,** *42* (9), 3956–3976.

32. Wagner, T.; Haffer, S.; Weinberger, C.; Klaus, D.; Tiemann, M., Mesoporous materials as gas sensors. *Chemical Society reviews* **2013,** *42*, 4036–4053.

33. Linares, N.; Silvestre-Albero, A. M.; Serrano, E.; Silvestre-Albero, J.; Garcia-Martinez, J., Mesoporous materials for clean energy technologies. *Chemical Society reviews* **2014,** *43*, 7681–7717.

34. Sing, K. S. W.; Everett, D. H.; Haul, R. A. W.; Moscou, L.; Pierotti, R. A.; Rouquerol, J.; Siemieniewska, T., Reporting physisorption data for gas/solid systems. *Pure and Applied Chemistry* **2008,** *57*, 603–619.

35. Malgras, V.; Ataee-Esfahani, H.; Wang, H.; Jiang, B.; Li, C.; Wu, K. C. W.; Kim, J. H.; Yamauchi, Y., Nanoarchitectures for mesoporous metals. *Advanced Materials* **2016,** *28*, 993–1010.

36. Kresge, C. T.; Leonowicz, M. E.; Roth, W. J.; Vartuli, J. C.; Beck, J. S., Ordered mesoporous molecular sieves synthesized by a liquid-crystal template mechanism. *Nature* **1992,** *359*, 710–712.

37. Beck, J. S.; Vartuli, J. C.; Roth, W. J.; Leonowicz, M. E.; Kresge, C. T.; Schmitt, K. D.; Chu, C. T. W.; Olson, D. H.; Sheppard, E. W.; McCullen, S. B.; Higgins, J. B.; Schlenker, J. L., A new family of mesoporous molecular sieves prepared with liquid crystal templates. *Journal of the American Chemical Society* **1992,** *114*, 10834–10843.

38. Zhao, D., Triblock copolymer syntheses of mesoporous silica with periodic 50 to 300 angstrom pores. *Science* **1998,** *279*, 548–552.

39. Kruk, M.; Jaroniec, M.; Ko, C. H.; Ryoo, R., Characterization of the porous structure of SBA-15. *Chemistry of Materials* **2000,** *12*, 1961–1968.

40. Emons, T. T.; Li, J.; Nazar, L. F., Synthesis and characterization of mesoporous Indium Tin oxide possessing an electronically conductive framework. *Journal of the American Chemical Society* **2002,** *124*, 8516–8517.

41. Vinu, A.; Ariga, K.; Mori, T.; Nakanishi, T.; Hishita, S.; Golberg, D.; Bando, Y., Preparation and characterization of well-ordered hexagonal mesoporous carbon nitride. *Advanced Materials* **2005,** *17*, 1648–1652.

42. Pal, N.; Bhaumik, A., Soft templating strategies for the synthesis of mesoporous materials: inorganic, organic-inorganic hybrid and purely organic solids. *Advances in colloid and interface science* **2013,** *189–190*, 21–41.

43. Deng, Y.; Wei, J.; Sun, Z.; Zhao, D., Large-pore ordered mesoporous materials templated from non-Pluronic amphiphilic block copolymers. *Chemical Society reviews* **2013,** *42*, 4054–4070.

44. Wan, Y.; Shi, Y.; Zhao, D., Designed synthesis of mesoporous solids via nonionic-surfactant-templating approach. *Chemical communications* **2007**, 897–926.

45. Gu, D.; Schüth, F., Synthesis of non-siliceous mesoporous oxides. *Chemical Society reviews* **2014,** *43*, 313–344.

46. Yang, P.; Zhao, D.; Margolese, D. I.; Chmelka, B. F.; Stucky, G. D., Block copolymer templating syntheses of mesoporous metal oxides with large ordering lengths and semicrystalline framework. *Chemistry of Materials* **1999,** *11*, 2813–2826.

47. Grosso, D.; Boissière, C.; Smarsly, B.; Brezesinski, T.; Pinna, N.; Albouy, P. A.; Amenitsch, H.; Antonietti, M.; Sanchez, C., Periodically ordered nanoscale islands and mesoporous films composed of nanocrystalline multimetallic oxides. *Nature Materials* **2004,** *3*, 787–792.

48. Brezesinski, T.; Smarsly, B.; Iimura, K.-i.; Grosso, D.; Boissière, C.; Amenitsch, H.; Antonietti, M.; Sanchez, C., Self-assembly and crystallization behavior of mesoporous, crystalline HfO_2 thin films: A model system for the generation of mesostructured transition-metal oxides. *Small* **2005,** *1*, 889–898.

49. Bartlett, P. N.; Baumberg, J. J.; Birkin, P. R.; Ghanem, M. A.; Netti, M. C., Highly ordered macroporous gold and platinum films formed by electrochemical deposition through templates assembled from submicron diameter monodisperse polystyrene spheres. *Chemistry of Materials* **2002,** *14*, 2199–2208.

50. Zhu, K.; Yue, B.; Zhou, W.; He, H., Preparation of three-dimensional chromium oxide porous single crystals templated by SBA-15. *Chemical communications* **2003**, 98–99.

51. Zhu, K.; He, H.; Xie, S.; Zhang, X.; Zhou, W.; Jin, S.; Yue, B., Crystalline WO_3 nanowires synthesized by templating method. *Chemical Physics Letters* **2003,** *377*, 317–321.

52. Tian, B.; Liu, X.; Yang, H.; Xie, S.; Yu, C.; Tu, B.; Zhao, D., General synthesis of ordered crystallized metal oxide nanoarrays replicated by microwave-digested mesoporous silica. *Advanced Materials* **2003,** *15*, 1370–1374.

53. Roggenbuck, J.; Koch, G.; Tiemann, M., Synthesis of mesoporous magnesium oxide by CMK-3 carbon structure replication. *Chemistry of Materials* **2006,** *18*, 4151–4156.

54. Jiao, F.; Harrison, A.; Hill, A. H.; Bruce, P. G., Mesoporous Mn_2O_3 and Mn_3O_4 with crystalline walls. *Advanced Materials* **2007,** *19*, 4063–4066.

55. Jiao, F.; Jumas, J. C.; Womes, M.; Chadwick, A. V.; Harrison, A.; Bruce, P. G., Synthesis of ordered mesoporous Fe_3O_4 and gamma-Fe_2O_3 with crystalline walls using post-template reduction/oxidation. *Journal of the American Chemical Society* **2006,** *128*, 12905–12909.

56. Kondo, J. N.; Domen, K., Crystallization of mesoporous metal oxides. *Chemistry of Materials* **2008,** *20*, 835–847.

57. Lee, J.; Orilall, M. C.; Warren, S. C.; Kamperman, M.; DiSalvo, F. J.; Wiesner, U., Direct access to thermally stable and highly crystalline mesoporous transition-metal oxides with uniform pores. *Nature Materials* **2008,** *7*, 222–228.

58. Ma, F.; Hanna, M. A., Biodiesel production: a review. *Bioresource technology* **1999,** *70*, 1–15.

59. Salimon, J.; Salih, N.; Yousif, E., Industrial development and applications of plant oils and their biobased oleochemicals. *Arabian Journal of Chemistry* **2012,** *5*, 135–145.

60. Maag, H., Fatty acid derivatives: Important surfactants for household, cosmetic and industrial purposes. *Journal of the American Oil Chemists' Society* **1984,** *61*, 259–267.

61. Vyas, A. P.; Verma, J. L.; Subrahmanyam, N., A review on FAME production processes. *Fuel* **2010,** *89*, 1–9.

62. Joshi, R. M.; Pegg, M. J., Flow properties of biodiesel fuel blends at low temperatures. *Fuel* **2007,** *86*, 143–151.

63. Ulf, S.; Ricardo, S.; Rogério, M. V., Transesterification of vegetable oils: A review. *Journal of the Brazilian Chemical Society* **1998,** *9* (3), 199–210.

64. Freedman, B.; Butterfield, R. O.; Pryde, E. H., Transesterification kinetics of soybean oil *Journal of the American Oil Chemists' Society* **1986,** *63*, 1375–1380.

65. Zou, F.; Jiang, Z.; Qin, X.; Zhao, Y.; Jiang, L.; Zhi, J.; Xiao, T.; Edwards, P. P., Template-free synthesis of mesoporous N-doped $SrTiO_3$ perovskite with high visible-light-driven photocatalytic activity. *Chemical communications* **2012,** *48*, 8514-6.

66. Puangpetch, T.; Sreethawong, T.; Yoshikawa, S.; Chavadej, S., Synthesis and photocatalytic activity in methyl orange degradation of mesoporous-assembled $SrTiO_3$ nanocrystals prepared by sol–gel method with the aid of structure-directing surfactant. *Journal of Molecular Catalysis A: Chemical* **2008,** *287*, 70-79.

67. Rabuffetti, F. A.; Stair, P. C.; Poeppelmeier, K. R., Synthesis-dependent surface acidity and structure of $SrTiO_3$ nanoparticles. *The Journal of Physical Chemistry C* **2010,** *114*, 11056-11067.

68. Navajas, A.; Arzamendi, G.; Romero-Sarria, F.; Centeno, M. A.; Odriozola, J. A.; Gandía, L. M., DRIFTS study of methanol adsorption on Mg–Al hydrotalcite catalysts for the transesterification of vegetable oils. *Catalysis Communications* **2012,** *17*, 189-193.

69. Kaur, N.; Ali, A., One-pot transesterification and esterification of waste cooking oil via ethanolysis using Sr:Zr mixed oxide as solid catalyst. *RSC Advances* **2014,** *4*, 43671–43681.

70. Topaloglu Yazıcı, D.; Bilgiç, C., Determining the surface acidic properties of solid catalysts by amine titration using Hammett indicators and FTIR-pyridine adsorption methods. *Surface and Interface Analysis* **2010,** *42*, 959–962.

71. Barzetti, T.; Selli, E.; Moscotti, D.; Forni, L., Pyridine and ammonia as probes for FTIR analysis of solid acid catalysts. *Journal of the Chemical Society, Faraday Transactions* **1996,** *92*, 1401–1407.

72. Binet, C.; Jadi, A.; Lamotte, J.; Lavalley, J. C., Use of pyrrole as an IR spectroscopic molecular probe in a surface basicity study of metal oxides. *Journal of the Chemical Society, Faraday Transactions* **1996,** *92*, 123–129.

73. Yaakob, Z.; Mohammad, M.; Alherbawi, M.; Alam, Z.; Sopian, K., Overview of the production of biodiesel from Waste cooking oil. *Renewable and Sustainable Energy Reviews* **2013,** *18*, 184–193.

74. Atadashi, I. M.; Aroua, M. K.; Abdul Aziz, A. R.; Sulaiman, N. M. N., The effects of water on biodiesel production and refining technologies: A review. *Renewable and Sustainable Energy Reviews* **2012,** *16*, 3456–3470.

75. Guo, L.; Ida, S.; Hagiwara, H.; Daio, T.; Ishihara, T., Direct soft-templating route to crystalline mesoporous transition-metal oxides. *Colloids and Surfaces A: Physicochemical and Engineering Aspects* **2014,** *451*, 136–143.

76. Mali, A.; Ataie, A., Influence of the metal nitrates to citric acid molar ratio on the combustion process and phase constitution of barium hexaferrite particles prepared by sol–gel combustion method. *Ceramics International* **2004,** *30*, 1979–1983.

77. Dong, W.; Brooks, S. C., Determination of the formation constants of ternary complexes of uranyl and carbonate with alkaline earth metals (Mg^{2+}, Ca^{2+}, Sr^{2+}, and Ba^{2+}) using anion exchange method. *Environmental Science & Technology* **2006,** *40*, 4689–4695.

78. Li, Y.; Xue, L.; Fan, L.; Yan, Y., The effect of citric acid to metal nitrates molar ratio on sol–gel combustion synthesis of nanocrystalline $LaMnO_3$ powders. *Journal of Alloys and Compounds* **2009,** *478*, 493–497.

79. Monica, A.; Juan, E. F.; Sylvie, D. C., Characterization of the porous structure of chilen volvanic soils by nitrogen adsorption and mercury porosimetry *Journal of the Chilean Chemical Society* **2004,** *49*, 313–318.

80. Yang, B.; Guo, C.; Chen, S.; Ma, J.; Wang, J.; Liang, X.; Zheng, L.; Liu, H., Effect of acid on the aggregation of poly(ethylene xide)-poly(propylene oxide)-poly(ethylene oxide) block copolymers. *The Journal of Physical Chemistry B* **2006,** *110*, 23068–23074.

81. Biswas, M.; Ojha, P. K.; Prasad, C. D.; Gokhale, N. M.; Sharma, S. C., Synthesis of fluorite-type nanopowders by citrate-nitrate auto-combustion process: A systematic approach. *Materials Sciences and Applications* **2012,** *3*, 110–115.

82. Yin, H.; Wada, Y.; Kitamura, T.; Sumida, T.; Hasegawa, Y.; Yanagida, S., Novel synthesis of phase-pure nano-particulate anatase and rutile TiO_2 using $TiCl_4$ aqueous solutions. *Journal of Materials Chemistry* **2002,** *12*, 378–383.

83. Bastakoti, B. P.; Ishihara, S.; Leo, S. Y.; Ariga, K.; Wu, K. C.; Yamauchi, Y., Polymeric micelle assembly for preparation of large-sized mesoporous metal oxides with various compositions. *Langmuir : the ACS journal of surfaces and colloids* **2014,** *30*, 651–659.

84. Lertpanyapornchai, B.; Yokoi, T.; Ngamcharussrivichai, C., Citric acid as complexing agent in synthesis of mesoporous strontium titanate via neutral-templated self-assembly sol–gel combustion method. *Microporous and Mesoporous Materials* **2016,** *226*, 505–509.

85. Li, B.; Zhao, J.; Liu, J.; Shen, X.; Mo, S.; Tong, H., Bio-templated synthesis of hierarchically ordered macro-mesoporous anatase titanium dioxide flakes with high photocatalytic activity. *RSC Advances* **2015,** *5*, 15572–15578.

86. Mirzaeian, M.; Hall, P. J., The control of porosity at nano scale in resorcinol formaldehyde carbon aerogels. *Journal of Materials Science* **2009,** *44*, 2705–2713.

87. Pisarello, M. L.; Querini, C. A., Catalyst consumption during one and two steps transesterification of crude soybean oils. *Chemical Engineering Journal* **2013,** *234*, 276–283.

88. Hsieh, L.-S.; Kumar, U.; Wu, J. C. S., Continuous production of biodiesel in a packed-bed reactor using shell–core structural $Ca(C_3H_7O_3)_2/CaCO_3$ catalyst. *Chemical Engineering Journal* **2010,** *158*, 250–256.

89. Li, K.-T.; Wang, C.-K.; Wang, I.; Wang, C.-M., Esterification of lactic acid over TiO_2–ZrO_2 catalysts. *Applied Catalysis A: General* **2011,** *392*, 180–183.

90. Kouzu, M.; Kasuno, T.; Tajika, M.; Sugimoto, Y.; Yamanaka, S.; Hidaka, J., Calcium oxide as a solid base catalyst for transesterification of soybean oil and its application to biodiesel production. *Fuel* **2008,** *87*, 2798–2806.

91. Carvalho, L. M. G. d.; Abreu, W. C. d.; Silva, M. d. G. d. O. e.; Lima, J. R. d. O.; Oliveira, J. E. d.; Matos, J. M. E. d.; Moura, C. V. R. d.; Moura, E. M. d., Heterogeneous catalysis afford biodiesel of babassu, castor oil and blends. *Journal of the Brazilian Chemical Society* **2013,** *24*, 550–557.

92. Noureddini, H.; Zhu, D., Kinetics of transesterification of soybean oil. *Journal of the American Oil Chemists' Society* **1997,** *74*, 1457–1463.

93. Kaur, N.; Ali, A., Kinetics and reusability of Zr/CaO as heterogeneous catalyst for the ethanolysis and methanolysis of Jatropha crucas oil. *Fuel Processing Technology* **2014,** *119*, 173–184.

94. Baraton, M.-I., Nano-TiO_2 for solar cells and photocatalytic water splitting: scientific and technological challenges for commercialization. *The Open Nanoscience Journal* **2011,** *5*, 64–77.

95. Zaki, M. I.; Hasan, M. A.; Al-Sagheer, F. A.; Pasupulety, L., In situ FTIR spectra of pyridine adsorbed on SiO_2–Al_2O_3, TiO_2, ZrO_2 and CeO_2: general considerations for the identification of acid sites on surfaces of finely divided metal oxides. *Colloids and Surfaces A: Physicochemical and Engineering Aspects* **2001,** *190*, 261–274.

96. Tamura, M.; Shimizu, K.-i.; Satsuma, A., Comprehensive IR study on acid/base properties of metal oxides. *Applied Catalysis A: General* **2012,** *433–434*, 135–145.

97. Scokart, P. O.; Rouxhet, P. G., Characterization of the basicity of oxides through the infrared study of pyrrole adsorption. *Journal of the Chemical Society, Faraday Transactions 1: Physical Chemistry in Condensed Phases* **1980,** *76*, 1476–1489.

98. López Granados, M.; Alba-Rubio, A. C.; Vila, F.; Martín Alonso, D.; Mariscal, R., Surface chemical promotion of Ca oxide catalysts in biodiesel production reaction by the addition of monoglycerides, diglycerides and glycerol. *Journal of Catalysis* **2010,** *276*, 229–236.

99. Dutta, B.; Tanaka, T.; Banerjee, A.; Chowdhury, J., Conformational preferences of ethyl propionate molecule: Raman, temperature dependent FTIR spectroscopic study aided by ab initio quantum chemical and Car-Parrinello molecular dynamics simulation studies. *The journal of physical chemistry. A* **2013,** *117*, 4838–4350.

100. Urlaub, R.; Posset, U.; Thull, R., FT-IR spectroscopic investigations on sol-gel-derived coatings from acid-modified titanium alkoxides. *Journal of Non-Crystalline Solids* **2000,** *265*, 276–284.

APPENDIX

APPENDIX A

XRD patters of as-synthesized MST

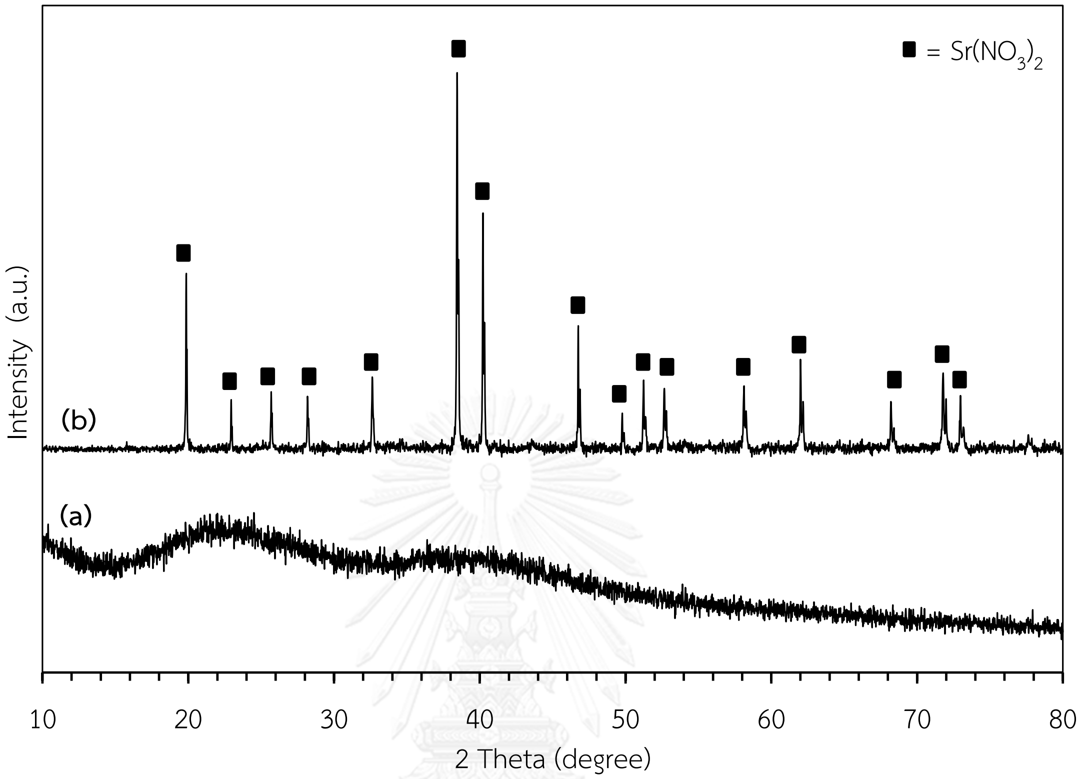

Figure A1 XRD patterns of (a) MST-1C-0.17P(as-syn), and (b) MST-0C-0.17P(as-syn)

APPENDIX B

Calculation of FAME yield and normalized composition of FAME product

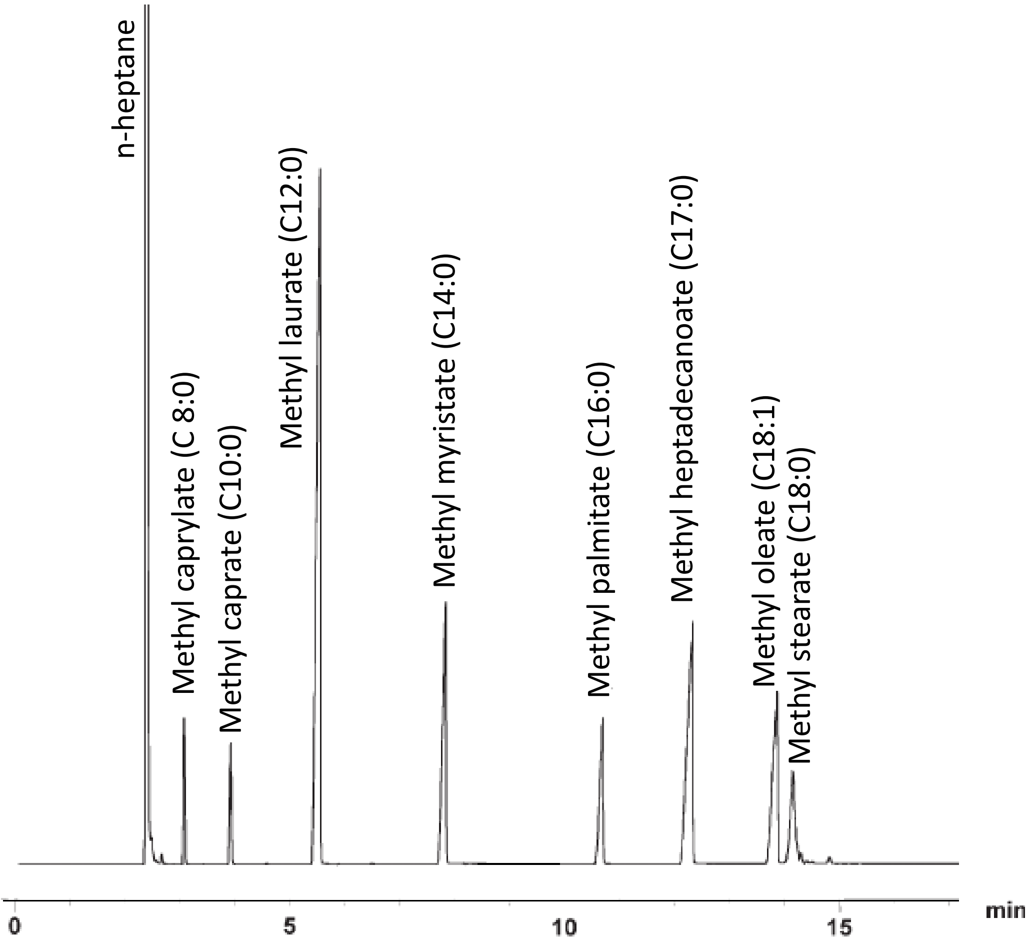

Figure B1 Respresentative chromatogram of FAME product in the presence of methyl heptadecanoate as internal standard.

Table B1 FAME composition and peak area of FAME and normalized FAME distribution (%)

Composition	Area	Normalized FAME distribution (%)
Methyl caprylate (C8:0)	7790	5.85
Methyl caprate (C10:0)	5703	4.28
Methyl laurate (C12:0)	77055	57.87
Methyl myristate (C14:0)	15326	11.51
Methyl palmitate (C16:0)	13250	9.95
Methyl heptadecanoate (C17:0)	66621	-
Methyl oleate (C18:1)	10250	7.70
Methyl stearate (C18:0)	3788	2.84

The FAME yield was calculated according to the equation below.

$$\text{FAME yield (wt\%)}=\frac{\text{Total peak area of FAME} \times \text{Weight of methyl heptadecanoate}}{\text{Total peak area of methyl heptadecanoate} \times \text{Weight of sample}}\times 100$$

Total peak area of FAME = 7790+5703+77055+15326+13250+10250+3788 = 133162

Peak area of methyl heptadecanoate = 66621

Weight of sample = 0.04 g

Weight of methyl heptadecanoate = 0.02 g

$$\text{FAME yield}=\frac{133162 \times 0.02}{66621 \times 0.04}\times 100 \quad = 99.94 \text{ wt.\%}$$

The normalized FAME yield was calculated according to the equation below.

$$\text{Normalized FAME distribution} = \frac{\text{Peak area of each FAME type}}{\text{Total peak area of FAME}} \times 100$$

For example, normalization distribution of methyl laurate

$$\text{Normalized methyl laurate distribution (\%)} = \frac{77055}{133162} \times 100 = 57.87\ \%$$

VITA

Mr. Boontawee Lertpanyapornchai was born on March 9th, 1984 at Bangkok, Thailand. He graduated high school from Rajwinitbangkaepankhum School, Bangkok province, in 2001 and received the Royal Scholarship for Student in Rajavinit School, provided by King Bhumibol Adulyadej (2000– 2001). He graduated the Bachelor's degree of Engineering in Petrochemical and Polymeric Material, Silpakorn University in 2005 and graduated Master’s degree of Engineering in Polymer science and engineering, Silpakorn University in 2008 and received the trophy for outstanding academic performance, provided by Graduate School, Silpakorn University. In 2008–2012, he worked as a lecturer at program in Chemical Industrial, Faculty of Science, Bansomdejchaopraya Rajabhat University. Then, Boontawee joined the Program in Petrochemistry, Chulalongkorn University, as a doctoral student in 2012. He has received the Royal Golden Jubilee Scholarship from Thailand Research Fund (2012–2014). He finished his philosophy of Doctoral Degree in June, 2016.

Presentation:

September 2014 “Mesostructured Sr and Ti Mixed Oxides as Novel Heterogeneous Base Catalysts for Transesterification of Palm Oil with Methanol” in ISCRE 23 & APCRE 7, Bangkok, Thailand

International publication:

B. Lertpanyapornchai , C. Ngamcharussrivichai, Mesostructured Sr and Ti mixed oxides as heterogeneous base catalysts for transesterification of palm kernel oil with methanol, Chemical Engineering Journal 264 (2015) 789–796.

B. Lertpanyapornchai, T. Yokoi, C. Ngamcharussrivichai, Citric acid as complexing agent in synthesis of mesoporous strontium titanate via neutral-templated self-assembly sol-gel combustion method, Microporous and Mesoporous Materials 226 (2016) 505–509.